Influence of Chain Stiffness on Structure and Dynamics of Polymers in the Melt

Dissertation
zur Erlangung des Grades
„Doktor der Naturwissenschaften“
am Fachbereich Physik
der Johannes Gutenberg-Universität
in Mainz

Roland Faller
geboren in Freiburg/Breisgau

Mainz, 2000

Tag der mündlichen Prüfung: 21. Juni 2000

Contents

Summary . . . 9
Zusammenfassung . . . 11

1 Polymers - A challenge on various scales 13

2 Description of polymers - Important results and models 17
- 2.1 Static structure of flexible and semiflexible chains . . . 17
  - 2.1.1 The random walk of a flexible chain . . . 17
  - 2.1.2 Effects of stiffness . . . 18
- 2.2 The Rouse model . . . 20
  - 2.2.1 Changes introduced by stiffness . . . 22
- 2.3 The reptation model . . . 23
  - 2.3.1 Experimental observations . . . 23
  - 2.3.2 The concept of the tube . . . 24
- 2.4 Approaches to combine semiflexibility and entanglements . . . 26
  - 2.4.1 Topological hooking model . . . 26
  - 2.4.2 The fuzzy cylinder model . . . 27
  - 2.4.3 Theory of Odijk and Doi . . . 27
  - 2.4.4 Morse's model of *highly* versus *loosely entangling* . . . 28
  - 2.4.5 The packing length concept . . . 29
  - 2.4.6 The state of the art . . . 29
  - 2.4.7 Theoretical consideration on diffusion in entangled semiflexible polymer melts . . . 30
- 2.5 Fundamentals of NMR in polymers . . . 32
  - 2.5.1 Reorientation and double quantum correlation functions . . . 33
  - 2.5.2 Dynamical order parameter . . . 33
  - 2.5.3 Double quantum experiments . . . 34
  - 2.5.4 Spin-lattice relaxation time . . . 35
  - 2.5.5 NMR and reptation . . . 36

3 Methods for polymer simulations 39
- 3.1 Molecular dynamics . . . 39
  - 3.1.1 Integrator . . . 41
  - 3.1.2 Berendsen method for constant temperature and pressure . . . 42
  - 3.1.3 Brownian Dynamics . . . 42
- 3.2 Monte Carlo . . . 42
  - 3.2.1 End-bridging Monte Carlo . . . 43
- 3.3 Bead spring model: Interaction potentials and description of the system . . . 45
- 3.4 Setup of melt configurations . . . 47

4 Static structure in polymer melts with local stiffness 49
4.1 Chain sizes and persistence length . . . 49
4.2 Orientation correlations . . . 51
4.3 Melt and chain structure . . . 56

5 Dynamic effects of entanglements in melts of semiflexible chains 59
5.1 Reorientation of semiflexible model Polymers . . . 60
  5.1.1 Reorientation correlation function . . . 61
  5.1.2 Comparison to double-quantum NMR experiments . . . 65
  5.1.3 Interdependence of reorientation and translation of segments . . . 67
  5.1.4 Implications . . . 70
5.2 Rouse mode analysis . . . 70
  5.2.1 Short chain systems . . . 71
  5.2.2 Long chains . . . 73
  5.2.3 Chain-length dependence and friction coefficient . . . 73
  5.2.4 Applicability of the Rouse model . . . 75
5.3 Chain diffusion and mean-squared displacements of monomers . . . 75
  5.3.1 Center-of-mass diffusion . . . 75
  5.3.2 Mean-squared displacements of central monomers . . . 77
5.4 Motion along the tube . . . 80
5.5 Comparison to theoretical predictions . . . 81
5.6 Dynamical structure functions . . . 82
5.7 The dynamics: A short overview . . . 85

6 Atomistic simulations of polyisoprene 89
6.1 Technical details . . . 89
6.2 The force-field . . . 91
  6.2.1 Torsion potentials . . . 91
  6.2.2 Angle potentials and bond lengths . . . 96
  6.2.3 Non-bonded potential . . . 96
6.3 Preparation of the melt . . . 99
  6.3.1 Starting configuration from quantum chemical torsion distributions . . . 99
  6.3.2 Application of end-bridging Monte Carlo . . . 99
6.4 Thermodynamic observables . . . 101
6.5 Conformations of the chains . . . 101
  6.5.1 Persistence length . . . 102
  6.5.2 Distribution of torsions . . . 103
6.6 Melt structure . . . 104
  6.6.1 Radial distribution functions and local molar fractions . . . 104
  6.6.2 Static orientation correlations . . . 108
  6.6.3 Melt structure function . . . 109
6.7 Dynamics of atomistic polyisoprene oligomers . . . 110
  6.7.1 Reorientation . . . 110
  6.7.2 Torsion dynamics . . . 117
6.8 General remarks . . . 118

7 An attempt of unification 121

7.1 Comparison of the dynamics of monomeric segments in atomistic and bead-spring models . . . 121

7.1.1 Mean-squared displacements . . . 121

7.1.2 Comparative Rouse mode analysis . . . 122

7.1.3 Reorientation . . . 123

7.2 A view back on the atomistic scale . . . 125

7.3 The global scale - Stiffness versus entanglements . . . 125

7.4 Stiffness on different scales . . . 126

7.5 Final conclusions . . . 127

A Relationship between double-quantum correlation function and reorientation correlation function 129

B List of Symbols 131

Bibliography 135

List of Figures 145

List of Tables 147

Summary

This thesis focuses on the investigation of models of locally stiff polymers in the melt by means of molecular dynamics simulations. In particular, the local properties in statics and dynamics are examined. Two simulation models are used: first, a generic polymer model with only the stiffness entering as a parameter characterizing specific polymers. This model allows for the simulation of relatively large time and length scales. Additionally, detailed atomistic simulations of a model of *trans*-polyisoprene were carried out. The model parameters were derived from a mixture of *ab initio* quantum chemistry and a newly developed automatic procedure for force-field parameterization.

With the first model the statics and dynamics of *wormlike chain* polymers in the melt can be observed. The static properties arise as expected from theory. The overall structure of the melt consists of Gaussian random walk chains, which are stretched on very local scales. Thus, the blob concept is suitable as static description. Local orientations depend on stiffness only weakly although they are present on the scale of a few monomeric units.

This, however, changes drastically in the dynamics. The reptation model for long chains in the melt is no longer able to fully describe the encountered dynamics. This is the main result of this work. Long chains move as if confined to tubes. Yet, this motion depends considerably on stiffness. Fully flexible chains move as expected, whereas chains of the relatively weak stiffness leading to a persistence length of five monomer units move almost only along their contour, as transversal motions are effectively suppressed. This leads to the missing of the $t^{1/4}$ behavior in the segmental motion commonly regarded as marking observable for reptation. For these chains the behavior of double-quantum NMR experiments could be reproduced qualitatively where a two-stage reorientation is observed. So the dynamics reflects experimental results in large even with such a simple model. It is no longer possible to define an entanglement length for stiffer chains in a simple way. For chains of stiffness five the entanglement length already approaches the persistence length. A more detailed study of the interdependence of these lengths especially at higher stiffnesses was prohibited by the nematic ordering transition which occurs in the melt quite early. Dynamic structure functions and primarily visualizations indicate as well that the chain motion is effectively confined to a tube.

The atomistic polyisoprene model was compared with different experiments, primarily NMR. A two stage reorientation appears in these oligomers where the first stage is contingent on the high frequency bond vibrations and the second stage on the overall reorientation of the short chains. To generate different independent starting configurations the end-bridging Monte Carlo technique was adapted to the polymer under study. In the subsequent molecular dynamics simulations experimental results could be reproduced qualitatively and semiquantitatively. Differences to simulations of *cis*-polyisoprene from other groups could be observed. Nevertheless, the findings are all in all comparable.

Finally, the model-free mapping of time and length scales of the two different models was a success with respect to reorientation behavior although the Rouse modes cannot be mapped onto each other.

Zusammenfassung

Die vorliegende Arbeit beschäftigt sich mit der Untersuchung von Polymeren mit intrinsischer Steifigkeit. Es werden vor allem lokale statische und dynamische Eigenschaften anhand zweier verschiedener Simulationsmodelle betrachtet. Das erste ist ein generisches Polymermodell, bei dem nur die Steifigkeit als ein das spezifische Polymer charakterisierenden Parameter eingeht. Dieses Modell erlaubt die Simulation über relativ große Zeitspannen und Längenskalen. Als zweites wird mit Hilfe einer Mischung aus *ab initio* Quantenchemie und einem neuentwickelten Verfahren zur Kraftfeldoptimierung ein detailliertes atomistisches Modell für *trans*-Polyisopren entwickelt.

Mit Hilfe des ersten Modells können Statik und Dynamik wurmartiger Ketten beobachtet werden. Die statischen Eigenschaften ergeben sich, wie theoretisch für eine Schmelze erwartet. Die Gesamtstruktur der Ketten in der Schmelze besteht aus Gaussschen Irrflügen, die auf lokalen Skalen gestreckt sind. Daher ist das Blob-Konzept eine angemessene statische Beschreibung. Die lokalen Orientierungen hängen nur schwach von der Steifigkeit ab, obwohl sie durchaus über mehrere Monomereinheiten hinweg beobachtet werden können.

In der Dynamik ändert sich dieses Bild grundlegend. Das Reptationsmodell kann die beobachtete Dynamik für lange Ketten nicht mehr angemessen beschreiben. Dies ist das zentrale Ergebnis der Arbeit. Lange Ketten bewegen sich, als ob sie in Röhren gezwängt wären; jedoch ist die Bewegung stark abhängig von der Steifigkeit. Voll flexible Ketten bewegen sich wie erwartet, während sich Ketten mit einer relativ schwachen Steifigkeit, die zu einer Persistenzlänge von fünf Monomereinheiten führt, fast ausschließlich entlang ihrer Kontur bewegen, da Transversalbewegungen durch die Steifigkeit effektiv unterdrückt werden. Insbesondere kann das $t^{1/4}$-Verhalten in der Segmentbewegung, das üblicherweise als Indikator für Reptation benutzt wird, nicht mehr beobachtet werden. Für Ketten dieser Art konnte qualitativ das Verhalten reproduziert werden, das in Doppelquanten-Kernspinresonanz (NMR)-Experimenten beobachtet wird. Es handelt sich um einen Zweistufenprozess. Die Dynamik solch einfacher Modelle kann damit zur Beschreibung der experimentellen Realität herangezogen werden. Eine Verhakungslänge lässt sich für solche Ketten kaum mehr definieren, da für Ketten mit einer Persistenzlänge von fünf Monomeren die Verhakungslänge etwa genauso kurz ist wie die Persistenzlänge. Eine genauere Untersuchung dieser Abhängigkeit bei steiferen Ketten war aufgrund des nematischen Phasenübergangs, der in einer dichten Schmelze derartiger Ketten sehr früh eintritt, nicht möglich. Dynamische Strukturfunktionen und insbesondere die direkte Visualisierung der Ketten verdeutlichen die effektiv auf eine Röhre beschränkte Bewegung.

Das atomistische Polyisoprenmodell wurde mit verschiedenen Experimenten, hauptsächlich NMR, verglichen. Ein Zweistufenprozess findet sich bei diesen Oligomeren, wobei die erste Stufe von den hochfrequenten Bindungsschwingungen abhängt, die zweite Stufe hingegen die Gesamtreorientierung der Kette widerspiegelt. Um mehrere unabhängige Startkonfigurationen zu erhalten, wurde das „endenverbindende“ Monte-Carlo-Verfahren auf dieses Isomer angepasst. In den anschliessenden Molekulardynamiksimulationen bei verschiedenen Temperaturen konnten qualitativ und semiquantitativ experimentelle Ergebnisse reproduziert werden. Ebenso werden Unterschiede zu Simulationen an *cis*-Polyisopren anderer Gruppen festgestellt, die allerdings nicht sehr groß sind.

Zuletzt wurden die Längen- und Zeitskalen der beiden Modelle erfolgreich aufeinander abgebildet, wobei, obwohl die explizite Dynamik nicht die gleiche ist, Diffusion und Reorientierung jedoch mit der gleichen Abbildung beschrieben werden können.

1 Polymers - A challenge on various scales

In the modern world, one cannot escape polymers - be it simple applications like plastic foil packaging through food technology, e. g. all the fat substitutes in low fat products are polymeric, or high performance materials in the clothing industry or even space technology. No other class of materials is so diverse and multi-functional. Even DNA which stores the human and all creatures' genome is a polymer. There are plenty of reasons for looking into generic features of the whole class of materials as well as for special features of a specific synthetic or naturally abundant polymers.

Polymers are chain molecules, characterized by the repetition of chemically equal or similar units (monomers). The most simple polymers are therefore chains of equal repeat units (homopolymers). There are several more complex variants, including topologically more complex ones when multi-functional units are introduced leading to stars, brushes or networks. Chemically more complex polymers are obtained when different repeat units along the chain line up randomly, alternatingly or in blocks (see fig. 1.1). One of the major challenges in polymer science is the large range of time and length scales spanning from interatomic bond distances (a few Å) to macroscopic scales. They require one to apply various experimental techniques like nuclear magnetic resonance (NMR) [SRS94], neutron [ZRF$^+$92, ZAC$^+$95, SFL$^+$98] and X-ray [Ale69] scattering, rheology [OMK70], atomic force microscopy [PSD95] and many others (see e.g. [Str97]) in order to elucidate the interesting and complex properties.

This challenge makes it even more demanding to understand polymers from a theoretical point of view. It is essential to combine different theoretical approaches developed independently in various fields of physics and theoretical chemistry which cannot not be easily interlinked. Perturbation theories depend on the dominance of one interaction or length scale over all the others, only treated as perturbations. Therefore, such theories are often not applicable to polymers due to the complex interrelation of length and time scales. A fundamental property of polymer chains is, that they cannot cross each other, as this would break chemical bonds and violate the excluded volume. This is difficult to incorporate into a theory as the resulting topology conservation imposes constraints on the equations of motion.

Computer simulations can contribute substantially to the understanding of physics and chemistry. They are the means of study applied in this thesis. Here, the different scales pose a severe problem. Actually, it is the hardest task in simulations to deal with all the length and time scales because the time step of the simulations is set by the fastest motion. This motion, however, is often not very important for answering the typically "interesting" mesoscopic or macroscopic questions. But in order to keep a correct dynamics, one has to be careful in integrating out these fast degrees of freedom correctly. The big advantage of simulations is the free access to all information about the system at all times. One knows "everything". However, simulations are only models of reality. One has always to validate them against experiments or analytic theory, and refine the model if necessary.

The subject of this work is the melt state of polymers, which is very interesting from the point

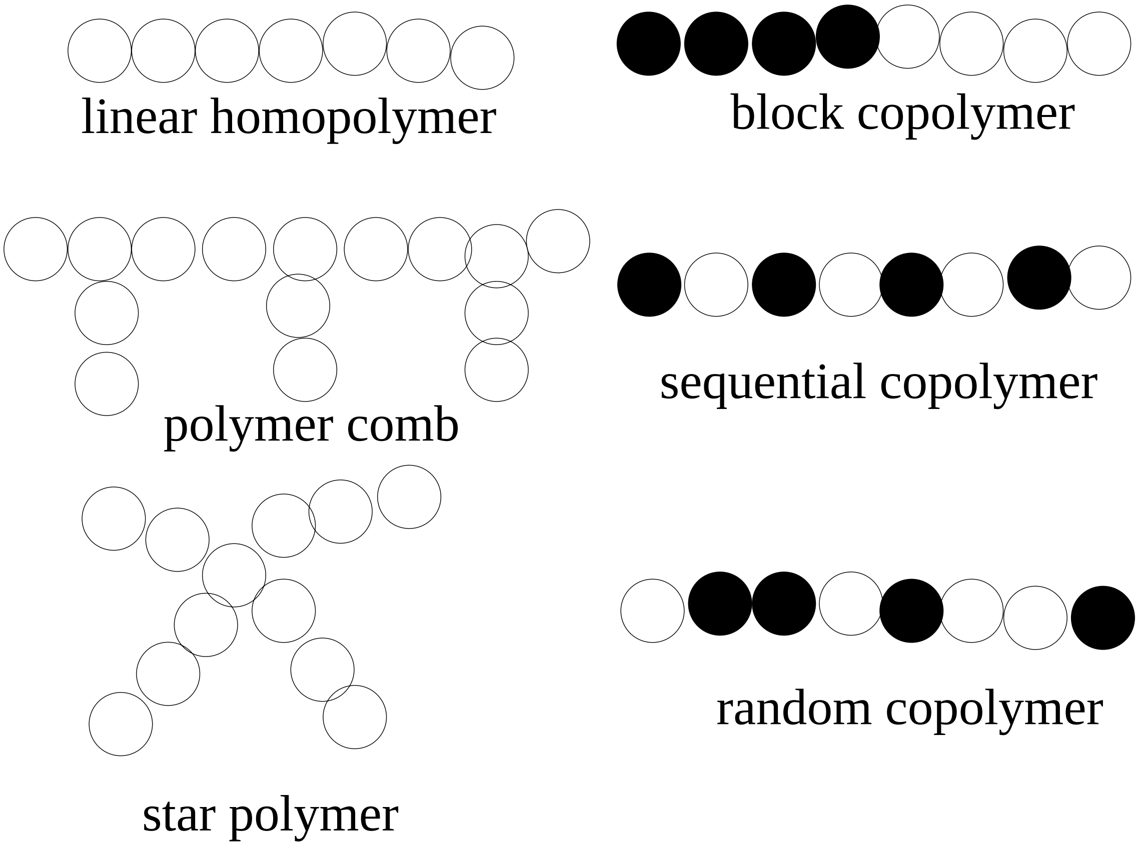
linear homopolymer
block copolymer
polymer comb
sequential copolymer
random copolymer
star polymer

Figure 1.1: Illustration of some topological polymer classes and of classes of copolymers. More complex copolymers are realized if more types of monomeric units are introduced.

of view of its dynamics depending on the degree of polymerization, i.e. the chain length. The properties change drastically from liquid-like to rubbery behavior as the chain length increases. Moreover, they are viscoelastic. They behave liquid-like if slow deformations are applied. In the high-frequency range they respond elastically to deformations like a solid. An important example for a polymer melt is non-vulcanized rubber, as e.g. polyisoprene. Besides, the melt state is crucial to polymer processing as most polymers in industrial applications are processed in their melt state, e.g. by injection molding. Thus, the technological relevance of a better understanding of polymer melts is obvious.

This thesis now deals on one hand with a very simple generic model of polymers that are just beads connected by springs. This model allows the investigation of generic questions on mesoscopic length scales where the detailed chemistry is of minor importance. On the other hand, a specific model for *trans*-polyisoprene is developed and examined in detail in order to be able to compare more directly to experimental data. Both approaches study different parts of the problems. The main focus is on the local scale structure and dynamics of chains in the melt. Recent nuclear magnetic resonance experiments on polybutadiene melts found local scale dynamics which cannot yet be explained completely by existing theories [GHS98]. Local reorientation dynamics is a main prerequisite for the understanding of such modern NMR experiments. Therefore, the reorientation of bond and segment vectors along polymer chains is a major issue of study in the subsequent chapters.

For the not too distant future, it would be desirable to calculate material properties of not yet synthesized polymers. To do this, one would need a link between the atomistic and the macroscopic length scales. Nowadays, however, even the local scale is not fully understood. This thesis wants to contribute to the understanding of local-scale phenomena in polymers; especially the influence of different chemical architectures, which express themselves in different stiffness, is under investigation.

This thesis is organized as follows. Chapter 2 reviews several important theoretical concepts for the understanding of polymer-melt statics and dynamics together with experimental observations. The following chapter discusses methods and models for polymer simulations. Chapters 4 and 5 present static and dynamic observations in the generic model as a function of stiffness. In chapter 6, a detailed polyisoprene model is developed and discussed. Finally, conclusions are drawn by linking the different length scales.

2 Description of polymers - Important results and models

The static structure and the dynamics of polymer chains are at the focus of several theoretical concepts. This chapter first provides a summary of models describing the static observables of polymer chains in the melt. Then, two of the most prominent dynamical models, the Rouse and the reptation model, are recapitulated in order to put the current work in the appropriate framework. A more detailed description is given in the original literature [Rou53, de 71] as well as in standard text books [de 79, DE86]. The Kratky-Porod model of semiflexiblity and some recent approaches to combine semiflexibility with entanglements are presented in sections 2.1.2 and 2.4. As nuclear magnetic resonance (NMR) experiments are addressed in the subsequent chapters, some fundamental connections between reorientation of polymer chains and NMR observables are discussed as well.

2.1 Static structure of flexible and semiflexible chains

2.1.1 The random walk of a flexible chain

In the most primitive model of a polymer, the monomers are simply connected beads without any correlation. If there are correlations, one maps more than one real monomer onto one bead to arrive at the length scale appropriate for this treatment. The polymer configuration performs a random walk (RW) in three dimensional space. The mean squared end-to-end distance of a chain consisting of N beads connected by fixed bonds of length l_b is given by

$$\begin{aligned}
\left\langle \vec{R}^2_{\text{e-e}} \right\rangle &= \left\langle \left(\vec{R}_N - \vec{R}_1 \right)^2 \right\rangle \\
&= \left\langle \Big(\sum_{i=1}^{N-1} [\vec{R}_{i+1} - \vec{R}_i] \Big)^2 \right\rangle \\
&= \left\langle \sum_{i,j=1}^{N-1} (\vec{R}_{i+1} - \vec{R}_i)(\vec{R}_{j+1} - \vec{R}_j) \right\rangle \\
&\overset{\text{RW}}{=} \left\langle \sum_{i=1}^{N-1} (\vec{R}_{i+1} - \vec{R}_i)^2 \right\rangle \\
&= (N-1) l_\mathrm{b}^2. \qquad (2.1)
\end{aligned}$$

The second to last equality is true because of the absence of correlations, so that only the diagonal terms contribute to the average.

An experimentally accessible measure, e.g. by small angle neutron scattering or light scattering, for the size of a polymer chain is its radius of gyration

$$R_{\text{gyr}} = \sqrt{\frac{1}{2N^2}\sum_{i,j=1}^{N}\left\langle(\vec{R}_i-\vec{R}_j)^2\right\rangle} = \sqrt{\frac{1}{N}\sum_{i=1}^{N}\left\langle(\vec{R}_{\text{cm}}-\vec{R}_i)^2\right\rangle}\,, \tag{2.2}$$

$$\vec{R}_{\text{cm}} = \frac{1}{N}\sum_{i=1}^{N}\vec{R}_i\,, \tag{2.3}$$

where $\vec{R}_{\text{cm}}$ is the position of the center of mass of a chain. The radius of gyration averages over all distances between monomers on a chain.

In the case of a random walk, often referred to as Gaussian chain, the radius of gyration and the end-to-end distance are related by

$$\vec{R}^2_{\text{gyr}} = \frac{\vec{R}^2_{\text{e-e}}}{6}\,. \tag{2.4}$$

This is not the case for other conformations. If the chain is more elongated the ratio becomes smaller ($1/12$ for an infinitely thin rod), a more collapsed conformation has a bigger ratio ($1/3$ for a sphere).

2.1.2 Effects of stiffness

Real polymers are not fully flexible, especially not on local scales. They cannot fold back onto themselves. Moreover, most of them have an intrinsic stiffness leading to locally stiff parts of more than one monomer size. To describe this, one needs a model including local stiffness or even semiflexibility. In the context of this work, semiflexibility means a constant stiffness along the chain backbone. For the *statics* of a melt the “blob model” provides a good description. It claims that all local *intra*-chain interactions lead just to a prefactor in the random walk extension

$$R^2_{\text{e-e}} = C_N(N-1)l_{\text{b}}^2\,. \tag{2.5}$$

The constant C_N depends on chain length. In the limit of long chains, however, it must become independent of chain length, as all local features become irrelevant. Then one can write:

$$R^2_{\text{e-e}} = C_\infty(N-1)l_b^2\,. \tag{2.6}$$

So all local interactions are summarized into an effective monomer size beyond which generic scaling arguments apply. This length scale is called the Kuhn length l_{K} [Kuh34] and defined as

$$l_{\text{K}} = \frac{\langle\vec{R}^2_{\text{e-e}}\rangle}{R^{(\text{max})}_{\text{e-e}}} = \frac{\langle\vec{R}^2_{\text{e-e}}\rangle}{(N-1)l_b} = C_\infty l_{\text{b}} \tag{2.7}$$

with $R^{(\text{max})}_{\text{e-e}}$ the maximum possible length of the end-to-end vector in fully stretched conformation. Direction correlations of neighboring bonds can be used to define another length, the *persistence length* l_{p}. It is the length on which such correlations decay. Local potentials lead to a short-range exponential decay. Then the persistence length in monomer units is defined as in equation (2.8)

$$\left\langle\vec{u}(n)\vec{u}(n\pm j)\right\rangle = e^{-j/l_{\text{p}}}\,. \tag{2.8}$$

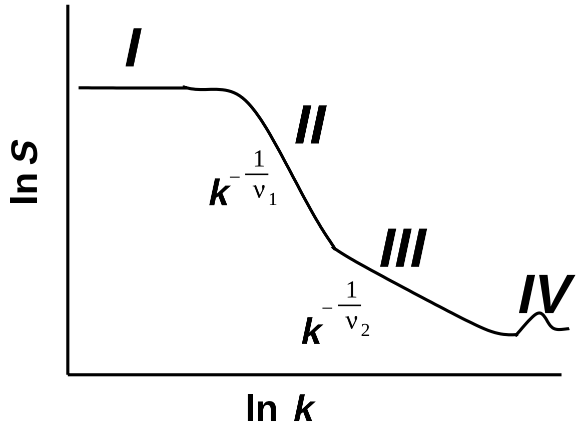

Figure 2.1: The different regimes of the single chain structure factor of a semiflexible chain in the melt in double logarithmic representation.

The vector $\vec{u}(n)$ is a tangent vector on the chain characterizing the direction of monomer n. Originally, the persistence length comes from the *wormlike*-chain picture (see below).

Static single chain structure factors $S_{\mathrm{SC}}(k)$, which can be measured by different scattering techniques [Str97], support the blob picture. The structure factor is the three-dimensional Fourier transform of the monomer positions. Here only the spherical average is needed, so that the wave-vector $\vec{k}$ and the position vectors $\vec{R}_j$ of bead j on the chain appear only with their moduli

$$S_{\mathrm{SC}}(k) = \left\langle \left| \sum_{j=1}^{N} \exp(ikR_j) \right|^2 \right\rangle . \tag{2.9}$$

For a continuous fractal curve in three dimensions the structure factor decays with a simple scaling exponent relating to the fractal dimension of the curve. Polymers are not true fractals as they are finite and cannot be self-similar on all scales. An ideal random walk is a fractal curve with a dimension of 2 embedded in three-dimensional space. Normally, in the structure factor a scaling regime is found which shows that, within approximation, mesoscopic length scales can be described as fractals. In the melt, chains are random walks since the blob picture holds. Thus, the structure factor behaves in this scaling regime as $S_{\mathrm{SC}}(k) \propto k^{-1/\nu}$ with a scaling exponent $\nu = 1/d = 1/2$. The high wave-vector end relates to intra monomer structure and for $k \to 0$ one finds the finite dimension of the chain relating to the radius of gyration. The typical shape of $S_{\mathrm{SC}}(k)$ is depicted in figure 2.1.

The structure factor of a locally stiff chain in the melt shows two scaling regimes relating to different fractal dimensions on different scales. On local scales the chain is stretched, but on larger length scales a random walk of blobs is recovered. In regime *I*, only the overall extension of the chain is seen. Therefore, the structure factor behaves like $1 - q^2/3R_{\mathrm{gyr}}^2$ which is the beginning of a cumulant expansion. The second regime is a Gaussian scaling regime decaying with k^{-2}. In the case of solutions the scaling behavior is fundamentally different with a scaling exponent $\nu \approx 0.59$. At a wave-vector related to the persistence length, the decay crosses over to regime *III* where a rod-like behavior with k^{-1} is observed. A rod has obviously a dimension of one. On very local scales (regime *IV*), the internal monomer structure shows up, which is of no relevance to scaling. In bead-spring models, like the one discussed in the following chapters, this regime is meaningless.

If one wants to take semiflexibility into account in a dynamic study, a model with energies and forces arising from stiffness is needed. For this purpose the *wormlike chain* model was introduced by Kratky and Porod, which establishes an additional contribution to the energy penalizing chain bending [KP49]

$$U_{\text{bend}} = \frac{E}{2}\int_0^L \mathrm{d}s \left(\frac{\partial \vec{u}}{\partial s}\right)^2 . \tag{2.10}$$

Here, s is the coordinate along the chain contour. The model is continuous, which is convenient for general theoretic considerations. Real polymers are not continuous curves but rather consist of discrete finite-size monomers. The discrete version of this model, which is applied to simulations in bead-spring systems, reads

$$V_{\text{angle}} = x\left(1 - \frac{\vec{r}_{i-1,i}\cdot\vec{r}_{i,i+1}}{r_{i-1,i}r_{i,i+1}}\right), \tag{2.11}$$

where x is a parameter of dimension energy, measured in the following in units of $k_B T$, describing the stiffness. In the limit of long chains the numerical values of persistence length l_{p} and x coincide in the chosen unit system. For a semiflexible chain, the radius of gyration can be calculated analytically [HWR97]

$$R^2_{\text{gyr}} = \frac{Ll_{\text{p}}}{3} - l^2_{\text{p}} + \frac{2l^3_{\text{p}}}{L} - \frac{2l^4_{\text{p}}}{L^2}(1 - e^{-L/l_{\text{p}}}) \tag{2.12}$$

with the contour length $L = (N-1)l_{\text{b}}$. The connection between the Kuhn-length and the persistence length can for the *wormlike* chain model be shown to be

$$l_{\text{K}} = 2l_{\text{p}} . \tag{2.13}$$

2.2 The Rouse model

A simple model for describing polymer dynamics was developed by Rouse in the 1950s [Rou53]. A polymer chain is taken as a number of noninteracting points connected by harmonic springs in a background of homogeneous friction. These basic assumptions lead to coupled Langevin equations of motion for the monomers

$$\xi\frac{\mathrm{d}\vec{R}_n}{\mathrm{d}t} = -k\Big[2\vec{R}_n - \vec{R}_{n+1} - \vec{R}_{n-1}\Big] + \vec{f}_n,\ 1 \le n \le N . \tag{2.14}$$

$\vec{R}_n$ are the position vectors of the beads, ξ is the constant friction coefficient, and $\vec{f}_n$ the stochastic force acting on the bead. $\vec{f}_n$ and ξ are coupled by a fluctuation dissipation theorem defining the temperature T (see e.g. [Rei65])

$$\frac{\xi}{m} = \frac{1}{2k_B T}\int_{-\infty}^{\infty}\Big\langle \vec{f}(t)\,\vec{f}(0)\Big\rangle \mathrm{d}t . \tag{2.15}$$

The equations (2.14) do not contain an inertial term. The motion is overdamped, as the stochastic forces are assumed to dominate the motion. It is a mean-field model, as all the effects of possible surroundings, e.g. solvent particles or other chains, are collected into one simple number, the friction coefficient. The chains are ideal Gaussian random walks moving independently. Nothing in the equations prevents them from cutting through each other. Thus, they move isotropically (in the ideal case).

Though the Rouse model was developed for a single polymer chain in solution, it is not able to describe this situation correctly because of the lack of hydrodynamic interactions[1] but is rather

---

[1] The Langevin dynamics does not conserve momentum. For hydrodynamic interactions the Zimm model [Zim56] is quite successful.

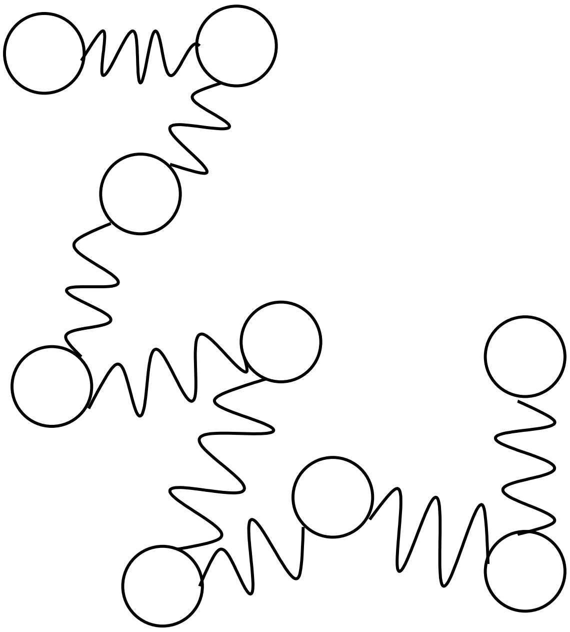

Figure 2.2: In the Rouse model the beads are connected with springs in a background of homogeneous friction.

appropriate for short flexible chains in the melt (see e.g. [DE86]). The reason for this is, that in the melt the chains screen each other from all long-range forces. In this context *long-range* means interaction between topologically or spatially distant monomers, be it the excluded volume (the monomers are not point particles, but need a finite volume) or hydrodynamic interactions. Hence, a local description is well suited.

The model is exactly solvable by transformation to the eigenmodes $\vec{X}_p$ of eq. (2.14) which are analogous to Fourier modes of the chain.

$$\vec{X}_p = \frac{1}{N} \sum_{i=0}^{N-1} \cos\left(\frac{\pi p (i + 1/2)}{N}\right) \vec{R}_i \ . \tag{2.16}$$

Since these modes diagonalize the differential equation system and lead to the uncoupled equations (2.17), the model is solved completely

$$\xi_p \frac{\partial}{\partial t} \vec{X}_p = -k_p \vec{X}_p + \vec{f}_p \ . \tag{2.17}$$

The $\vec{f}_p$ are the representation of the random forces in the space spanned by the eigenmodes with index p denoting the mode number. The k_p are the oscillator strengths of the respective modes. The mode with index 0 relates to the center of mass motion, $p = 1$ is the internal mode with the longest wave-length and so on.

As the system is solved for given random forces, one can calculate observables of systems if the exact mapping, i.e. the friction coefficient, is known. The overall center of mass diffusion constant reads

$$D = \frac{k_B T}{N \xi} \tag{2.18}$$

with N being the monomer number (or more precisely the number of Kuhn segments, see above). Several simulational [KG90, HMT98] and experimental [Fer80] investigations for short chains have been performed confirming the prediction. Moreover, the diffusion constant leads to a melt viscosity of monodisperse melts to scale with $\eta \propto N$. The relation between viscosity and diffusion coefficient may even be used to deduce melt viscosities from computer simulations after the Rouse model has been confirmed e.g. by the correlation functions of modes [HMT98].

The autocorrelation functions

$$\left\langle X_{p\alpha}(t) X_{q\beta}(0) \right\rangle = \delta_{pq} \delta_{\alpha\beta} \frac{k_B T}{k_p} e^{-t/\tau_p} \tag{2.19}$$

of the Rouse eigenmodes decay exponentially for $p > 0$. The Greek indices denote the Cartesian components of the vectors. The respective time constants behave like $\tau_p = \tau_{\mathrm{R}}/p^2$ with $\tau_{\mathrm{R}} \equiv \tau_1$ called the *Rouse* time, the longest relaxation time of the system

$$\tau_{\mathrm{R}} = \frac{\zeta N \langle R^2_{\text{e-e}} \rangle}{3\pi^2 k_B T} \; . \tag{2.20}$$

One sees that the correlation time τ_0 of mode $p = 0$ diverges, as the correlation function of the center of mass motion does not decay exponentially. The center of mass performs a normal diffusive motion. As shorter chains do not differ from subchains of longer chains in this model, the relaxation times of short chain polymer melts behave like $\tau_{\mathrm{relax}} \propto N^2$.

For describing the motion of the chains, mean-squared displacements (MSD) of whole chains related to the diffusion and mean-squared displacements of monomers on the chain are often discussed. In the Rouse model, two regimes for the inner-monomer-MSD are to be considered. First, there is a sub-diffusive motion, as the internal degrees of freedom are not relaxed

$$g_1(t) := \left\langle [\vec{R}_{N/2}(t) - \vec{R}_{N/2}(0)]^2 \right\rangle \propto t^{1/2} \; . \tag{2.21}$$

In order to limit end-effects always the central monomer is used for $g_1(t)$. A monomer is not free to diffuse, since it is connected to the chain and has to drag more and more “mass” of other monomers with it for longer and longer distances. As this part of the chain becomes the whole chain, the monomer diffusion and the center of mass diffusion obey the same dynamics, i.e. a normal diffusive motion $g_1 \propto t$. This behavior is shown in fig. 2.3a. For future reference a second function $g_3(t)$ is, additionally, defined here, which is the mean-squared displacement of the center of mass

$$g_3(t) := \left\langle [\vec{R}_{\mathrm{cm}}(t) - \vec{R}_{\mathrm{cm}}(0)]^2 \right\rangle . \tag{2.22}$$

2.2.1 Changes introduced by stiffness

In the case of an additional stiffening potential, the stiffness plays an increasing role for eigenmodes of large wave-vectors so that the original Rouse model is no longer appropriate. But still, analytical calculations of the relaxations of the modes are possible. The eigenmodes and the correlation functions of the respective amplitudes have been calculated analytically [HWR97]. The resulting correlation times have to be derived from transcendental equations which incorporate the two limits of full flexibility and strong rigidity. In the limit of small persistence length a Rouse-like dependence is recovered (γ is a normalization constant)

$$\tau_p = \frac{\gamma L^2}{3\pi^2 l_{\mathrm{p}} k_B T p^2} \; . \tag{2.23}$$

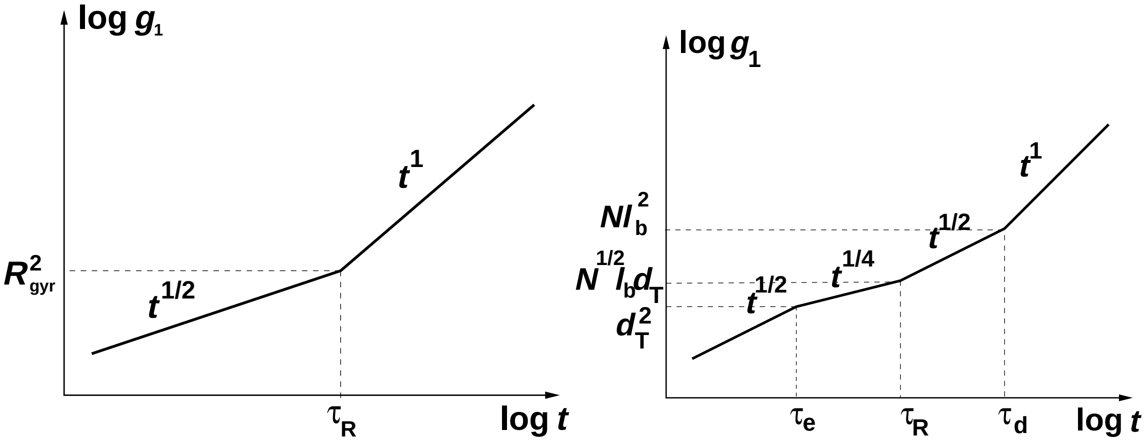

Figure 2.3: Dynamical scaling laws of the mean-squared displacement of inner monomers with time: a) Rouse model, b) reptation model.

For high stiffness the relaxation times increase with L^4 and the dependence on mode number changes drastically

$$\tau_p = \frac{32\gamma L^4}{l_\mathrm{p} 3(2p-1)^4 \pi^4 k_B T} \ . \tag{2.24}$$

The longest relaxation time in the high stiffness case does no more scale with L^2 as in the Rouse case. Thus, the relaxation is slowed down by stiffness.

In the “intermediate” regime where the bending modes and the Rouse modes are equally important an analytical treatment becomes very involved [HWR97].

2.3 The reptation model

2.3.1 Experimental observations

Experimentally, one observes that the Rouse model is no longer appropriate for chains longer than a characteristic length. Thus, a more elaborate model has to be used, which includes the *entangling* of long polymer chains. From the experimental point of view there are typically two different ways of defining an entanglement molecular mass M_e or a critical molecular mass M_c, respectively.

Plateau modulus

The former (M_e) is derived from the plateau in the oscillatory shear modulus [Fer80]. In an oscillatory shear experiment the stress σ applied to a material and the measured strain $\gamma = \gamma^0 \cos \omega t$ are coupled by the following constitutive relation in the case of linear viscoelasticity, i.e. stress and strain follow a linear dependence

$$\sigma = \gamma^0 (G' \cos \omega t - G'' \sin \omega t) \ , \tag{2.25}$$

where G' and G'' are the storage and loss moduli. The storage modulus is the elastic part of the modulus whereas the loss modulus is the inelastic, dissipative part. In entangled polymers one finds a plateau G_N in the storage modulus G' over a range of frequencies ω (fig. 2.4). The existence of the plateau relates to an intermediate time and corresponding length scale which is the maximum

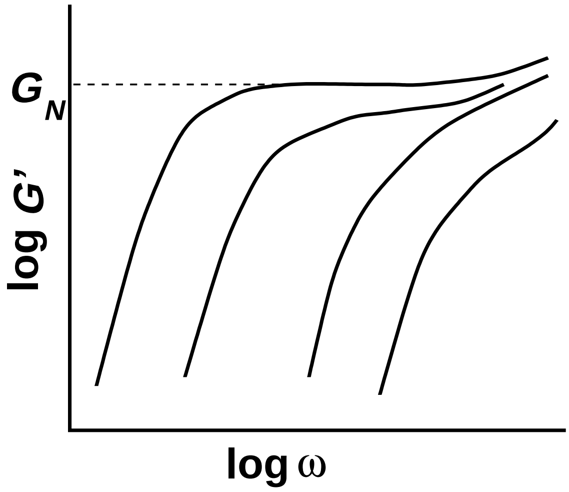

Figure 2.4: A sketch of the plateau in the storage modulus used to extract the entanglement length. The molecular weight increases from right to left. An experimental observation for polystyrenes can be found e.g. in ref [OMK70].

length any local process can see. Any length longer than l_e is “infinite” for all local scales. The relation between the entanglement monomer number N_e and the plateau modulus is

$$G_N = \frac{4\rho k_B T}{5N_\mathrm{e}} \ . \tag{2.26}$$

Viscosity

Experimentally, the viscosity no longer scales for chains longer than a characteristic length with N^2 as predicted by the Rouse model, but rather with $N^{3.4}$ [BF68]. The respective molecular weight M_c is not necessarily the same as M_e but close to it. The change of the scaling exponent may partly be explained by the reptation model introduced by de Gennes [de 71] which predicts a N^3-dependence. Recently it was proposed that the $N^{3.4}$ dependence is only a long lasting cross-over region [MM98]. This has not yet been decided experimentally.

2.3.2 The concept of the tube

The main oversimplification of the Rouse model if applied to polymer melts is the neglect of the non-crossability of the chains, which is a topological property. In nature and simulations this originates from the excluded volume interaction. The reptation model incorporates topological constraining without waiving the simplicity of an effective one-chain picture. The main idea of the reptation model is most easily explained by a bunch of cooked spaghetti. The chains are not allowed to cross each other. Instead they move more easily along their contour than perpendicular to it, as they do not need to push away neighbors in the space the chain occupies already.

Reptation, therefore, introduces the concept of a tube in which the polymer resides. This tube, however, does not exist independently of the chain; the chain defines its tube. It is a mean-field description of the complex topological constraints imposed by neighboring chains. Experiments could actually resolve the snake-like motion of chains by direct visualization [PSC94]. The experiment was performed by dragging a chain through the medium.

The reptation model is under investigation in the following chapters, especially its interplay with local chain stiffness. In this connection some of its deficiencies become clear. One of the

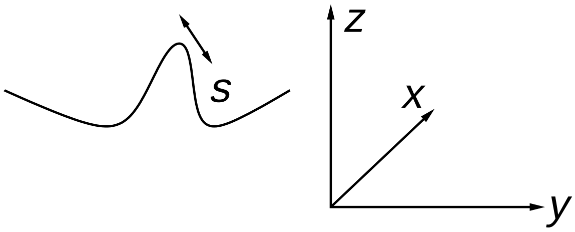

Figure 2.5: The monomers in the tube move along the curvilinear coordinate s performing a random walk. As the tube itself performs a random walk, the motion in cartesian space is more complex.

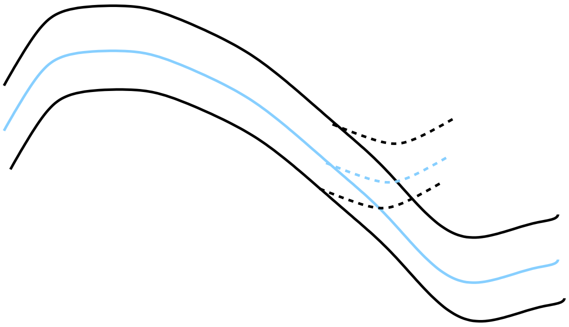

Figure 2.6: The polymer moves back and forth along the tube. When the polymer leaves a part of the tube this part vanishes. By entering in a new region a new part of the tube is defined.

important dynamical measures used in the discussion of reptation is the mean-squared displacement of single monomers. One focuses on the central monomers, i.e. the function g_1 as end-effects obscure the observations. The expected behavior of this entity is depicted in figure 2.3b. After the (here neglected) ballistic regime where monomers just move very shortly following the law of inertia, a Rouse regime with $t^{1/2}$ is expected, because, on short scales, a monomer does not know about the tube and behaves like simply being attached to its own chain. After some time τ_e, so-called *entanglements* start to play a role. The monomers feel the constraint by the tube. This time τ_e can be translated to an entanglement length l_e (or entanglement monomer number N_e) by regarding τ_e, the *entanglement time*, as the Rouse relaxation time of a subchain with N_e monomers. The Rouse model is used for this mapping, as it is expected to hold up to this length, thus: $\tau_R(N_e) = \tau_e$. The so defined entanglement molecular weight is not necessarily the same as the molecular weight M_e of experiments measuring the plateau modulus [PKG00]. As the chain is confined to a one-dimensional tube performing a random walk in three-dimensional space, the sub-diffusive Rouse motion is slowed down even more strongly. A $t^{1/2}$ behavior in the curvilinear contour coordinate s is expected. As the tube performs a random walk in three dimensions, this transforms to a $t^{1/4}$ scaling in Cartesian space (fig. 2.5). After the Rouse time τ_R, all internal degrees of freedom are relaxed, but the chain is still confined to its tube. So the whole chain may be then regarded as a single particle performing a one-dimensional random walk in a curvilinear tube leading again to a $t^{1/2}$ regime, because all monomers just follow the center of mass. Here the diffusive *reptile*-like motion, leading to the model name, is encountered. After some time when the polymer has moved about its own radius of gyration, the tube relaxes. As only the chain can define the tube, the original tube shortens and is rebuilt somewhere else by the chain moving out at the ends (fig. 2.6). The old tube path may still exist; however, it is meaningless without the chain. After the whole tube has been rebuilt this way, an unconstrained diffusive motion in space leads to the standard diffusion exponent $g_1(t) \propto t$. This last crossover time is called the tube *disengagement* time τ_d. Although all these *static* explanations are rather illustrative, one has to keep in mind that the tube itself and the whole concept of entanglements is purely *dynamic*. They are used to give an intuitive picture of the anisotropy of the motions.

Several simulations have been performed to look for reptation [KG90, WPB92, PKG00]. Kre-

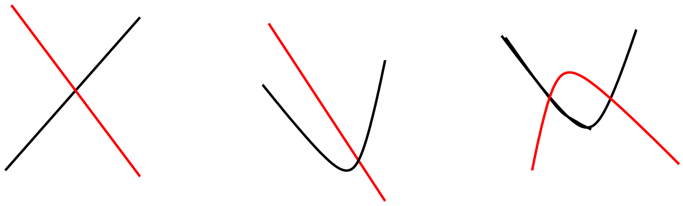

Figure 2.7: Possible “hooking scenarios” according to [Wu89].
Left: plain contact, middle: single hook contact, right: binary hook contact

mer *et al.* and Pütz *et. al.* have used the same model as applied in the following chapters without bending stiffness. The different dynamic regimes could be confirmed and the entanglement length of the model chains was determined by several different methods.

According to the Rouse model the center-of-mass diffusion constant D scales with N^{-1}, whereas in the reptation model it scales with N^{-2}. So if DN, the center-of-mass diffusion coefficient multiplied by the number of monomers, is plotted in a double logarithmic representation versus the number of monomers N, a plateau is expected for short chains. At the entanglement monomer number it kinks down to a straight line with slope -1, $N_\mathrm{e} \approx 32$ is determined this way for flexible chains with excluded volume [KG90]. The crossover time from a $t^{1/2}$ to a $t^{1/4}$ behavior in g_1 gives in the case of flexible chains ($x = 0$) an even better estimate of N_e (after mapping the time to a monomer number using the Rouse model). The tube diameter can be determined by the distance a monomer has diffused at the crossover. For the flexible polymers investigated in the past this tube diameter is $d_\mathrm{T} \approx \sqrt{N_\mathrm{e}}$ (for bond length $l_b \approx 1$). This is no more the case with added semiflexibility as the tube encloses the chain more tightly.

The different scaling regimes introduced in this section can be investigated in more detail. In doing so, the prefactors can be calculated [DE86]. The corresponding equations read for the standard reptation picture of flexible chains

$$g_1 = l_\mathrm{b}\left(\frac{3k_BT}{\pi\zeta}t\right)^{1/2}, \qquad t < \tau_\mathrm{e} = \frac{\pi^2}{9}\frac{\zeta d_\mathrm{T}^4}{k_BTl_\mathrm{b}^2}\,; \tag{2.27}$$

$$g_1 = d_\mathrm{T}\left(\frac{k_BTl_\mathrm{b}^2}{\zeta}t\right)^{1/4}, \qquad \tau_\mathrm{e} < t < \tau_\mathrm{R}\,; \tag{2.28}$$

$$g_1 = d_\mathrm{T}\left(\frac{k_BT}{N\zeta}t\right)^{1/2}, \qquad \tau_\mathrm{R} < t < \tau_\mathrm{d} = \tau_\mathrm{e}\left(\frac{N}{N_\mathrm{e}}\right)^3; \tag{2.29}$$

$$g_1 = \frac{k_BTd_\mathrm{T}^2}{3N^2l_\mathrm{b}^2\zeta}t\,, \qquad t > \tau_\mathrm{d}\,. \tag{2.30}$$

2.4 Approaches to combine semiflexibility and entanglements

Several attempts have been undertaken to treat the semiflexibility in the presence of entanglements. Up to now, none of them can describe the full physics satisfactorily. Here an overview of some approaches is given.

2.4.1 Topological hooking model

A purely topological model to describe the interplay of entanglements and stiffness is based on the *hooking* of polymer chains (fig. 2.7) [Wu89]. According to this model only *binary hooks* are

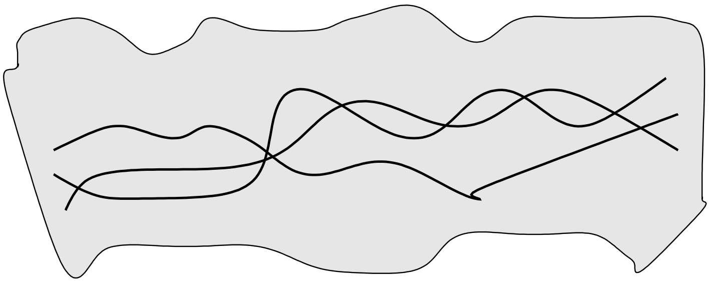

Figure 2.8: Illustration of the fuzzy cylinder model by Sato *et al.* The monomer positions are smeared out on intermediate times defining a cylinder-like object.

entanglement contacts. This reasoning leads then to the relation

$$N_\mathrm{e} \propto C_\infty^2 \,. \tag{2.31}$$

This ansatz, however, is questionable. First, as will be shown later, the entanglement monomer number shrinks massively with increasing persistence length which contradicts this idea. Second, the definition of an entanglement is non-unique especially on the molecular scale.

2.4.2 The fuzzy cylinder model

Some measurements of the shear viscosity of semiflexible chains in the hydrodynamic limit cannot be explained by the standard reptation theory, as the viscosity shows different scaling with concentration and molecular weight [ST91, TST91, OKST95]. Therefore, Sato *et al.* introduced a *fuzzy cylinder* model in order to describe a semiflexible polymer in solution or melt. The main idea is that there is a separation of time-scales between local conformation changes and the overall relaxation (fig. 2.8). The local motion smears out the positions of the different monomers on intermediate time scales. However, the overall reorientation is hindered by entanglements. Every chain defines a fuzzy cylinder by its local motion, and then this cylinder has to relax. For very stiff polymers (persistence length of tens to hundreds of nanometers), there is considerable agreement with experiment. However, the polymers of interest in the present work do not fall into this category.

2.4.3 Theory of Odijk and Doi

Odijk was one of the first, who combined the concept of the tube with semiflexibility [Odi83]. He introduced the concept of a deflection length λ, which is assumed to be small against the Kuhn length $\lambda \ll l_\mathrm{K}$. It is the length between two points where the chain “hits” the tube. This, of course, is only a conceptual picture, as there is no external tube imposing the deflection of the chain at its walls (fig. 2.9). Odijk replaced the chain by straight segments of length λ.

This qualitative argumentation was later quantified by Doi, who assumed that the Brownian motion is dominated by reptation [Doi85]. He derived e.g. a diffusion coefficient D_cm for the center of mass along the chain contour

$$D_\mathrm{cm} = \frac{D}{3}\left\{\frac{l_\mathrm{K}}{L} - \frac{l_\mathrm{K}^2}{2L^2}\left[1 - \exp\left(-\frac{2L}{l_\mathrm{K}}\right)\right]\right\} \,, \tag{2.32}$$

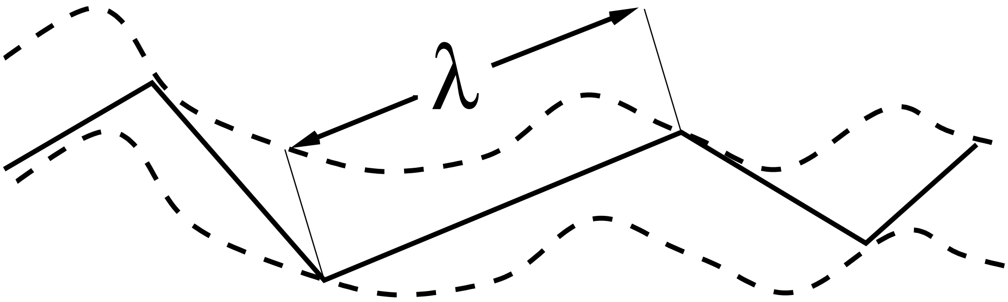

Figure 2.9: The chain in a tube deflected by the walls. The deflection length λ is the mean distance between two “hits” at the tube wall.

where D is the diffusion coefficient along the backbone. The underlying assumption is that the mesh size of the (pseudo)-network is small against the Kuhn segment length. Here again the stiffness defines the bigger length scale. Doi also speculated about a fast bending motion allowing the polymer to interact strongly with its environment in addition to reptation. Thus, the “deflection points” press themselves into the surrounding matrix.

2.4.4 Morse’s model of *highly* versus *loosely entangling*

Recently, Morse has proposed a crossover from a *loosely* to a *highly* entangled state [Mor98a, Mor98b, Mor98c]. The loosely entangled regime corresponds to the standard reptation picture requiring that the chain performs a random walk in the tube, which itself is a random walk. This corresponds to a line which is only very loosely fixed in a wide tube and can therefore wind freely.

The opposite limit is the highly entangled regime (fig. 2.10). It is characterized by the condition $l_\mathrm{p} \gg l_\mathrm{e}$ which is not reached in this work. However, the basic ideas already apply. The chain has to follow the tube and vice versa. For both of them, a wormlike chain model rather than random walk statistics applies at least on local scales (cf. the single chain structure factor, fig. 2.1). In the extreme case, this can be pictured as an electric wire in its insulation hose. The systems studied in the following fall between the two limits as the entanglement length and the persistence length come very close.

Within this model stress tensors and viscoelastic properties can be calculated [Mor98b]. The moduli depend considerably on the persistence-length/contour-length relationship. The plateau in the storage modulus shortens with increasing persistence length. In the framework of this theory, there is a proposal for the dependency of the entanglement length and the tube diameter on the persistence length in the limit of $l_\mathrm{e} < l_\mathrm{p}$ and $d_\mathrm{T} < l_\mathrm{p}$ (*tightly* entangled) [Mor98b] whereby the rheological entanglement length is identified as Odijks deflection length

$$l_\mathrm{e} \propto l_\mathrm{p}^{1/5}\rho^{-2/5} , \tag{2.33}$$

$$d_\mathrm{T} \propto l_\mathrm{p}^{-1/5}\rho^{-3/5} . \tag{2.34}$$

The entanglement length depends on the density ρ and rises weakly with the persistence length whereas the tube diameter shrinks. It is noteworthy that there is no longer a positive correlation between them. Thus, the tube becomes more anisotropic. It is tighter and at the same time longer in comparison to the standard tube picture.

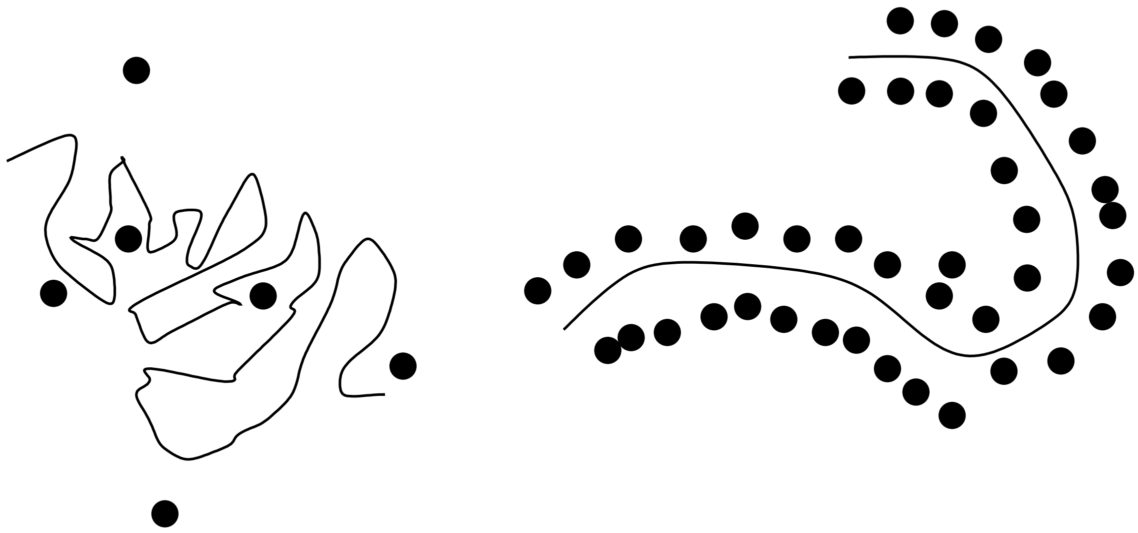

Figure 2.10: Illustration of the Morse model where loosely (left) and highly (right) entangled polymers are of interest.

2.4.5 The packing length concept

It is not yet known, how the entanglement length relates to the persistence length. However, there is a suggestion by Fetters *et al.* that the entanglement molecular weight can be calculated using a *packing length* defined as

$$p = \frac{M}{\langle R_{\text{e-e}}^2 \rangle \rho N_a} \tag{2.35}$$

[FLR+94, FLG99, FLMG99], whereby M is the chain molecular weight per mole chains, $\langle R_{\text{e-e}}^2 \rangle$ the mean-squared end-to-end distance, N_a Avogadro's number and ρ the system mass density. This packing length is a measure of the chain thickness. The choice is motivated by the idea that stiffer polymers are more extended and therefore have more contact to other chains which makes it easier for them to entangle. The decisive length is the length at which one other complete chain is entirely inside the volume spanned by a chain; i.e. the ellipsoid a chain defines is only half filled by itself.

There is some experimental evidence that this length is important for the dynamics, although it is a purely static definition. Fetters *et al.* suggest by fitting to experimental data that the actual entanglement molecular weight reads [FLG99]

$$M_{\text{e}} = 218 \rho p^3 \propto l_{\text{p}}^{-3}. \tag{2.36}$$

At least for the bead-spring model this result is not appropriate as will be shown in section 5.3.

2.4.6 The state of the art

One can conclude that the interplay between entanglements and stiffness is not very well understood analytically. There are several different models which all contribute more or less to the understanding. The extreme limits of full flexibility and full rigidity are described quite well. However, it is not at all clear what happens in the, experimentally very relevant, intermediate regime

concept	N_e	d_T
Wu hooking model	$\propto l_p^2$	
Morse model	$\propto l_p^{1/5}$	$\propto l_p^{-1/5}$
packing length	$\propto l_p^3$	

Table 2.1: The different proposed dependencies of the entanglement length and tube diameter (whichever are available) on the persistence length from the discussed concepts.

where the characteristic lengths arising from stiffness and from entanglements become comparable. In the following chapters this parameter region will be under study. In a dynamical Monte Carlo study using the bond-fluctuation model [CK88], Wittmer *et. al.* looked for the dependence of reptation on temperature with temperature entering as a bending potential that vanishes with $T \to \infty$ [WPB92]. These results can be regarded as the first study of reptation under semiflexibility suggesting an increasing degree of entanglement with stiffness. However, they could not elucidate the dependence of l_e on l_p and have problems with the lattice structure.

Table 2.1 compares the different proposed dependencies of entanglement length or tube diameter on the persistence length.

2.4.7 Theoretical consideration on diffusion in entangled semiflexible polymer melts

For the interesting case of intermediate stiffness, there are only very few theoretical considerations. Therefore, a simple analysis of the segmental motion in this regime is deduced here.

In simulations of entangled melts a new type of dynamics was encountered, whereby monomers of the semiflexible chains can move faster than of flexible ones (sec. 5.3). This can be explained by a strong reptation dynamics, where the chain coincides almost with its tube. The relevant dynamics is therefore the second $t^{1/2}$ regime of the reptation model (fig. 2.3b). In the case of fully flexible chains the *primitive path* diffuses along the tube (figure 2.11). According to a blob argument the persistence length of the tube is $l_{\mathrm{p,tube}} = l_b N_e^{1/2}$ where l_b is the bond length and N_e the entanglement monomer number. So the mean squared displacement of an inner monomer in this dynamic regime (which is difficult to observe for moderately long chains [Püt99]) is

$$g_1(t) = l_b N_e^{1/2} \sqrt{\frac{k_B T}{\xi N} t} \tag{2.37}$$

with the friction coefficient ξ [DE86].

In the semiflexible case the persistence lengths of the tube and the chain cannot be very different. The chain moves almost exclusively along its contour as transverse fluctuations are effectively suppressed by the stiffness. Thus, the mean squared displacement of an inner monomer reads

$$g_1(t) = l_p \sqrt{\frac{k_B T}{\xi N} t} \quad . \tag{2.38}$$

Here the correlation length $l_b N_e^{1/2}$ of the random walk tube of eq. (2.37) is exchanged by the persistence length l_p of the chain. This regime crosses over to the final free diffusion when the chain has moved one tube length along the contour. In the flexible case this is the length of the primitive path; in the semiflexible case, it is the length of the chain itself.

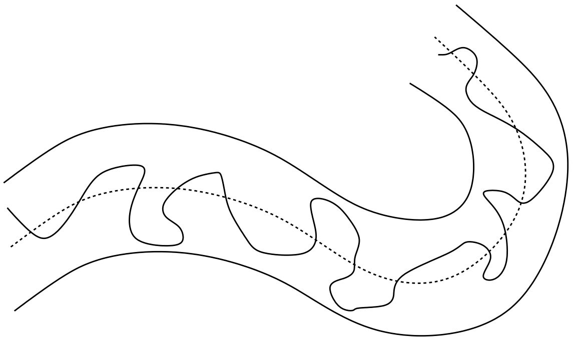

Figure 2.11: The chain in the tube and its primitive path.

The final diffusion coefficient for long times D_∞ may be calculated from

$$D_\infty = \frac{\langle r^2 \rangle_{\mathrm{crossover}}}{t_{\mathrm{crossover}}} \,. \tag{2.39}$$

The mean-squared distance and time of the crossover, however, may be calculated from "below" ($t < t_{\mathrm{crossover}}$), where the above considerations are valid. The respective times are by diffusion along the tube

$$\left.\begin{array}{l} N_\mathrm{e} l_\mathrm{b}^2 \\ \\ l_\mathrm{p}^2 \end{array}\right\} \frac{k_B T}{\xi N} t_{\mathrm{crossover}} = \left\{\begin{array}{ll} \left(\frac{N l_\mathrm{b}^2}{d_\mathrm{T}}\right)^2 & \text{flexible} \\ \\ L^2 & \text{semiflexible} \end{array}\right. \,. \tag{2.40}$$

In the flexible case the diffusion coefficient is with $\langle r^2 \rangle_{\mathrm{crossover}} = N l_{\mathrm{corr}}^2$ (l_{corr} the respective correlation length of the tube)

$$D_\infty = \frac{l_\mathrm{b} N_\mathrm{e}^{1/2} \frac{N l_\mathrm{b}^2}{d_\mathrm{T}}}{\frac{\xi N}{k_B T}\left(\frac{N l_\mathrm{b}^2}{d_\mathrm{T}}\right)^2} = \frac{k_B T}{\xi N} \frac{l_\mathrm{b}^2 N_\mathrm{e}}{N l_\mathrm{b}^2} = \frac{k_B T}{\xi N} \frac{N_\mathrm{e}}{N} = \frac{k_B T}{\xi N} \frac{l_\mathrm{e}}{L}, \tag{2.41}$$

where $d_\mathrm{T} = l_\mathrm{p} N_\mathrm{e}^{1/2}$ is the tube diameter in the flexible case. The corresponding expression with semiflexibility is

$$D_\infty = \frac{l_\mathrm{p} L}{\frac{\xi N}{k_B T} L^2} = \frac{k_B T}{\xi N} \frac{l_\mathrm{p}}{L}. \tag{2.42}$$

The criterion to decide, which of the two models applies, is that the persistence length is smaller than the tube diameter. The tube diameter, however, shrinks with increasing stiffness as the chain cannot explore transversal degrees of freedom. So the second scenario arises already at moderate stiffness.

Another way of seeing this is, that one may define two tube diameters. A very tight $d_{\mathrm{T1}} \approx l_\mathrm{b}$ emanating from the local stiffness and a second wider d_{T2} arising from the topological constraining. This concept is especially helpful in the range of intermediate stiffness where the diffusion coefficient shows two Rouse-like plateaus if DN is plotted against N (sec. 5.3).

Depending on l_p there are now three possible scenarios (fig. 2.12):

1. $l_\mathrm{p} < d_\mathrm{T}$: The standard reptation model holds.

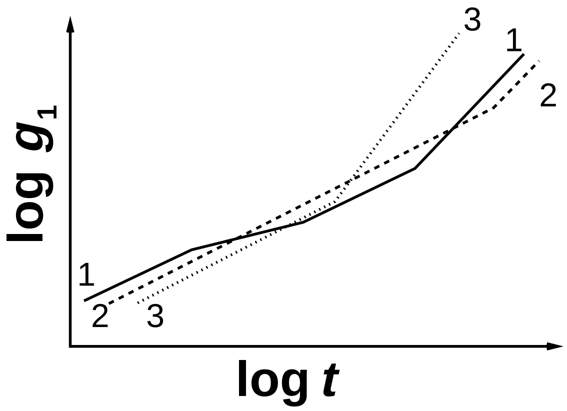

Figure 2.12: Possible intersection patterns for mean-square displacements of central monomers ($g_1(t)$) of flexible and stiff chains. The solid curve denotes the standard reptation picture. The dashed line is the second intermediate case and the dotted line is the very stiff case (leading to nematic order).

2. $d_\mathrm{T} < l_\mathrm{p} < l_\mathrm{e}$: The mean-squared displacements of a flexible and the semiflexible chain intersect twice, because the semiflexible chain is faster in the reptating dynamics but slower in the final diffusion.

3. $l_\mathrm{p} > l_\mathrm{e}$: The mean-squared displacements intersect once. The semiflexible chain is faster in the final diffusion as well. However, for such persistence lengths, the nematic state would be reached (for the densities interesting for this work). In this case, the speedup is, however, obvious, as the diffusion in a nematic liquid crystal along its director is fast.

The second intersection of the second scenario could not yet be found in simulations, as the simulation times were too short.

2.5 Fundamentals of NMR in polymers

In order to study experimentally the reorientation of chain segments one can apply nuclear magnetic resonance (NMR). With NMR the relaxation of magnetization arising from nuclei is investigated. Therefore, only elements with nuclei which do have a non-zero magnetic moment are observable by NMR. Luckily, the hydrogen nucleus ^{1}H has a magnetic moment, as does the isotope deuterium ^{2}H. The normal carbon nucleus ^{12}C has no magnetic moment. One has to exchange it with the isotope ^{13}C. By selective isotope exchange, vectors between distinct nuclei can be monitored in NMR experiments.

An interesting observable for polymer dynamics is the reorientation of bond-vectors. Two neighboring nuclei interact by their magnetic moments and are, therefore, recordable by NMR. The reorientation of vectors between well-defined atoms can be monitored selectively. NMR can only investigate *directors*. A director can be regarded as a vector with indistinguishable ends.[2]

Recent NMR experiments on different entangled polymers have shown remarkable differences in the local scale dynamics depending on chain stiffness. In contrast to poly-(dimethylsiloxane) (PDMS) which follows almost perfectly the reptation model [CS98], poly-(butadiene) (PB) experiments show considerable deviations which are taken as indications of local order [GHS98]. There is a high degree of order for $t \to 0$ which cannot be explained by reptation. In the case of poly-(ethylene-oxide) (PEO) deviations from reptation behavior are observed as well [CS98]. PDMS is one of the most flexible polymers and, therefore, well suited for direct comparison to simple theoretical bead-spring models. PB, however, is locally stiff and has an alternating flexibility along its backbone originating from the sequence of alternating single and double bonds.

---

[2] Actually, a director is a symmetric traceless second rank tensor

On the basis of the reptation model one can calculate dynamic exponents for the reorientation of polymer chain segments with time [BCS97]. As the degree of entanglement increases (with increasing chain length or correspondingly decreasing entanglement length), the reorientation dynamics of the chains slows down tremendously.

2.5.1 Reorientation and double quantum correlation functions

To describe the reorientation dynamics of local chain segments, one defines the auto-correlation function of the second Legendre polynomial of a chain tangent vector

$$C_{\mathrm{reor}}(t) = \left\langle \frac{1}{2}\left[3\left(\vec{u}(t)\vec{u}(0)\right)^2 - 1\right]\right\rangle . \tag{2.43}$$

In appendix A it is shown that the experimentally accessible double quantum correlation function C_{DQ} is proportional to C_{reor} under the assumption of an isotropic distribution of the unit vectors at all times. C_{DQ}, which was determined for polybutadiene for instance [Gra98, GHS98], is defined as [SRS94]

$$C_{\mathrm{DQ}}(t) \equiv \left\langle P_2\left[\vec{B}\vec{u}(0)\right] P_2\left[\vec{B}\vec{u}(t)\right]\right\rangle \tag{2.44}$$

$$\overset{\text{isotropy}}{=} \frac{1}{5} C_{\mathrm{reor}}(t) . \tag{2.45}$$

$\vec{u}$ is a unit vector. As for the reorientation behavior one normally is interested in vectors along the backbone but experimentally monitors atom-atom vectors it can be necessary to transform between them. $\vec{B}$ is a unit vector parallel to the external magnetic field in the NMR experiment. Its direction is arbitrary in the analysis of isotropic simulations since no magnetic field is involved. Thus, $\vec{B} = \hat{e}_z$ can be chosen for convenience.

2.5.2 Dynamical order parameter

From NMR measurements for entangled systems residual order effects can be inferred. One of the central observables is the *residual dynamical order parameter* [CA74, SRS94]

$$\mathcal{S}(t) = \left\langle P_2(\alpha)\right\rangle_t . \tag{2.46}$$

The angle α describes the orientation with respect to the external field $\vec{B}$. This dynamical order parameter yields the residue of orientation correlation after time-averaging over (possibly anisotropic) fast local motions, i.e. t is the length of the time interval. For a fully isotropic movement $\mathcal{S}$ would vanish, in rigid systems it stays at $\mathcal{S} = 1$. The local motional anisotropy leads to a non-vanishing time average

$$\mathcal{S}(\tau_{\mathrm{e}}) = \frac{1}{\tau_{\mathrm{e}}} \int_0^{\tau_{\mathrm{e}}} \mathrm{d}t\, P_2(t) \tag{2.47}$$

up to the entanglement time τ_{e}, the time when the chain experiences its surrounding as a constraining tube.

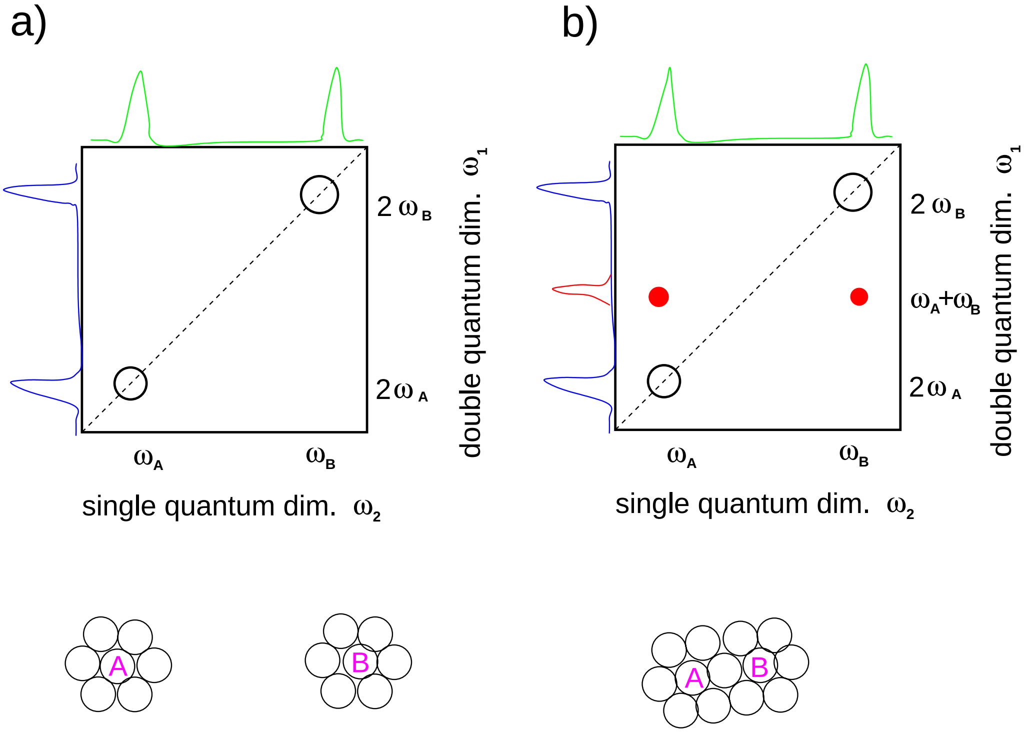

Figure 2.13: Two different two-dimensional NMR spectra. In part a the two spins *A* and *B* are well separated and do not give rise to double quantum coherences. In part b they are close enough to interact. Thus, the two coherence peaks (marked in red) arise (compare [Gra98]).

2.5.3 Double quantum experiments

To focus on the reorientation correlation C_{reor} of distinct vectors one has to be able to identify the atoms constituting the vector. This is possible without isotopic exchange if *multidimensional*, i.e. multi quantum, NMR is applied. In the following the discussion is restricted to the double quantum case. Double quantum transitions are forbidden in the sense of second order quantum mechanical perturbation theory. Two quanta have to be absorbed for the transition. Therefore the experiment is inherently two-dimensional in the frequency domain. Two interacting spins result in different two dimensional patterns from the ones of two separate spins. Figure 2.13 shows the two cases with the corresponding twodimensional patterns [Gra98]. In the single quantum dimension ω_2[3] the two spectra do not differ, i.e. only double quantum experiments are able to elucidate the discrepancies as the respective chemical shifts of the nuclei are correlated. These double quantum coherences allow now double quantum filtering of the spectra to resolve “interesting” vectors from the background of all the rest. The experiments for polymer dynamics are therefore possible in simple melts without any substitution [GHS98].

Double quantum experiments work in the following manner. A sequence of electro-magnetic pulses (radio frequency) is radiated into the sample to excite the relevant spins. After an evolution time t_{evolve} the spin signal is reconverted by a pulse sequence which corresponds exactly to the adjoint propagator of the preparation pulse. Then the signal is detected (fig. 2.14). For the specific

---

[3] ω_1 typically denotes the double quantum dimension.

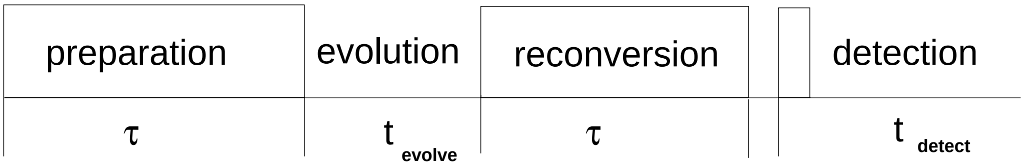

Figure 2.14: The double quantum NMR experiments consist of four different phases.

pulse sequences for the different purposes see the literature on NMR [SRS94, Gra98].

By quantitative analysis of the amplitudes of these spectra one can e.g. infer reorientation in polymer melts which is of interest for the present work. The intensity of the double quantum intensity at the end of the reconversion phase is [Gra98]

$$I_{\mathrm{DQ}} = \langle \sin(|\omega_{ij}(\beta,\gamma)| t_{\mathrm{prep}}) \sin(|\omega_{ij}(\beta,\gamma)| t_{\mathrm{reconv}}) \rangle_{\beta,\gamma} \ . \tag{2.48}$$

The average over β and γ means averaging over all possible orientations of the spin pair. For weak excitation intensities this can be linearized. Additionally the two times are the same because of the adjoint propagators which results in

$$I_{\mathrm{DQ}} = A \overline{F}^2_{\mathrm{pulse}} D^2_{ij} t^2_{\mathrm{prep}} e^{-t_{\mathrm{prep}}/\tau_{\mathrm{DQ}}} \ . \tag{2.49}$$

The factor $\overline{F}^2_{\mathrm{pulse}}$ depends on the exact pulse sequence and can be calculated; D_{ij} is the dipolar coupling constant between the spins in which one is interested. It is dependent on the distance vector between the spins. The exponential is an attenuation of the signal with a single time constant again depending on the pulse sequence used. The amplitude A is measurable by an independent experiment without the preparation and reconversion phase. The dipolar coupling strength is now a measure of the interaction of the spins, i.e. how strong they are coupled or how dependent their positions are. D_{ij} can be again separated in

$$D_{ij} = D_{ij}(r) P_2(\Theta) \tag{2.50}$$

which is exactly what one needs to look for the reorientation function. By this method the function (2.44) is accessible.

2.5.4 Spin-lattice relaxation time

Another experimental observable for local polymer dynamics is the time T_1 in which the magnetization of the spin system relaxes. It is often called the spin-lattice relaxation time [Sli90]. For melts of *cis*-1,4-polyisoprene, for example, this value was determined by Dejean de la Batie *et. al.* [DLM89]. They interpreted their data as a fast, local anisotropic reorientation by segmental motion. The relationship between the reorientation correlation function and the spin-lattice time for a C-H vector reads [LS82a, DLM89]

$$\frac{1}{T_1} = \frac{\hbar^2 \gamma_{\mathrm{C}}^2 \gamma_{\mathrm{H}}^2}{10 r^2_{\text{C-H}}} \Big[J(\omega_{\mathrm{H}} - \omega_{\mathrm{C}}) + 3J(\omega_{\mathrm{C}}) + 6J(\omega_{\mathrm{H}} + \omega_{\mathrm{C}}) \Big]. \tag{2.51}$$

The γ_i are the gyro-magnetic ratios of the respective nuclei and ω_{C} and ω_{H} are the Larmor frequencies, r is the distance between the nuclei. The function $J(\omega)$ is the spectral density, i.e. the

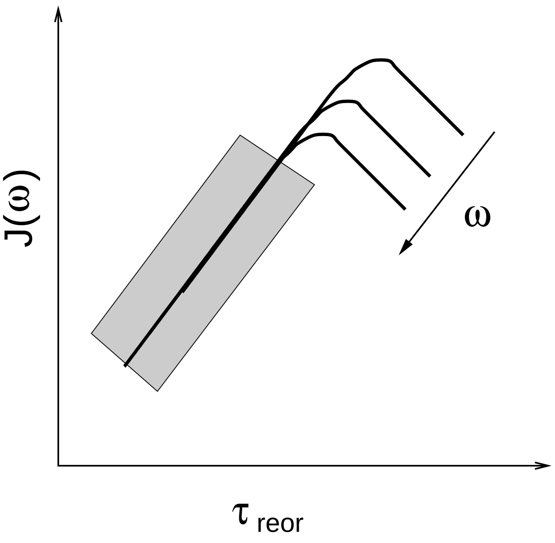

Figure 2.15: The extreme narrowing limit is reached for times in the shaded area on the left hand side. For longer times the spectral density becomes frequency dependent.

Fourier transform of C_{reor} of the respective vector

$$J(\omega) = \frac{1}{2}\int_{-\infty}^{\infty} C_{\mathrm{reor}} e^{i\omega t}\mathrm{d}t \ . \tag{2.52}$$

In atomistic simulations T_1 has been determined for different polymers [ME96, PSY97, AST98]. Moe and Ediger use the limit of *extreme narrowing* to analyze their *cis*-polyisoprene data at T $=$ 413 K, as is done in most other atomistic simulations [ME96]. This has the advantage that T_1 becomes independent of the respective Larmor frequencies [KBB84], which cannot be directly measured in simulations. The spectral density $J(\omega)$ is for very short times independent of ω as it reads:

$$J(\omega) = B_{\mathrm{local}}^2 \frac{2\tau_{\mathrm{reor}}}{1+\omega^2\tau_{\mathrm{reor}}^2} \ . \tag{2.53}$$

Figure 2.15 shows that for short times $J(\omega)$ is directly proportional to the reorientation. However, the *extreme narrowing* regime ($\omega\tau_{\mathrm{reor}} \ll 1$)is not reached normally by the experiments, as high temperatures are needed to yield short enough correlation times.

The reorientation time τ_{reor} is defined by the time integral over the correlation function

$$\tau_{\mathrm{reor}} = \int_0^{\infty} C_{\mathrm{reor}}\mathrm{d}t \ , \tag{2.54}$$

and in the extreme narrowing limit this is directly related to the inverse T_1 time for a C$-$H vector

$$T_1^{-1} = 10nK\tau_{\mathrm{reor}} \ , \tag{2.55}$$

whereby K is a constant related to the bond length and n is the number of protons connected to the respective ^{13}C.

2.5.5 NMR and reptation

For the interpretation of NMR data the reptation model is often used [SRS94]. Since the characteristic decay time of the dipolar interaction strength (M_2, measured in 1/s^2) is about 1 µs, one can

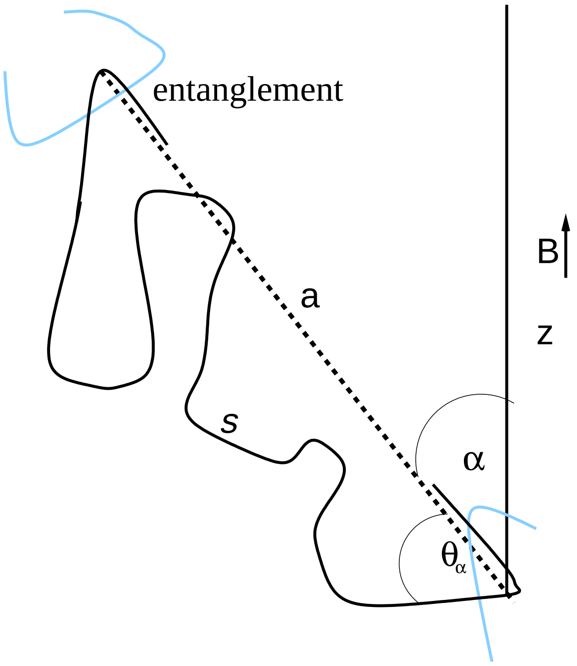

Figure 2.16: Illustration of a polymer between entanglements (compare [BCS97]). The solid black line represents a polymer "entangled" by the blue polymers. The straight part of the tube is given by the dashed primitive path which is inclined to the z-axis (magnetic field direction) by an angle α. The angle Θ_α denotes the direction of the polymer with respect to the tube.
As one cannot really pin down entanglements to points in space, this picture is only to be taken as an illustration of the concept.

infer that a massive pre-averaging over the fast motion occurs on experimental time scales (which are in the millisecond range) [BCS97, GHS98] leading to

$$\overline{M_2} = M_2 \left[\left\langle P_2(\Theta_\alpha) \right\rangle_{\text{fast}} \right]^2 . \tag{2.56}$$

Θ_α is the angle between a vector $\vec{u}$ (e.g. C–H or H–H vector) and the primitive path of the reptation tube $\vec{a}$, which itself is inclined by an angle α against the direction of the field $\hat{e}_z$ (see figure 2.16). The influences of entanglements on the chains lead then to a non-vanishing dynamical order parameter.

Motion along the primitive path and reorientation

Ball *et al.* derived expressions for the decay of the orientation correlation function C_{reor} in the reptation model [BCS97]. This derivation is sketched here.

In a homogeneous melt there are no preferred directions or alignments. All the chains are randomly oriented but they cannot move randomly due to the excluded volume constraint. Thus, the final reorientation can only take place by motion along the tube. The initial decay is due to local reorientations inside the tube.

The displacement of a curvilinear chain segment with time is denoted by $s(t)$. Its average orientation after the initial decay with respect to the z-axis (denoting the magnetic field) is described

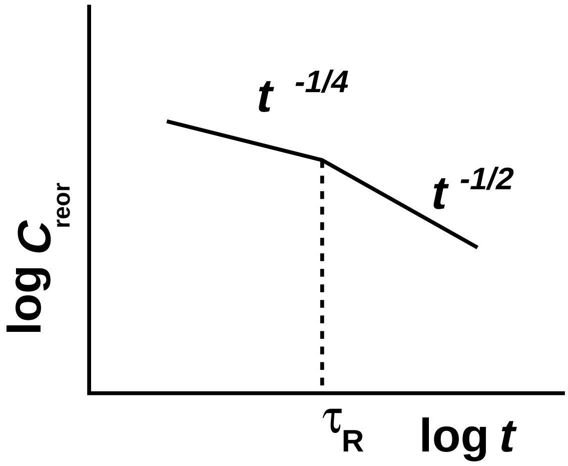

Figure 2.17: The scaling regimes in the reorientation correlation function expected if the reptation model is assumed. The kink occurs at the Rouse time τ_R.

by an orientation cosine given by $\frac{\partial z(s)}{\partial s}|_{s(t)}$.[4] The (time-dependent) second Legendre polynomial then reads

$$P_2[\cos\alpha(t)] = \frac{3}{2}\left[\left(\frac{\partial z(s)}{\partial s}\bigg|_{s(t)}\right)^2 - \left\langle\frac{\partial z(s)}{\partial s}\right\rangle\right] . \tag{2.57}$$

If the tube is not relaxed ($t < \tau_\mathrm{d}$), $P_2[\cos\alpha(t)]$ is a stationary random function $P(s)$ with a correlation length of the order of the Kuhn length l_K, as the tube direction imposes the chain orientation and the correlation length of the tube is expected to be in the order of the segment length.

For the motion along the primitive path in an infinite tube one can write for the correlation function of the Larmor frequencies relevant for NMR

$$\Big\langle\omega(t)\omega(0)\Big\rangle = \overline{M}_2\Psi_\mathrm{RTO}(t) , \tag{2.58}$$

$$\Psi_\mathrm{RTO} := P\Big(s, t\Big|\Big\langle\Big[s(t) - s(0)\Big]^2\Big\rangle \le l_\mathrm{K}^2\Big) , \tag{2.59}$$

where Ψ_RTO is the return-to-origin probability, defined as probability to come back to a point closer than l_K to the original position. The reorientation function can be calculated from this. The result is

$$\Psi_\mathrm{RTO} \propto \begin{cases} (t/\tau_\mathrm{e})^{-1/4}, & \tau_e < t < \tau_\mathrm{R} \approx (N/N_\mathrm{e})^2\tau_\mathrm{e} \\ (t/\tau_\mathrm{e})^{-1/4}(t/\tau_\mathrm{R})^{-1/4}, & \tau_\mathrm{R} < t < \tau_\mathrm{d} \approx (N/N_\mathrm{e})\tau_\mathrm{R} \end{cases} . \tag{2.60}$$

The reorientation correlation function exhibits the same power-law behavior as Ψ_RTO. So in the second and third dynamic regime of the reptation model C_reor decays with $t^{-1/4}$ and $t^{-1/2}$ respectively (fig 2.17). These exponents are just the negative of the exponents one encounters for the mean-squared displacements of inner chain monomers (sec. 2.3).

---

[4] The derivative of a parametrically described curve with respect to its length (the contour coordinate) is the tangent vector. Taking only the z-component is equivalent to the scalar product with the direction vector.

3 Methods for polymer simulations

Computer simulation has become an important means for the investigation of complex materials. In principle, simulations allow access to all possible observables of the system at all times, because positions of all particles are available. The only limitation of simulations is the limitation of the model (Hamiltonian, system size, simulation time, ergodicity) and the power of the used computer. There is no *a priori* reality in the simulation data, itself as they are mere numbers. Only the model allows their interpretation. They have to be compared to theory and experiment in order to check their content of reality or physical significance.

Comparison to experiments is not only possible with “final” results, which are often derived by interpretation using a model, but more directly at the stage of experimental raw data. This is an important issue in order to understand complex experiments. Often raw data have to be processed by models and theories in order to obtain interesting observables. Thus, simulations can and should be validated against raw data, and both should be interpreted together [MPSF00]. The validation shows how much “reality” can be assigned to the model under study.

In this work purely classical molecular dynamics simulations are presented because quantum mechanical degrees of freedom are not deemed relevant. They could, however, be introduced, e.g. by Car-Parinello molecular dynamics [CP85] or other approaches [BvGMP98]. Then the simulation times and system sizes would be limited even more.

A central problem is the time and length scales which can be reached in reasonable computer time. As the relevant time scales range from 10^{-13}s for bond vibrations up to milliseconds and beyond for macroscopic rheologic relaxations, one has to think about what detailed system information is necessary. Naturally the problem of *coarse graining* arises [BBD$^+$00]. All atom simulations contain one interaction site for every atom and therefore allow access to all atoms. The length scales are of the order of a few Ångstrøm. Such detailed information is not always necessary or even wanted because it obscures the individual influences of the different interactions. Simulations with less details but larger time and length scales are desirable.

A first widely applied step is the use of so called united atoms (UA) models, taking only the heavy atoms into account, while the hydrogen atoms are incorporated into the neighboring heavy atoms [WH79, PSY97, HMT98]. They are quite successful and allow a moderate increase of the time step. The next step is coarse-graining of whole monomeric units onto one interaction center, which sacrifices more information for the sake of speedup and clarity. One can even go so far as mapping a whole chain onto one “fluffy ellipsoid” [MK98].

In the subsequent chapters various methods are applied on different levels of detail to simulate polymers. Figure 3.1 gives an overview of the methods and their use in this work.

3.1 Molecular dynamics

Molecular dynamics (MD) is a widely used simulation technique in various fields of physics and chemistry [AT87, vGB90, Hai92, Bin95, BC96, FS96]. It relies on the stepwise time integration

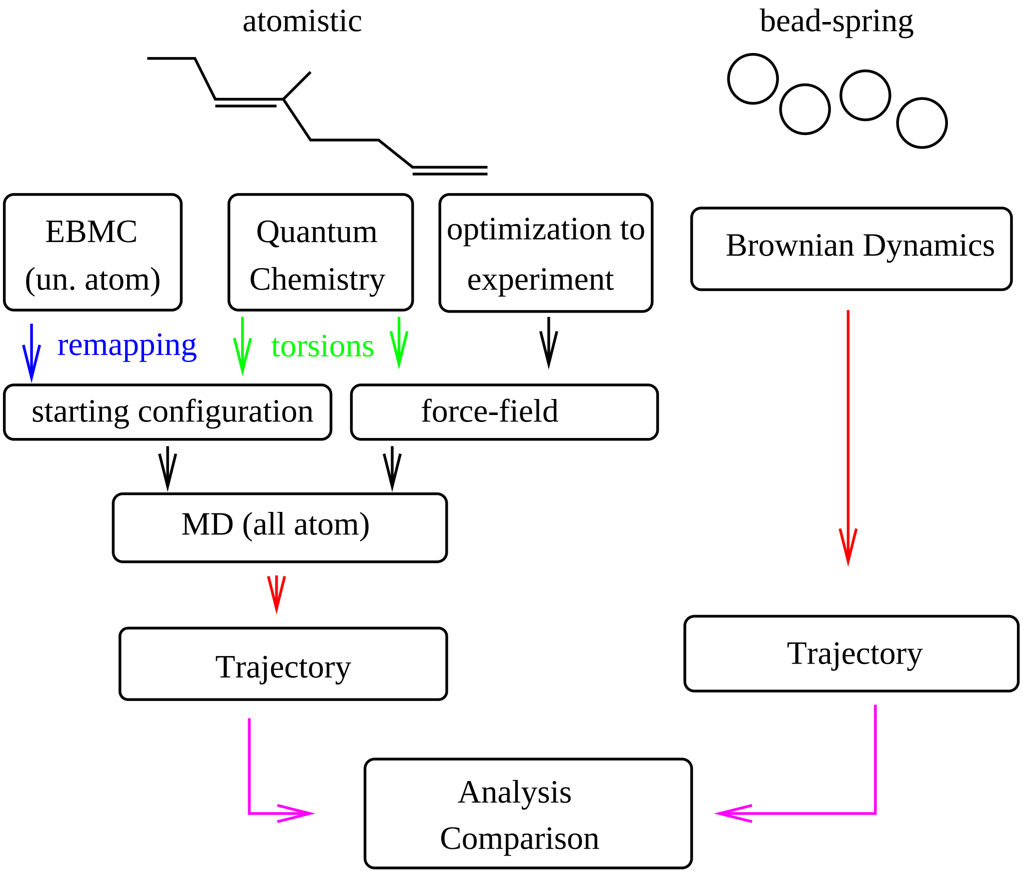
atomistic
bead-spring
EBMC (un. atom)
Quantum Chemistry
optimization to experiment
Brownian Dynamics
remapping
torsions
starting configuration
force-field
MD (all atom)
Trajectory
Trajectory
Analysis Comparison

Figure 3.1: Overview of the different methods for simulations at the different levels of detail.

of Newton's equations of motion

$$m_i \frac{\mathrm{d}^2\vec{r}_i}{\mathrm{d}t^2} = -\nabla V\Big(\{\vec{r}_j\}\Big) \, . \tag{3.1}$$

Here m_i denotes the mass of the particle i under consideration, $\vec{r}_i$ its position and $V(\{\vec{r}_j\})$ the potential energy function depending on the whole set of particle positions. In the limit of time step to zero, MD becomes correct as long as a classical description of the system is appropriate.

As Newton's equations are not questionable, the main ingredient of MD simulations is the proper choice of the potential energy function $V(\{\vec{r}_j\})$, often called a "force-field", for the system under study. There are several strategies, one may even say philosophies, to develop force-fields. On the very local end detailed atomistic force-fields are necessary in order to describe reliably the differences between the different atom types in the respective environment. In section 6.2 the development of an atomistic force-field for polyisoprene simulations is described in detail. For more generic issues less detailed and, hence, computationally more efficient interaction potentials are better suited. Here only generic features such as volume exclusion, connectivity or semiflexibility are of relevance.

Normally, the dynamical equations used in the simulations are not directly Newton's equations. They conserve volume and total energy and, thus, lead to the micro-canonical ensemble, which is most often neither experimentally relevant nor theoretically convenient. Yet, the equations of motion have to be changed to work with constant temperature instead of constant energy or constant pressure instead of constant volume. This corresponds to Legendre-transformations to the canonical (NVT) or the isothermal-isobaric (NpT) ensemble. It is even possible to apply the grand- or semi-grand-canonical ensembles which allow particles to be created, annihilated or change identity [FS96].

The simulations presented in this thesis use constant temperature and either constant volume or constant pressure. Constant temperature is either ensured by simulating Brownian dynamics [GK86] or by Berendsen's method [BPvG$^+$84]. The latter is applied for constant pressure as well.

3.1.1 Integrator

There are several approaches for the integration of the equations of motion. The *integrator* together with the force calculation is the "heart" of any MD program. The *Verlet* integrator and its *leap-frog* variant are commonly used in MD simulations [Ver67, Hoc70, AT87, FS96]. The leap-frog algorithm reads as follows

$$\vec{r}_i(t+\Delta t) \;=\; \vec{r}_i(t) + \Delta t\, \vec{v}_i\left(t + \frac{1}{2}\Delta t\right) \, , \tag{3.2}$$

$$\vec{v}_i\left(t + \frac{1}{2}\Delta t\right) \;=\; \vec{v}_i\left(t - \frac{1}{2}\Delta t\right) + \frac{\Delta t}{m_i}\vec{F}_i\Big[\vec{r}(t)\Big] \, . \tag{3.3}$$

$\vec{r}_i$ and $\vec{v}_i$ are positions and velocities of particle i. The force $\vec{F}_i$ is the sum of all (pair) forces acting on the particle. It is calculated from the force-field $V(\{\vec{r}_j\})$. All Verlet algorithms have the advantage that they are correct to order $O(\Delta t^3)$ and preserve time inversion symmetry. Additionally, they are symplectic, i.e. they preserve the volume in phase-space. However, in the leap-frog formulation velocities and positions are not known at the same point of time. They are "leap frogging" each other. If one needs to know both at a time the velocity has to be interpolated between $\vec{v}(t + 1/2\Delta t)$ and $\vec{v}(t - 1/2\Delta t)$.

3.1.2 Berendsen method for constant temperature and pressure

The above mentioned Berendsen method for thermostatting and keeping constant pressure works as follows: particle velocities or, for constant pressure, the size of the simulation box (edge length l) and all particle positions are adapted in a first order way so that the corresponding observables T and p approach the desired target values

$$l^{(\mathrm{new})} = l^{(\mathrm{old})} \left(\frac{\kappa_T}{\tau_\mathrm{p}} \left[p - p^{(\mathrm{target})} \right] \right)^{1/3} . \tag{3.4}$$

With respect to constant pressure equation (3.4) shows that in every time step the length of the simulation box is scaled according to the difference between the present pressure and the target pressure. The relaxation time τ_p is to be chosen much greater than the time step Δt. κ_T is the isothermal compressibility which cannot be calculated directly with this method.[1] This algorithm breaks by its first-order nature time inversion symmetry. Therefore, the algorithm has to be applied with some caution. If one uses this rescaling of the box (or any other rescaling algorithm) one has to be very careful if displacements are calculated for dynamical quantities. The rescaling may cause unphysical particle displacements, since not only the overall box size but all particle positions have to be rescaled uniformly [SFMP99]. By simply rescaling the particle positions, a specific origin of the coordinate system is defined and particles far away from this arbitrary chosen point are affected more strongly than the ones in its vicinity.

3.1.3 Brownian Dynamics

In Brownian dynamics a Langevin equation is simulated instead of Newton's equation [GK86]

$$m_i \frac{\mathrm{d}^2 \vec{r}_i}{\mathrm{d}t^2} = -\nabla V\left(\{\vec{r}_j\}\right) - \xi \frac{\mathrm{d}\vec{r}_i}{\mathrm{d}t} + \vec{f} . \tag{3.5}$$

The heat bath of the canonical ensemble is represented by the stochastic force $\vec{f}$, uncorrelated in time and space with vanishing mean $\langle \vec{f} \rangle = 0$, acting on the particles and the friction constant ξ. The friction and the strength of the stochastic force are at a defined temperature T connected by the fluctuation-dissipation theorem (compare eq. (2.15)).

A problem may be the local (and even global) non-conservation of momentum. The center of mass which would stay in place for momentum conservation moves like a Brownian particle. One would need dissipative particle dynamics for this purpose, where the random forces are applied as pair forces [GW97]. However, in dense melts this is no problem, as long range momentum transport is of no relevance.

3.2 Monte Carlo

A completely different approach in computer simulations is Monte Carlo (MC). As a Monte Carlo scheme is applied for equilibrating atomistic simulations, the basics of MC are briefly summarized.

The purpose of MC is to calculate the partition function of a system with a given Hamiltonian. From a statistical mechanics point of view everything is known about a system with the partition function. In contrast to molecular dynamics, Monte Carlo is no dynamical way of wandering through phase space. One does not follow the actual physical trajectory although there are some dynamical Monte Carlo procedures [CK88, HvdE99]. In principle every "short-cut" is allowed as long as the algorithm samples the conformation space in a correct manner. By sampling all available phase space the system would be characterized completely. As sampling all states of a system is far out of reach of simulations even for very simple systems, one has to think of clever ways to sample a representative subset from which the true partition function of the whole system can be deduced.

---

[1] In order to calculate the compressibility one would have to simulate constant volume at different volumes and calculate the respective pressures. Then the compressibility is available by finite differences. The fluctuations produced by the Berendsen method are not completely correct [PM96].

For Monte Carlo one needs a Hamiltonian (for most cases only consisting of the potential energy, i.e. the same $V(\{\vec{r}_i\})$ as in section 3.1) depending on the state of the system, i.e. in our case the particle positions

$$H = H\Big(\{\vec{r}_i\}\Big). \tag{3.6}$$

Any change of position of one or more particles changes the value of the energy. MC now works by trying to change the system state. For the new state the value of the Hamiltonian H is calculated. This new state is accepted if the so-called Metropolis criterion is fulfilled [MRR$^+$53]: if the energy is lower in the new the state, it is accepted in any case. If it is higher it is accepted with a probability corresponding to the Boltzmann factor $e^{-\beta H}$ with $\beta = {}^{1}\!/_{k_B T}$. The ground state of the system is the one with lowest energy. States with moderately higher energies are accessible at finite temperature and therefore contribute to the partition function. This makes the acceptance of "uphill" moves necessary.

Most Monte Carlo approaches aim at calculating the partition function in the canonical or in the NpT ensemble. In order to calculate the canonical partition function, it is sufficient that *detailed balance* is fulfilled [FS96]

$$\mathcal{K}(a \to b) = \mathcal{K}(b \to a)\ . \tag{3.7}$$

The flow $\mathcal{K}(a \to b)$ from configuration a to configuration b has to be the same as the back flow. One has to ensure that no net flow occurs, which is a definition of equilibrium. The flow between two states consists of three parts: the probability $p(a)$ of being in state a, the probability of generating the new trial configuration $q(b, a)$, and the probability of accepting the move $p_{\mathrm{acc}}(b, a)$

$$\mathcal{K}(a \to b) = p(a)q(b, a)p_{\mathrm{acc}}(b, a)\ . \tag{3.8}$$

For all Monte Carlo moves used in the following detailed balance was proved. Still, Monte Carlo is not used for production runs on any system but, rather, to produce independent starting configurations for molecular dynamics simulations.

3.2.1 End-bridging Monte Carlo

The Monte Carlo procedure used to equilibrate atomistic polyisoprene melts applies a modern *end-bridging* Monte Carlo move (EBMC). The end bridging method was originally developed for polyethylene by the group of D. Theodorou [KT95] at Berkeley and later Patras university and adapted to *cis*-polyisoprene by Manolis Doxastakis [Dox]. For the purpose of this work, their program was changed to *trans*-polyisoprene. The Monte Carlo simulations use a united atom model, because the hydrogens in atomistic simulations can be neglected for the long length-scale structure. Hydrogen atoms only complicate the procedure unnecessarily. Therefore, a coarse-graining and remapping procedure for taking out and reintroducing the hydrogens into their rest positions

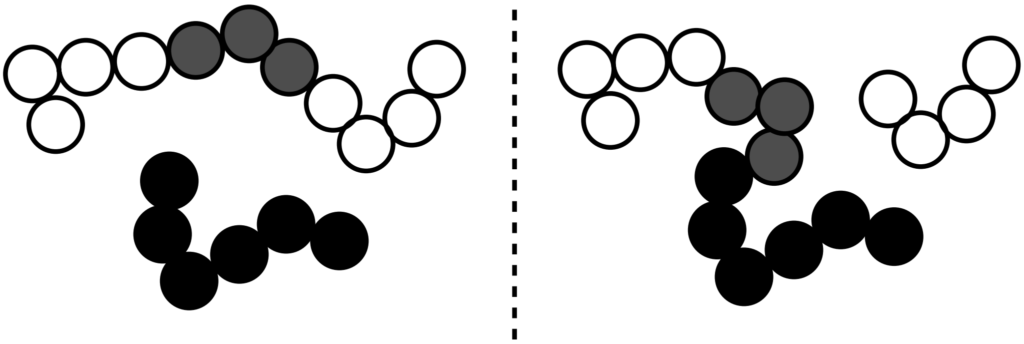

Figure 3.2: The end-bridging move: The black chain “attacks” the white chain. The gray monomers are displaced during the move.

is necessary. The interaction sites for the united atoms are chosen to be the carbon positions; after EBMC the hydrogen atoms are reintroduced geometrically into their rest positions.

EBMC works as follows: a chain end close to a neighboring chain “attacks” that chain. The “victim” chain is now split into three parts, the middle one being a trimer. One end remains as a shorter chain, keeping the “identity” of the victim. The other end merges together with the attacking chain, where the intermediate trimer is rebuilt as link between the parts. This is illustrated in figure 3.2. There may be cases where for given bond lengths and angles there is more than one or no torsion configuration for the trimer to satisfy the conditions. In the case of multiple solutions, all of them are included in the calculation and acceptance is checked. For a detailed description of the geometric problem of connecting two given chains by a trimer with fixed lengths and bond angles see ref. [MBZT99]. There one finds also benchmarks for the application of this method to different systems. As end-bridging changes the topology of the chain, polydispersity cannot be avoided.

For simple systems like polyethylene this method can be directly applied as it stands. For polyisoprene a more elaborate strategy is necessary. Since end-bridging moves use trimers and the topology of the polyisoprene monomer must not be altered, each chain carries a *hypothetical* chain with it (fig. 3.3). The hypothetical chain in the case of *trans*-polyisoprene consists of the carbons C_1, C_4, and C_5. Their positions define uniquely the rest positions of the corresponding C_2 and C_3. All end-bridging moves were performed in the hypothetical chain picture. The other two carbons were then reintroduced and the MC run continued. The geometrical solution of the bridging problem is obtained using the hypothetical chain.

In addition to this MC move other moves are integrated into the simulation. A configuration-biased reptation (CBR), which uses the hypothetical chain as well, is applied [dLS92]. It works as follows: a whole (hypothetical) monomer is built step by step in several different torsional states at one end while being cut off at the other. The different torsional states, from which the best is selected, are necessary in order to come to reasonable acceptance rates in dense melts. Of course, precautions have to be taken that the move is reversible and that the rates are correct in order to keep detailed balance. For CBR as wells as EBMC this has been proved [dLS92, KT95, MBZT99].

Additional moves which were applied include torsional rotations of chain ends around one or more of the bonds between the last and second last monomer as well as volume fluctuations in order to run at constant pressure and concerted rotations (intra-chain rebridging) [DBT93] which are similar to end-bridging. Here a trimer is cut out of the middle of a chain. The two neighbors

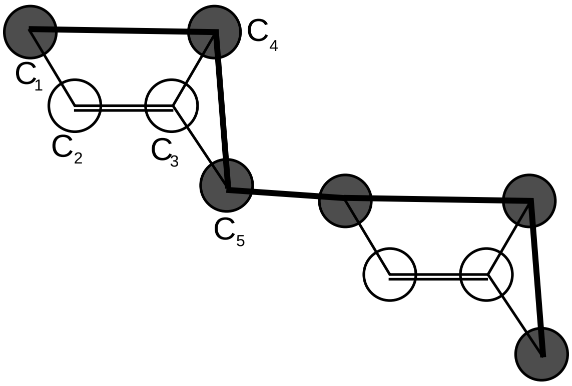

Figure 3.3: The hypothetical chain used in the Monte Carlo procedure. The gray trimers are taken as the trimers for bridging in the end-bridging MC. The white atoms are reinserted after the move is completed.

are then displaced and the trimer is rebuilt into the new position.

3.3 Bead spring model: Interaction potentials and description of the system

A widely used model for polymer simulations is applied in chapters 4 and 5 [GK86, KGC88, RR88, KG90, TR91, DGK98, Bar00]. A slightly changed variant of the program POLY by M. Pütz was used [PK98, Püt99].

The non-bonded interactions are purely short-ranged and repulsive. A Lennard-Jones potential is cut at the minimum and shifted to zero (Weeks-Chandlers-Andersen, WCA, potential [WCA71]). So it is continuous and differentiable over the whole range

$$V_{\mathrm{WCA}}(r) = 4\epsilon \left[\left(\frac{\sigma}{r}\right)^{12} - \left(\frac{\sigma}{r}\right)^{6} + \frac{1}{4} \right], \; r < r_{\mathrm{cutoff}} = \sqrt[6]{2}\sigma \; . \tag{3.9}$$

For $r > r_{\mathrm{cutoff}}$ all interactions vanish. Here, σ is the diameter of the monomers, ϵ the interaction strength and r_{cutoff} the cutoff distance. Together with the monomer mass m, σ and ϵ define the system of units used throughout the following chapters. Temperature is measured in energy units by setting Boltzmann's constant $k_B = 1$. The unit of time for this system is

$$t^* = \sigma \sqrt{\frac{m}{\epsilon}} \; . \tag{3.10}$$

Bonded monomers interact additionally by a FENE (finitely extendable non-linear elastic) potential. Together with the repulsive WCA potential this yields an anharmonic spring. As normally only weak elongations are considered, one may just think of a normal spring (fig. 3.4). The main advantage is that the computationally expensive square root is avoided:

$$V_{\mathrm{FENE}}(r) = \frac{\alpha}{2} \frac{R^2}{\sigma^2} \ln \left(1 - \frac{r^2}{R^2} \right), \; r < R = 1.5\sigma, \; \alpha = 30 \, . \tag{3.11}$$

α is the strength of the FENE spring. As the FENE potential has a finite range, one has to ensure, that bonded monomers are not torn apart farther than 1.5σ where the bond breaks. The mean bond length in this model arrives at $\langle l_{\mathrm{b}} \rangle = 0.97$.

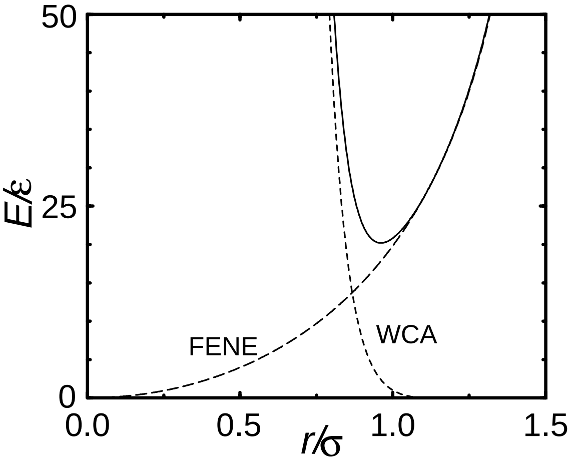

Figure 3.4: The relative strengths of the different potentials applied in the simulation except the bending potential.

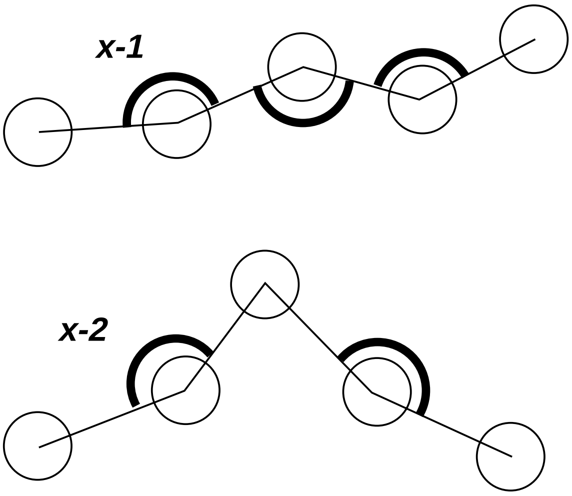

Figure 3.5: Illustration of applying the stiffening potential to every or only every second angle.

Furthermore, a stiffening potential was applied for most of the simulations in order to get a better description of real polymers. Here the discrete version of the Kratky-Porod wormlike chain model of section 2.1.2 was used

$$V_{\text{angle}} = x\left(1 - \frac{\vec{r}_{i-1,i} \cdot \vec{r}_{i,i+1}}{r_{i-1,i} r_{i,i+1}}\right). \tag{3.12}$$

x is the strength of the stiffening potential, $\vec{r}_{ij}$ is the vector connecting monomers i and j of the same chain. Not necessarily all angles were stiffened by this potential, for some systems only every second. The following naming convention applies: x: potential strength, eq. (3.12), y: distance along backbone between two applications. Thus, consequently a $x - y = 5 - 2$ polymer has a stiffening potential of strength 5 applied to every second angle (fig. 3.5). This may be used for modeling polymers with alternating stiffness along the backbone like polyisoprene or polybutadiene with their single-bond/double-bond sequence, or for copolymers with different stiffnesses of the constituents. With stronger intrinsic stiffness, such a model can be applied to investigate nematic liquid crystals [Kol99]. There is no nematic liquid crystal in the potential region ($x \leq 5$) investigated in the following. The non-crossability of the chains is not explicitly enforced. However, it is hindered by an energy barrier of $70k_BT$ high enough for all practical applications.

Brownian dynamics simulations of 500 to 2000 chains with length 2 to 1000 representing

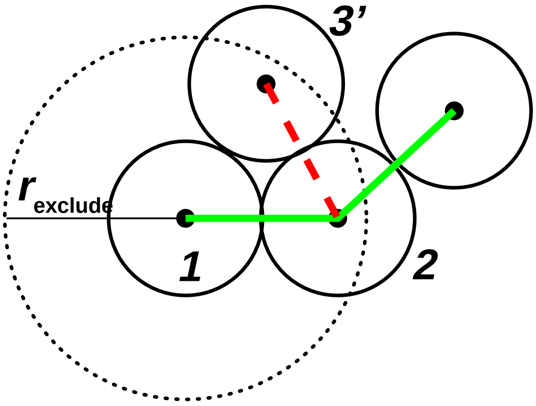

Figure 3.6: The exclusion radius used to faster equilibrate the system.

dense melts at a density of $\rho = 0.85$ were performed at a time-step of $\Delta t = 0.01$, temperature $T = 1$, and the friction coefficient $\xi = 0.5$.

3.4 Setup of melt configurations

Not only the interaction potential is crucial in simulations, but it is equally necessary to have a physically meaningful representation of the system. This means that the system has to be equilibrated carefully to let all system properties settle to their converged values. To come to feasible equilibration times, the melts were set up as non-reversal random walks. Next-to-nearest neighbors were not allowed to approach closer than a certain “exclusion radius” r_{exclude} to account for local stiffness (fig. 3.6).

The chains were set up monomer by monomer. If monomer 1 and 2 like in figure 3.6 are set, monomer 3 is not allowed to penetrate the dashed sphere. Thus, position 3’ is forbidden, whereas position 3 is allowed. This leads to a bias towards a straight conformation. The strength of the bias depends on r_{exclude}. For the first few simulation steps, the interaction potential was reduced in order to avoid technical problems because of overlapping monomers, which may be the case for monomers from different chains as well as for monomers several indices apart on the same chain. Therefore, a finite potential at $r = 0$ was introduced which avoids instabilities by the diverging force. The value of r_{exclude} was tuned by simulating short chains and afterwards deducing the end-to-end distance of longer chains. The short chains could be simulated well beyond any possible relaxation time $t_{\text{sim}} \gg \tau_R$, so that one can be sure that all static properties are equilibrated. Figure 3.7 illustrates the relaxation of the end-to-end distance in a simulation of 500 chains of length 200 with $x = 3$.

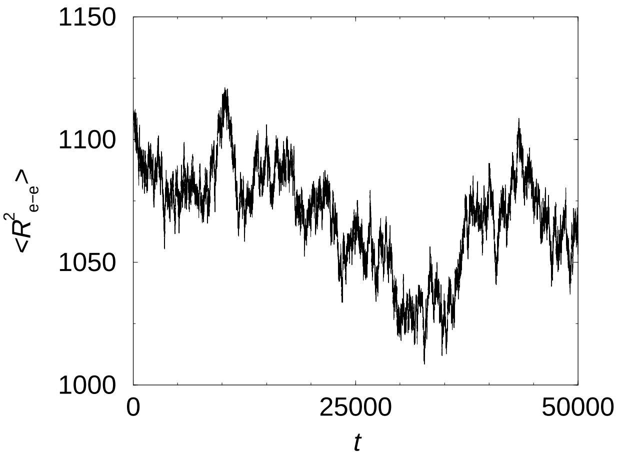

Figure 3.7: The relaxation of the end-to-end distance squared for $x = 3$, $N = 200$. The simulation was allowed to settle about three times longer than shown here before the data collection was started for these long chains. Additionally, during the production runs these observables were carefully monitored. For short chains, the first three to five Rouse times were discarded.

4 Static structure in polymer melts with local stiffness

This chapter concentrates on the investigation of the static description of the generic polymer model described in section 3.3. The influences of different strengths of local stiffening potentials are elucidated in particular. Local mutual orientations are the main focus. Additionally, the static structure of the chains and the melt is presented.

4.1 Chain sizes and persistence length

The gyration radius and the end-to-end distance are important observables in the chain statics, as they are measurable by light scattering or viscosimetry in Θ-solution[1] [HZF82, Str97]. For Gaussian chains the ratio $R^2_{\text{e-e}}/R^2_{\text{gyr}} = 6$ is expected (compare sec. 2.1). These observables are shown in table 4.1 for systems containing 500 chains each.

For the alternating bond scenario where only every second angle has a stiffening potential $(x - 2)$ this value was closely approached (tab. 4.1), i.e. about 6.1 to 6.2. But for $y = 1$ the end-to-end distance is longer than for Gaussian chains, these chains are really *semi*flexible. The radius of gyration in the simulations differs only slightly (up to 5%) from the values calculated for the wormlike chain with eq. (2.12), whereby a continuous curve is assumed (tab. 4.1). The exponential term was neglected, as it is very small. One has to keep in mind that the calculated values correspond to continuous Kratky-Porod chains, and the value for l_p is the potential strength x disregarding the melt influences, which were found to be weak. There is, however, a slight change of the persistence length.

It is not obvious whether for the $x - y$, $y \neq 1$ case the bond correlation has to follow an exponential law, as the *wormlike* chain model does not apply directly. Therefore, the applicability of the persistence length concept would be questionable, whereas the Kuhn length is defined at any rate (sec. 2.1.2). An exponential decay, however, was always found (fig. 4.1).

From a simple argument the effective persistence length in the case of persistence lengths l_{p1} and l_{p2} for alternating angle stiffness is

$$\frac{1}{l_\text{p}} = \frac{1}{2}\left(\frac{1}{l_{\text{p1}}} + \frac{1}{l_{\text{p2}}}\right) , \tag{4.1}$$

because

$$e^{-2l/l_\text{p}} = e^{-l/l_{\text{p1}}} e^{-l/l_{\text{p2}}} . \tag{4.2}$$

---

[1] Θ-solution is characterized by a vanishing second virial coefficient between two chains. The chains then perform random walks and are neither swollen nor collapsed.

System	Length	$\left(R_{\mathrm{gyr}}^{(\mathrm{sim})}\right)^2$	$\left(R_{\mathrm{gyr}}^{(\mathrm{theory})}\right)^2$	$R_{\text{e-e}}^2$	$\frac{R_{\text{e-e}}^2}{R_{\mathrm{gyr}}^2}$	l_{p}	l_{K}
$0-1$[a]	50	13±4		79±2	6.0	1.0±0.1	1.7±0.1
$1.5-1$	20	7.4±0.4	7.2	47±2	6.4	1.2±0.1	2.6±0.1
$1.5-1$	50	22±1	21.4	134±7	6.2	1.3±0.1	2.9±0.1
$1.5-1$	200	88±5	93.3	540±30	6.1	1.4±0.1	2.8±0.1
$2-1$	50	24±1	29.7	154±8	6.3	1.70±0.01	3.3±0.2
$3-1$	20	11±1	11.7	79±4	7.0	2.8±0.1	4.3±0.2
$3-1$	50	34±2	39.1	216±11	6.4	2.91±0.05	4.6±0.2
$3-1$	200	172±9	182.3	1070±50	6.2	2.8±0.1	5.6±0.2
$3-2$	50	17±1		104±5	6.0	1.2±0.1	2.2±0.1
$3-2$	200	66±4		380±20	5.8	1.3±0.1	2.0±0.1
$4-2$	50	18±1		111±5	6.1	1.1±0.1	2.4±0.1
$5-1$	20	16±1	15.4	124±6	7.8	4.8±0.1	6.8±0.3
$5-1$	50	55±3	58.1	38±20	6.9	4.22±0.08	8.1±0.4
$5-1$	200	277±14	295	1770±90	6.4	4.94±0.07	9.3±0.4
$5-2$	50	19±1		114±6	6.1	1.2±0.1	2.4±0.1
$5-2$	200	67±4		390±20	5.9	1.35±0.05	2.1±0.1
$13-2$	50	21±1		133±7	6.2	1.45±0.05	2.8±0.1
$100-2$	50	23±1		142±7	6.3	1.51±0.07	3.0±0.2

Table 4.1: Radius of gyration, end-to-end distance (in LJ units), persistence length (in monomers) and Kuhn segment length (in LJ units) for selected simulation systems. A $x-y$ system has a stiffening potential of strength xk_BT applied every y monomers. The errors are estimated in the range of 5% consistent with binning analyses [AT87] and the relaxation times of the chains. The second value for R_{gyr}^2 is the analytical expression of eq. (2.12) if one sets $l_{\mathrm{p}} = x$. This is only possible for $y = 1,\ x > 0$.

---

[a] These data coincide well with those of Pütz who investigated 1600 chains [Püt99]. Thus, 500 chains are enough for this system size.

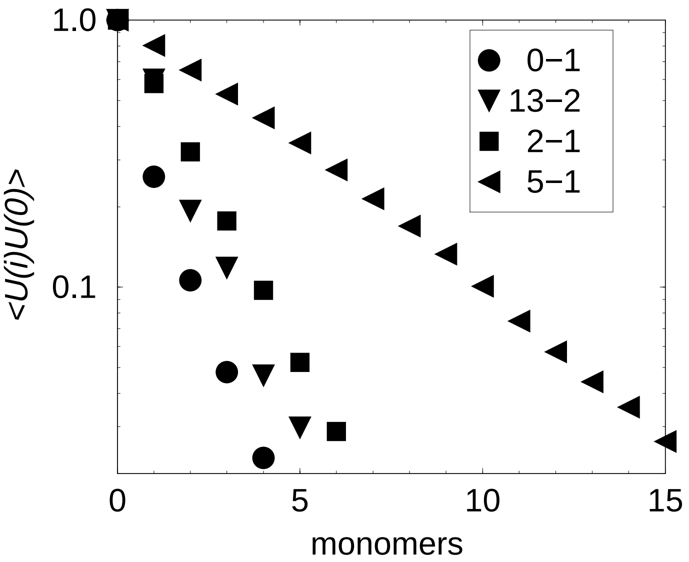

Figure 4.1: Bond correlation functions along the chain back-bone used in the calculation of persistence lengths for different systems of chain length $N = 50$.

This is perfectly true for all points with even monomer distances along the chain. This result may be generalized to a repetitive sequence of n different bond angle potentials

$$\frac{1}{l_\mathrm{p}} = \frac{1}{n}\sum_{j=1}^{n}\frac{1}{l_{\mathrm{p}j}} \; . \tag{4.3}$$

This description worked well for the $x - 2$ chains. The decay length of the bond-correlation depends on chain length due to end-effects. In the case of an infinitely long *wormlike* chain, there would be no ambiguity, and persistence length, Kuhn length and C_∞ would behave as expected.

Even in the systems of $x = 5$ and $N = 200$ no strong influences from periodic boundary conditions are expected. The size of the box was $49 \times 49 \times 49\sigma^3$. The end-to-end distance was on average $\sqrt{1769} \approx 42$ and the radius of gyration $R_\mathrm{gyr} \approx 16$. As the interaction cutoff was negligible with $r_\mathrm{cutoff} = \sqrt[6]{2}$, there was only weak direct interaction of the chains with their images.

4.2 Orientation correlations

In this section the local ordering of neighboring chains in bead-spring polymer melts is studied. For the chains, tangent unit vectors were calculated between nearest neighbor monomers or to describe larger blocks along the chains. The spatial orientation correlation function *OCF* measures local orientation. For comparison to NMR experiments [Sli90, SRS94] and to avoid the distinction between head and tail of the symmetric chains, the second Legendre polynomial was used

$$OCF(r) := \Big\langle P_2(\alpha) \Big\rangle_r = \left\langle \frac{1}{2}\Big(3\cos^2\alpha - 1\Big) \right\rangle_r \; . \tag{4.4}$$

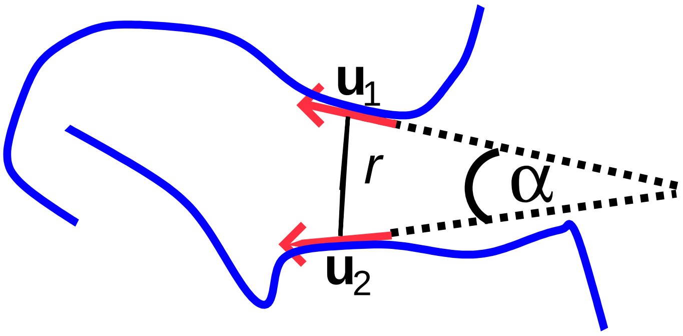

Figure 4.2: Definition of angle and distance for the orientation correlation function (eq. (4.4)) between different chains.

To this end, unit vectors between adjacent monomers were defined as

$$\vec{u} = \frac{\vec{r}_i - \vec{r}_{i-1}}{|\vec{r}_i - \vec{r}_{i-1}|} \ . \tag{4.5}$$

The scalar product between two such unit vectors describes the angle between chain tangent vectors (fig. 4.2)

$$\cos\alpha = \vec{u}_{\text{chain1}} \cdot \vec{u}_{\text{chain2}} \ . \tag{4.6}$$

The *OCF* was recorded as a function of r, the distance between the centers of mass of the respective chain segments. The unit vectors $\vec{u}_i$ are direction vectors along *different* chains unless explicitly stated otherwise. The *OCF* falls in the range $-0.5 \leq P_2 \leq 1$. A negative value means a preferentially perpendicular orientation of the respective vectors (-0.5 is perfectly perpendicular), a positive value indicates a parallel orientation (1 is perfectly parallel) as illustrated in figure 4.3. For uncorrelated vectors P_2 averages to zero.

The very first investigation of this kind was performed in the 1970s with only 200 atoms on one infinitely long chain, whereby the last monomer was connected to the first without closing to a ring [WH79]. Some time ago such orientation correlations were also observed in similar systems like the ones under study here but for short chains of $10-20$ monomers [RR88].

Figure 4.4a shows inter-chain orientation correlation functions of different systems. The first minimum ($r < 1$) is close to $P_2 = -0.5$ which would indicate a perfect perpendicular ordering. There are only few pairs approaching so closely. They have for geometric reasons to align perpendicular as the centers of mass of two dimers can come closest if they are perpendicular to each other. The first peak ($r \approx 1.2$) shows a preferred parallel alignment at the distance of the first neighbor shell. This order is not mediated by a perpendicular chain inbetween. The numbers of such pairs is much higher than the direct perpendicular contacts. A second parallel peak follows at $r \approx 2$. The intervening minima ($r \approx 1.6$) get weaker for higher stiffness indicating stronger local parallel ordering. The *OCF* decays to zero with r because the system is globally isotropic, not nematic.

For systems with small persistence lengths such as $2-1$, and $5-2$, the local order differs only slightly from the fully flexible case, whereas the chain with $x = l_\text{p} = 5$ shows a more pronounced local parallel orientation. For these chains there is residual parallel order even at the intermediate minimum ($r \approx 1.6$), where the other systems show some perpendicular ordering. These chains have except for the few direct contacts locally a preferred parallel neighborhood of three monomer diameter size.

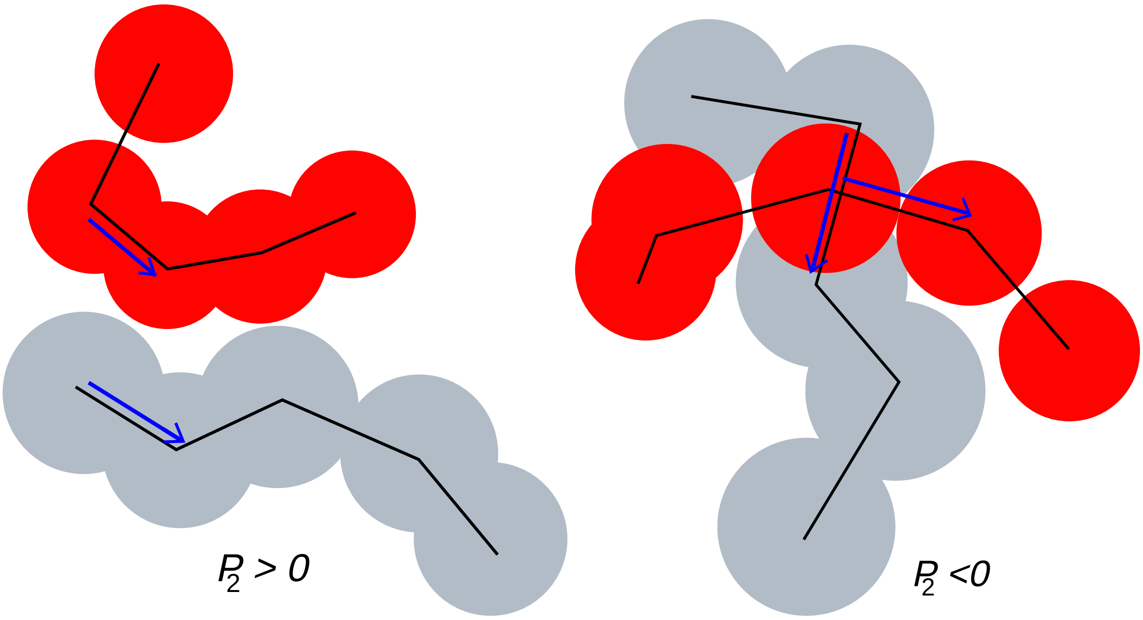

Figure 4.3: Illustration of the meaning of positive and negative values of the orientation correlation function (second Legendre polynomial). The values correspond to the dimers indicated by blue arrows.

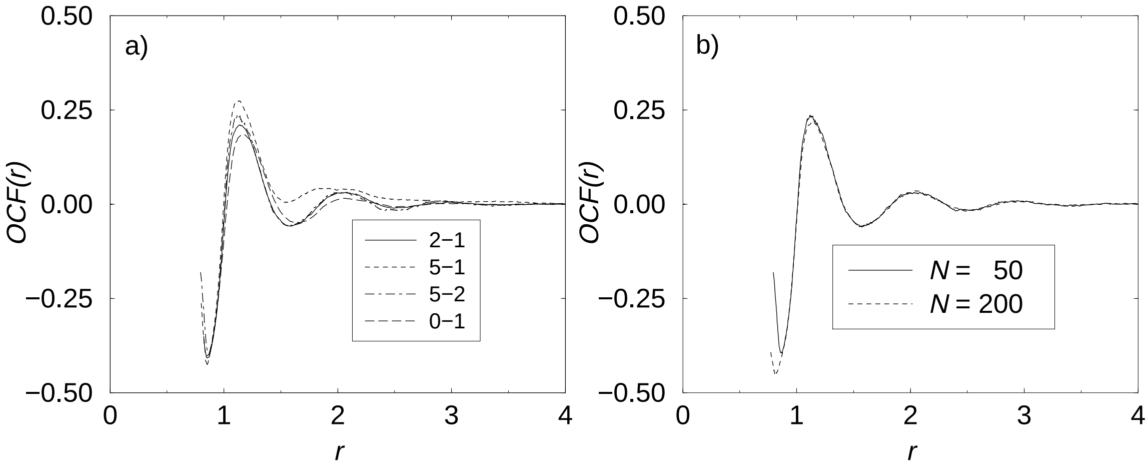

Figure 4.4: a) Inter-chain orientation correlation functions for chains with 50 monomers. b) Inter-chain orientation correlation function for different chain lengths for the 5 − 2 system. To better distinguish between the lines, a running average (over 15 points, $\delta x \approx 0.05$) was performed.

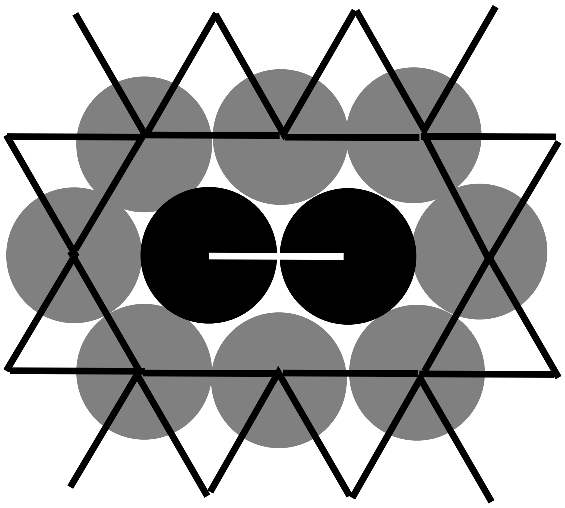

Figure 4.5: One plane of the face centered cubic lattice, only correlations between the white line and the black lines are taken into account for the *OCF* to model simplistically the connectivity.

Except for the very few direct contacts where chains are pressed into each other, there is, thus, parallel orientation between neighboring chains. This order is visible up to about three monomer diameters. The more flexible systems ($0-1, 2-1, 5-2$) show qualitatively a similar ordering, but it is less pronounced and there is intermediate preferred perpendicular orientation at a distance of about the first minimum in the radial distribution function ($r \approx 1.6$).

The *OCF*s for chains of different length are not distinguishable (fig. 4.4b) [FPMP99]. Thus, the effect is strictly local. This even holds although the global dynamics of the chains of varying lengths is different: the chains of length 25 are not yet entangled, whereas the longer chains are already influenced considerably by entanglements (entanglement length in the fully flexible case about 32 monomers [KG90, PKG00], and shorter with increasing l_p see section 5.3).

The only effects contributing to the local order in the case of full flexibility are connectivity and excluded volume. The latter can be modeled simplistically by a close packing of spheres. Therefore, a face-centered cubic lattice was created. In this model correlations of directions of dimers were looked for. The connectivity was modeled in a simplistic fashion; only dimers not sharing a common lattice site were taken into account (fig. 4.5). The result of these correlations is shown in figure 4.6 in comparison to the orientation correlations of fully flexible chains. The generic features are in good agreement. One can say that the local structure of fully flexible chains is well explained by simple packing arguments. For packing in turn the shape of the excluded volume is very important, as can be seen here for hard spheres. In section 6.6 this is the reason for the explicit local packing of atomistic models. One can imagine the parallel orientation at the first peak because of orientation correlations *along* the chains. On average a chain prefers at least slightly to keep its direction. Thus, the neighbors have to line up.

In addition, orientation correlation functions of longer chain segments were investigated. Here, not only vectors connecting nearest neighbors but vectors connecting next-to-nearest neighbor beads or beads farther apart were taken into account (fig. 4.7). The orientations of such segments is characterized by unit vectors defined as

$$\vec{u}_d := \frac{\vec{r}_i - \vec{r}_{i-d}}{|\vec{r}_i - \vec{r}_{i-d}|} \,, \tag{4.7}$$

where d is a measure of the segment size. Figure 4.8a shows that the effect of local parallel chain orientation is not restricted to segments of 2 monomers. It persists when larger chain fragments are

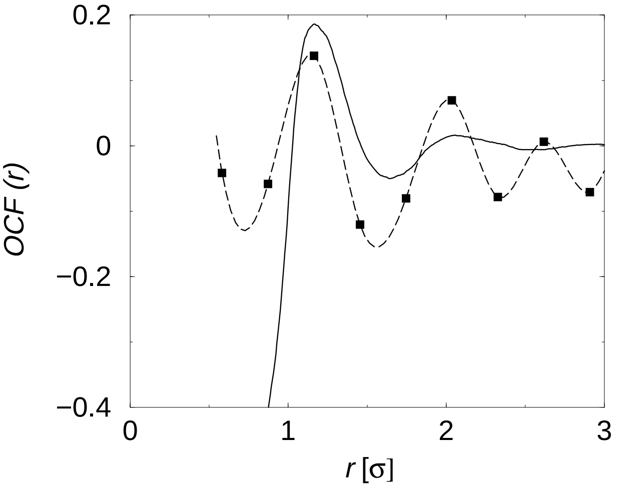

Figure 4.6: Comparison of orientation correlation on a lattice (squares) with the simulation results for the fully flexible system (solid line for 500 chains of length 50). The dashed line is a spline as a guide to the eye.

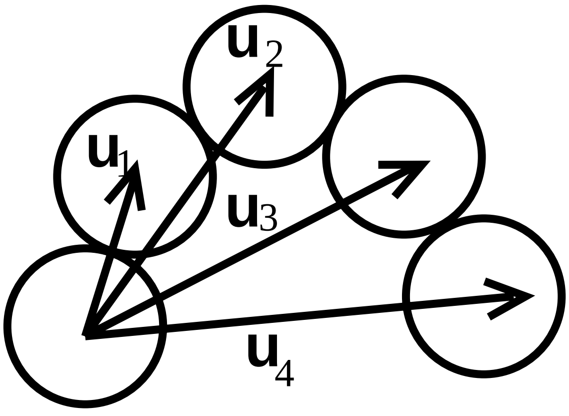

Figure 4.7: Definition of unit vectors of segments along the chain. Centers of mass are the midpoints of the arrows.

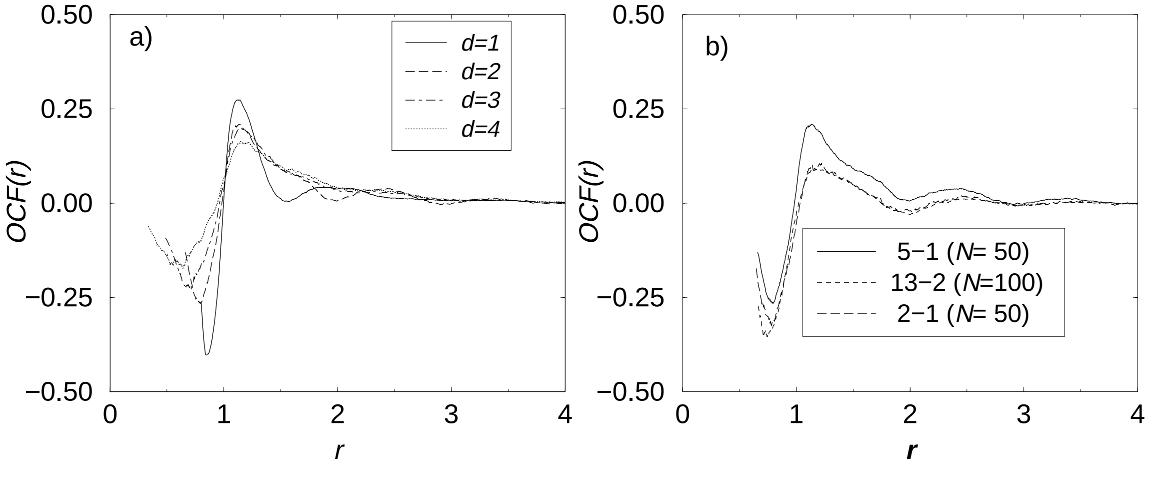

Figure 4.8: Spatial orientation correlation functions of segments of length d: a) Different segment lengths in a $5-1$ system with 50 monomers. b) Different systems, $d = 2$. A running average was applied in order to be able to see differences of the curves.

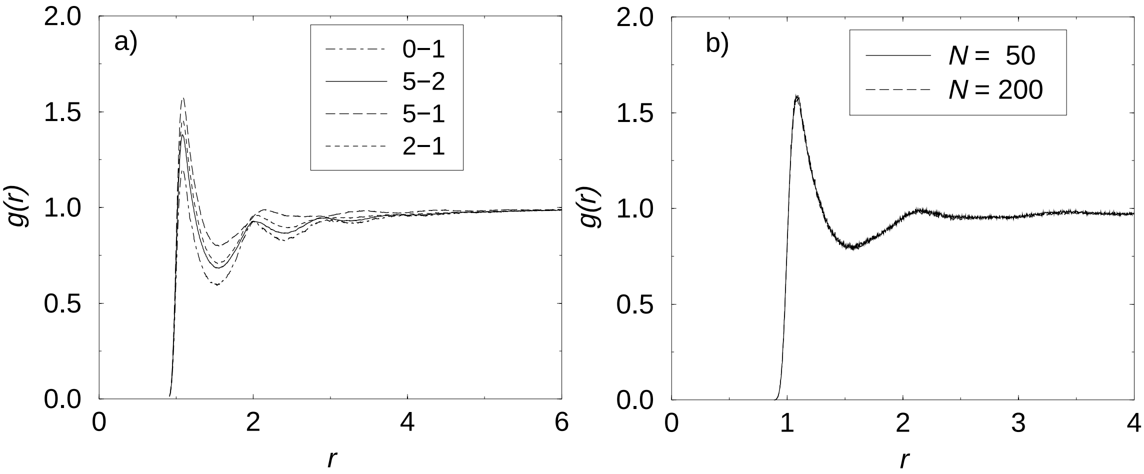

Figure 4.9: Inter-chain monomer-monomer radial distribution functions: a) Different stiffnesses for length 50. b) Different lengths for 5 − 1 system. To better distinguish between the curves, a running average was applied.

analyzed. But, the degree of order decreases with segment size. Figure 4.8b again shows the more pronounced local order in the case with persistence length $l_\mathrm{p} = 5$ compared to the more flexible chains. The 2 − 1 and the 13 − 2 systems coincide almost perfectly. Their persistence lengths are quite similar, and for the bigger segment sizes the exact local realization of this persistence length is no longer important, only its overall value.

These results are also in qualitative agreement with a lattice Monte Carlo investigation of short chains [KSY86]. Lattice models, however, are biased in favor of orientation correlation. Due to the lattice a long range correlation is induced leading to more pronounced and longer ranged correlations.

4.3 Melt and chain structure

The *inter* chain radial distribution function $g(r)$ (RDF) describing the monomer packing in the melt does not change much with added stiffness on large scales (fig. 4.9a). There are, however, some differences on very local scales. Both the second and third neighbor peaks are further apart for stronger stiffness. Furthermore, the minimum between the first and second neighbor shell is not as pronounced as in the more flexible cases, whereas the first maximum is higher. The local stretching allows a closer approach of chains. This leads to a reduction of the correlation hole which results from the fact that due to connectivity any monomer has a significant number of monomers from the same chain as neighbors, excluding monomers from other chains from its neighborhood. In fully flexible systems the number of neighbors from the same chain increases with chain length until saturation. No effect of chain length is to be seen for the stiffer systems (figure 4.9b) which again reflects the strict locality of the structure formation in the melt.

Static structure functions are experimentally accessible by neutron or X-ray scattering. The single chain structure factor S_SC reads (sec. 2.1.2):

$$S_\mathrm{SC}(k) = \frac{1}{N} \sum_{m=1}^{N_\mathrm{C}} \left\langle \left| \sum_{j=1}^{N} \exp(ikr_j^m) \right|^2 \right\rangle . \tag{4.8}$$

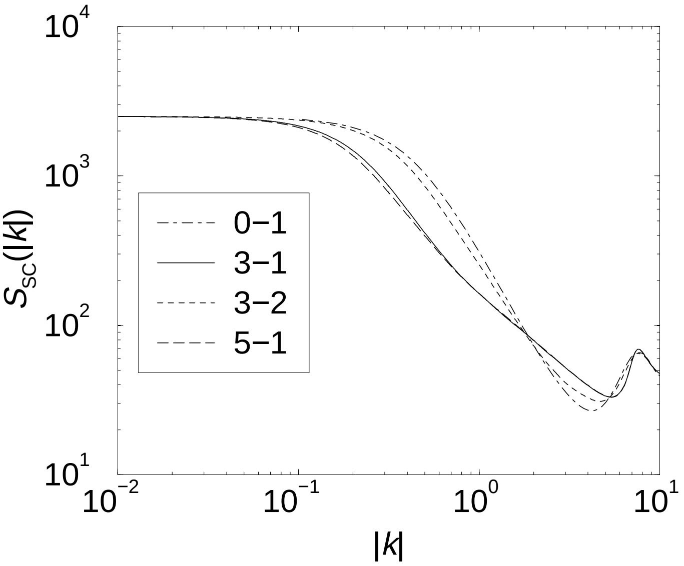

Figure 4.10: Single chain structure factor S_{SC} in the melt for different systems at chain length $N = 50$.

N_C is the number of chains, N the number of beads per chain and k the modulus of the scattering vector. The static single chain structure factor was calculated from the simulations (fig 4.10). First, one recognizes that the single chain structure factor of the fully flexible chains decays with k^{-2} as expected. This exponent indicates a Gaussian chain (sec. 2.1.2). Additionally, one sees that the stiffening leads to a deviation at large k-vectors, i.e. at short length scales. The fully stretched and the Gaussian chain are the two extremes which are interpolated between.

In the static case a renormalization of the chains onto coarse-grained Gaussian chains is possible by introducing the concept of a *Kuhn*-segment length l_K. As there is only one governing length scale, everything on larger lengths than l_K does not know about the local interactions. The melt consists of renormalized Gaussian chains, where the local packing leads to correlations of orientation on short scales without forming a liquid crystal on the large scale.

5 Dynamic effects of entanglements in melts of semiflexible chains

As the statics of semiflexible model polymers can be described in terms of established models, one can now perform the next step. This chapter focuses on the dynamics of the model described in section 3.3. First, the reorientation dynamics is under investigation in order to compare with NMR experiments. Then, the Rouse analysis of the system is performed, and mean-squared displacements as well as the diffusion behavior are examined in order to determine the crossover to reptation dynamics.

Table 5.1 gives an overview of the simulated systems with their Rouse times and simulation lengths. The Rouse modes are no longer the true eigenmodes of the system if local stiffness comes into play (secs. 2.2 and 5.2). However, Rouse times are still useful as an estimate of the relaxation time.

x	N	N_{C}	$t_{\mathrm{sim}}[\tau]$	τ_{R}	$6DN$
–	2	1000	2500	-	0.45
1.5	5	1000	30000	(40)	0.44
3.0	5	1000	30000	(60)	0.42
5.0	5	1000	30000	(88)	0.38
0.0	10	500	30000	100±10	0.43
1.5	10	500	30000	190±10	0.44
1.5	10	2000	20000	170±10	0.41
3.0	10	500	30000	300±30	0.36
5.0	10	500	33000	(630)	0.27
1.5	13	500	25000	290±10	0.35
3.0	13	500	25000	600±50	0.27
1.5	15	500	37000	400±20	0.36
3.0	15	500	36000	850±30	0.28
1.5	17	500	66000	540±40	0.34
3.0	17	500	30000	1080±20	0.27
5.0	17	500	30000	(2600)	0.22
1.5	20	500	30000	800±30	0.28
1.5	20	2000	30000	820±30	0.31
3.0	20	500	42000	1800±100	0.22
5.0	20	500	28000	3700±200	0.19
0.0	25	500	30000	730±20	0.39
1.5	25	500	25000	1380±50	0.29

x	N	N_{C}	$t_{\mathrm{sim}}[\tau]$	τ_{R}	$6DN$
3.0	25	500	63000	3150±50	0.20
5.0	25	500	78000	6900±150	0.18
1.5	30	500	37000	2200±50	0.27
3.0	30	500	54000	5000±300	0.18
5.0	35	500	109000	18000±2000	0.14
0.0	50	500	20000	3300±200	0.30
1.5	50	500	73000	7000±200	0.18
3.0	50	500	70000	20000±1000	0.10
5.0	50	500	113000	42000±2000	0.10
1.5	75	500	148000	23000±2000	0.14
1.5	200	500	300000	≈100000	
3.0	200	500	350000	≈200000	
5.0	200	500	750000	*	
0.0[1]	350	120	1700000	≈500000	
5.0	1000	250	60000	*	

Table 5.1: Simulated systems with $y = 1$: x: strength of the stiffening potential, for static observables see table 4.1; N: number of monomers per chain; N_{C}: number of chains, t_{sim}: simulation times; τ_{R}: Rouse times, numbers in brackets for systems if chains are too short for reliable Rouse mode analysis; D: center of mass diffusion constant (for the systems in which free diffusion was reached) with error of at most 5%. The Rouse times are determined by averaging over the first few modes (compare table 5.4) for $N \leq 75$. For longer chains the crossover from the $t^{1/4}$ to the $t^{1/2}$ regime in g_1 is taken. The Rouse time is only an estimate of the relaxation time. *:The Rouse times for these systems could not be determined by either method.

The short chains allow an estimate of the intrinsic diffusion coefficient of chains of a given stiffness, i.e. their mobility without constraints from the surrounding. They could be followed into free diffusion allowing for the determination of influences of stiffness on chain mobility. The slowdown does not follow a linear relationship with chain stiffness, as would be expected from the Rouse model. The chains of length 10 and below can be no more described as random walks, especially if an intrinsic stiffening potential is applied, as the relation $l_{\mathrm{p}} \ll L = (N-1)l_{\mathrm{b}}$ is no longer fulfilled. But, remarkably, a Rouse scaling is applicable at $N = 10$ up to $l_{\mathrm{p}} = 3$ (see section 5.2).

5.1 Reorientation of semiflexible model Polymers

Double-quantum NMR experiments on different polymers allow the investigation of local reorientation dynamics, i.e. the reorientation of C−H bonds [Gra98, GHS98, CS98]. The relevant time and length scales discussed in this section, therefore, lie in the range of the NMR experiments. For polybutadiene (PB), which is the polymer to which the simulation data will be compared, the reptation time (crossover from $t^{1/2}$ to $t^{1/4}$ in the mean-squared displacement) is $\tau_e = 0.15$ ms and the

---

[1] This simulation was taken from M. Pütz and reanalyzed [Püt99].

Rouse time is $\tau_R = 300$ ms at T = 223 K and a molecular weight of 128000 g/mol with a double quantum preparation time in the range of $0.25 - 1.5$ ms [Gra98]. This is the time during which the monitored bond vector can reorient; its direction is then correlated to the initial direction. The experiments actually rely on the time-temperature superposition principle. The relevant data from the butadiene measurements are in the dynamic regime, in which a one-dimensional Rouse-like relaxation of the chain is expected for fully flexible chains. The observations in the reorientation of polybutadiene are not explained by the simple reptation picture [GHS98] in contrast to experiments on the more flexible PDMS [CS98], as a high degree of local order is claimed. The stiffness of polybutadiene is characterized by $C_\infty = 5.8$ for *trans*-PB and 4.7 for the *cis* conformer.

5.1.1 Reorientation correlation function

The reorientation correlation function

$$C_{\mathrm{reor}} = \left\langle \frac{1}{2}\left[3\left(\vec{u}(t)\vec{u}(0)\right)^2 - 1\right]\right\rangle \tag{5.1}$$

described in section 2.5 was recorded in the simulations. The short-time and long-time behaviors differ fundamentally and are, therefore, discussed separately [FMPH00].

Short-time behavior

Reorientation of next-neighbor connecting vectors is a measure of very local scale chain dynamics. This reorientation correlation function decays algebraically on short time scales, as can be seen in figure 5.1. Even this very local property depends on chain length. Reorientation correlation functions decay much slower if the chains become longer. This is seen most evidently by the fact that longer chains have a much longer time-span of algebraic decay. Short chain correlation functions bend over to a second exponential process (see below) quite soon, especially for short persistence length. Moreover, the overall melt viscosity for $k \rightarrow 0$ should scale with N if the Rouse model was applicable. This leads to an overall slowdown with chain length. Additionally, the viscosity is dependent on the "bead friction", which depends on chain stiffness, as the Rouse relaxation times of short chains increase with persistence lengths (tab. 5.1). Thus, comparisons require a renormalization of time scales. In figure 5.1 time is rescaled by the chain length.

For shorter or more flexible chains the local process is more "effective" in the sense that it decreases the autocorrelation function to lower values in the initial algebraic process. Longer chains have more residual memory of the initial orientation when the second exponential process sets in. The local segments, therefore, are dynamically not independent. If one scales the simulation time by chain length ($t \rightarrow {}^{t}\!/_{N}$) the initial decays coincide almost (fig. 5.1d).

The short-time part of the correlation function depends more on stiffness and the long-time correlation more on chain length (below). So one can conclude that *intra*-chain interactions related to the intrinsic stiffness contribute significantly to the first process. On the local scale the persistence length prevents the chain from bending and, thus, local vectors from reorienting. On longer time scales the reorientation is hindered substantially by topological constraints of the neighboring chains; the *inter*-chain effects come into play as the chains get more extended.

An alternative view of the separation of time scales can be taken from the involved energy scales. The *intra* and *inter* interactions have different frequencies (or energies) involved. Bond angle bending is a high frequency process. It appears on short time scales with a high energy

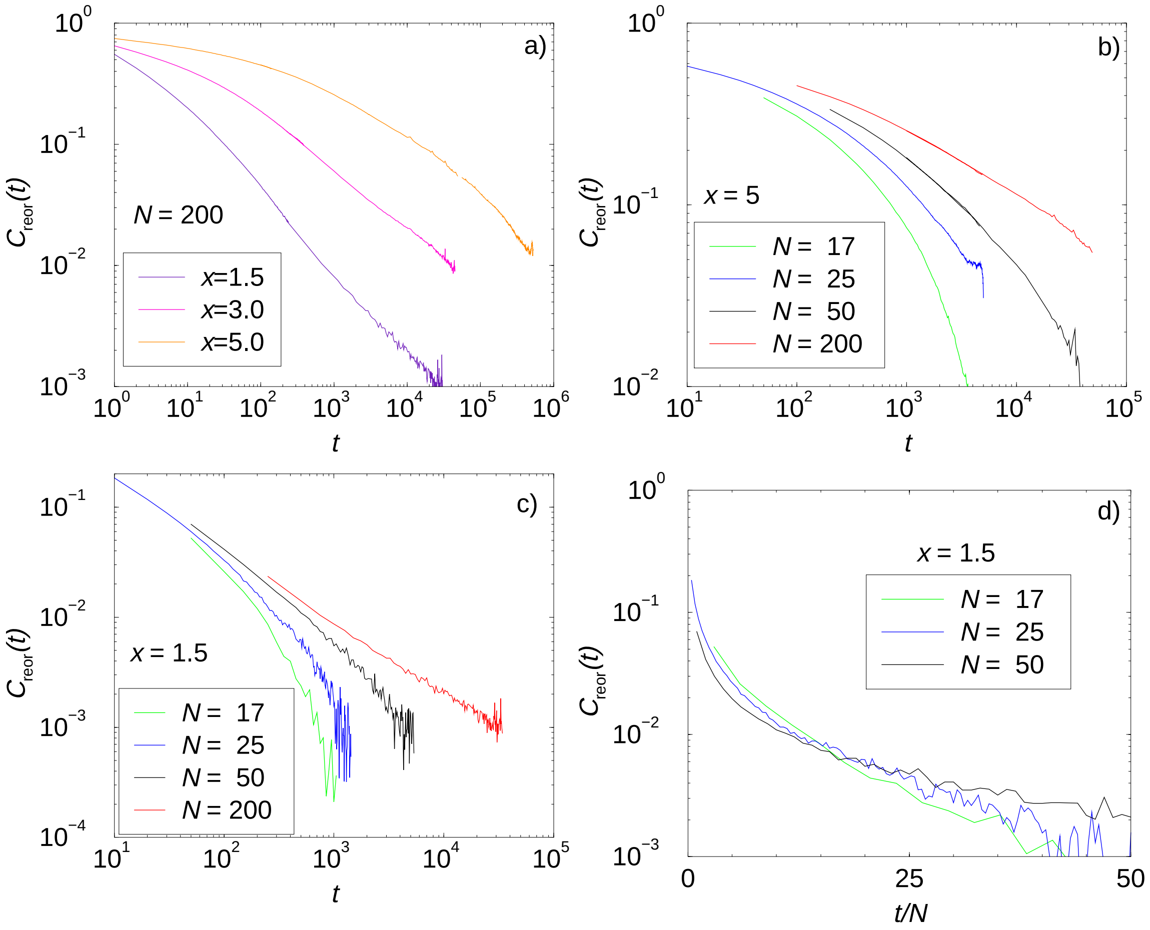

Figure 5.1: Short time behavior of the time dependent second Legendre polynomial of all next neighbor vectors for different systems. a) $N = 200$, different persistence lengths, b) $x = 5.0$, different chain lengths, c) $x = 1.5$, different chain lengths. d) $x = 1.5$ for very short times rescaled by $1/N$.

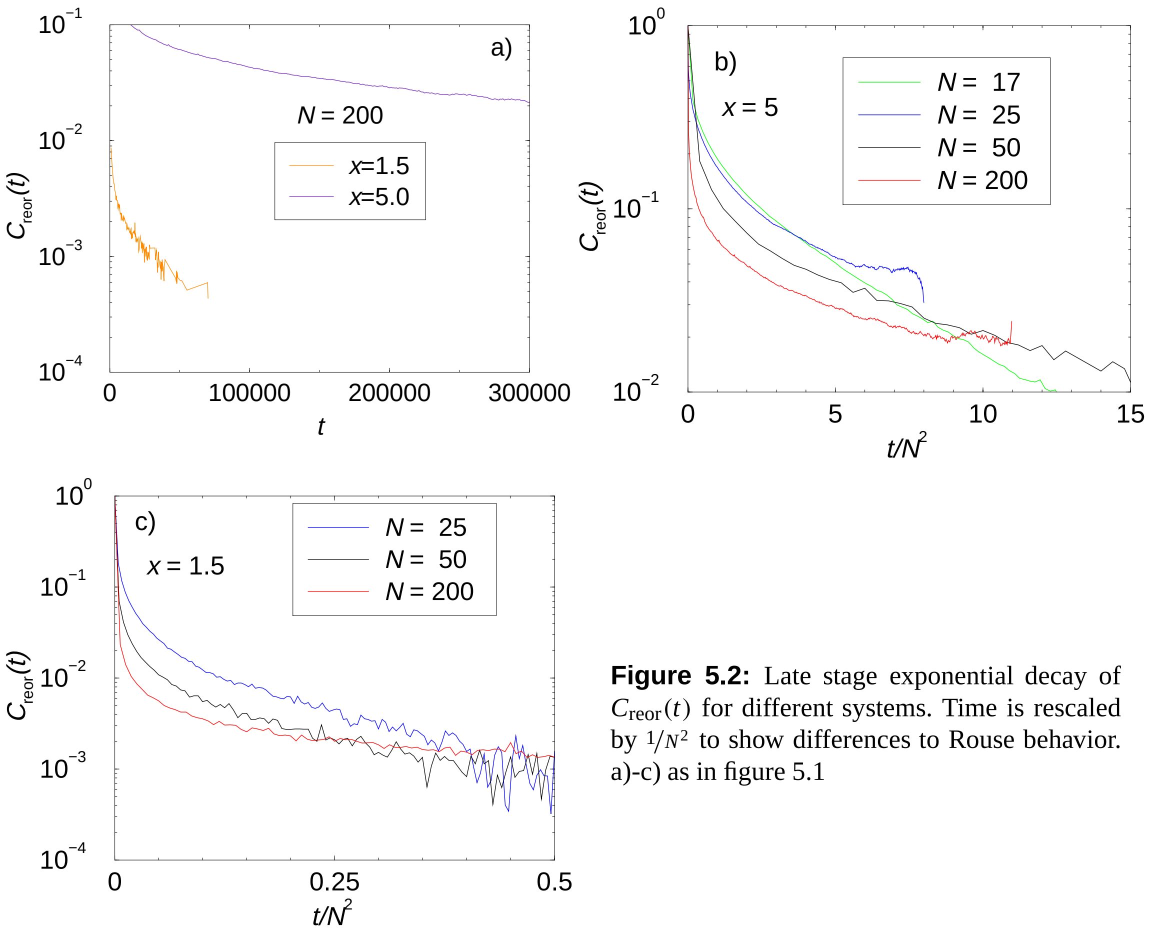

Figure 5.2: Late stage exponential decay of $C_{\text{reor}}(t)$ for different systems. Time is rescaled by $1/N^2$ to show differences to Rouse behavior. a)-c) as in figure 5.1

penalty. On the other hand, relaxation of entanglements leads to energetically very similar conformations; thus, it is a low frequency process. This explains the separation of the time scales of the two processes from a more abstract point of view.

Long-time behavior

The long-time tail of the reorientation correlation function decays exponentially as can be seen in figure 5.2. This process and its decay time change considerably with chain length (fig. 5.3). The dependence is more evident than in the short-time regime. This is expected because, according to the Rouse model, the overall chain relaxation should scale with N^2. Time is rescaled in figures 5.2b and c to stress the observed deviations from Rouse behavior. Approaching the entanglement regime, an increase with the the chain length to the power of 3.4 is expected. The reorientation time constant τ_{reor} (obtained by exponential fitting of the second part of the auto-correlation function) is much shorter than the time for overall chain reorientation of the long chains, but still longer than all local time scales involved in the short time process. Therefore, in the case of long entangled chains, it is for the local processes no longer important whether the overall chain reorients completely. There is an intermediate length scale, the entanglement length, governing the local scale dynamics.

In the limit of infinitely long chains the local segmental dynamics has to become independent

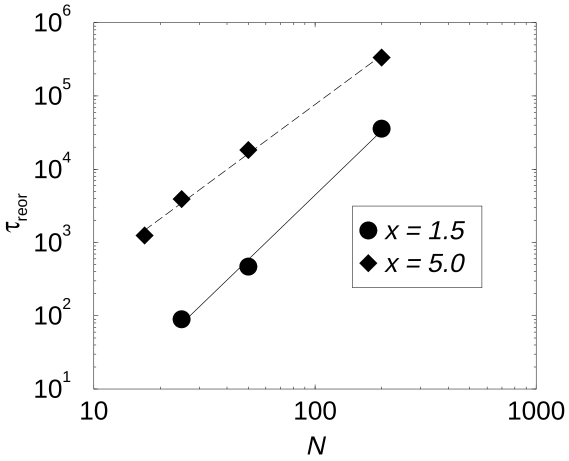

Figure 5.3: Reorientation times τ_{reor} of local segments as a function of chain length and stiffness calculated from exponential fits to the long-time tail of the reorientation correlation function. The dashed line indicates an increase with $N^{2.3}$ for $x = 5$ and the solid line $N^{2.9}$ for $x = 1.5$.

of chain length because it is impossible to propagate chain orientations over infinitely long distances in the finite local reorientation time. In this limit, the local segment does not "know" the length of the chain, to which it is attached. Thus, the relaxation of a large but finite segment of the chain of the order of a few entanglement lengths has to give the local parts enough freedom to relax totally. Otherwise, the local parts could not relax completely. This would be the case if the ends of the relevant segment were constrained for all times. Then, even the smallest segment would get "stuck" at some final plateau value. Just take the case of an entangled melt of fully flexible chains ($N = 350$, $x = 0$) as an example whereby the initial algebraic decay of C_{reor} is very fast. This occurs on time scales of the entanglement time, which is about 1800τ in this system [DGK98]. Additionally, this process is very effective. The remaining $C_{\mathrm{reor}}(\tau_{\mathrm{e}})$ for the long-time orientation is less than 0.01. The decay time of the long-time process is about 5000, which is the relaxation time of chain-segments of the length of about 60 monomers. This corresponds to about twice the entanglement length of the system [KG90], so that it is sufficient that subchains of the order of slightly more than the entanglement length relax to give local vectors the freedom to reorient fully.

Reorientation of medium-size chain segments

The reorientation of longer chain segments, i.e. unit vectors between monomers farther apart along the chain, is shown in figure 5.4 for the system with chain length 200 and stiffness parameter, i.e. persistence length, 5 as an example. The unit vectors are here defined as

$$\vec{u}_d = \frac{\vec{r}_{i+d} - \vec{r}_i}{|\vec{r}_{i+d} - \vec{r}_i|} \ . \tag{5.2}$$

Thus $d = 1$ represent the next-neighbor connecting vectors discussed so far.

If there is a distance of d monomers along a chain of length N the amplitudes of the reorientation correlation function in the exponential regime are expected to behave according to $3d/5N$, if simple arguments for entanglements are used [GHS98]. To obtain this relation, one uses the number of the Kuhn segments between two entanglements. Thus, the static picture is transferred into the dynamics.

All local length scales ($d \leq 11$) decay in the second process with almost the same single exponential function defining a reorientation time τ_{reor} (tab. 5.2). However, the proportionality of the amplitude with $1/N$ is not observed questioning the topological arguments (fig. 5.3). In subsec-

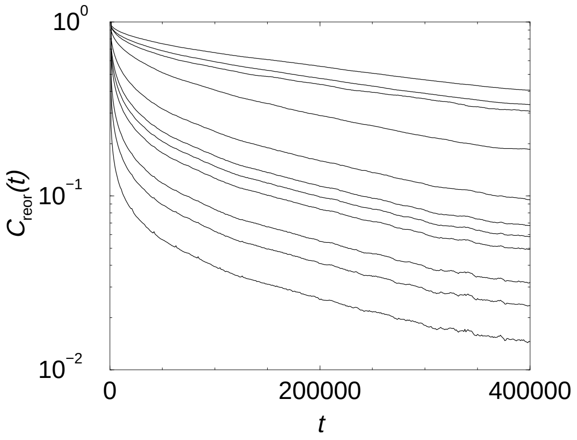

Figure 5.4: Reorientation of chain segments of different length d for the system with length $N = 200$ and potential strength (persistence length) $x = 5$, $d = 1, 3, 5, 9, 11, 13, 19, 39, 79, 119$, and 199 (end-end vector) from bottom to top

d	β	$\frac{\tau}{1000}$
1	0.055	269
3	0.087	272
5	0.115	276
9	0.172	283
11	0.202	286
39	0.533	335
199	0.796	558

Table 5.2: Exponential decays fitted to the curves in figure 5.4 ($N = 200$, $x = 5$) in the time domain between $t = 100000$ and 300000. The amplitude β is defined by the following relation $C_{\mathrm{reor}}(t) \rightarrow \beta e^{-t/\tau}$, $t \rightarrow \infty$, i.e. the value extrapolated back to $t = 0$ for the function valid in the long-time limit to compare amplitudes.

tion 2.4.1 it was discussed that arguments of this kind cannot describe the interplay between stiffness and entanglements sufficiently. Especially in the systems with chains of length 200 and 1000 one sees that the respective time constant for the second process can no longer be related to the reorientation of the full chain (see above). The latter is at least for $N = 1000$ expected to occur on time scales well beyond the reach of the simulations ($\approx 10^7$). The reorientation happens on shorter but still macroscopic or at least mesoscopic orders of magnitude $\tau_{\mathrm{reor}} \approx 300000$ (fig. 5.3). This finding suggests also that the entanglement length is a relevant length scale. For local phenomena every length longer than l_{e} is “infinite”. Therefore, local processes experience their surrounding at most up to the entanglement spacing. Additionally, this is a hint that the entanglement length decreases with persistence length as the separation of time scales is more pronounced.

The proportionality of the correlation function at a given time in the long time tail with the segment length d could not be confirmed either (see parameter β in table 5.2). There is obviously a dependence of the residual order on the segment size. But it does not simply scale linearly, as suggested by analysis of the simplified model. The length scales correlate in some complex manner which shows the interplay of relevant length and time scales.

5.1.2 Comparison to double-quantum NMR experiments

For the interpretation of double-quantum experiments like the ones by Graf *et. al.* for polybutadiene [GHS98], the correlation function $C_{\mathrm{DQ}}(t) = \langle P_2(\vec{u}(t)\vec{B})P_2(\vec{u}(0)\vec{B})\rangle$ is the correct choice (sec. 2.5). As shown in appendix A, this function is for isotropic melts proportional to C_{reor}.

There is a difference between C_{DQ} for simple bead-spring chains and the experimental C_{DQ}

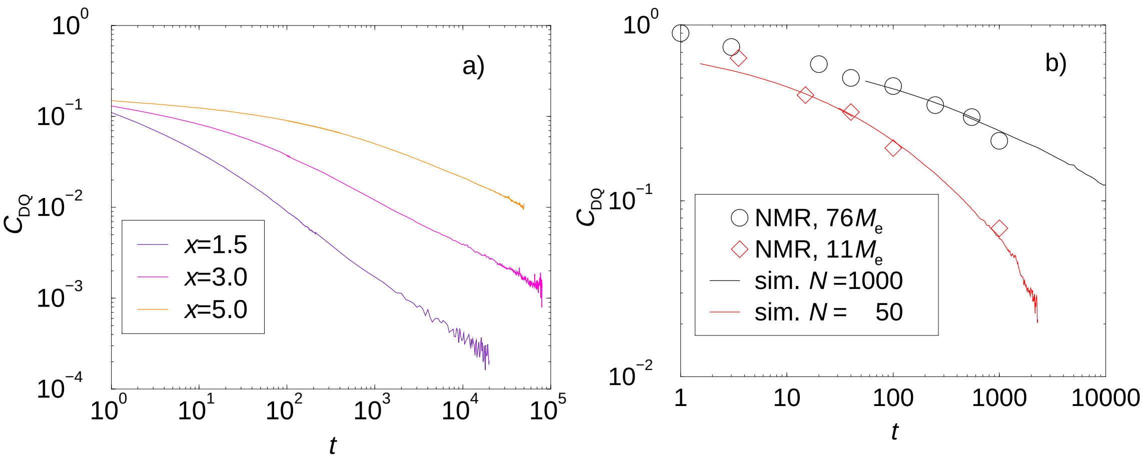

Figure 5.5: a) Double-quantum correlation functions for systems with different persistence lengths at chain length $N = 200$. This function directly relates to experimental observables.
b) Comparison of double-quantum correlation functions from the simulations with the experiments on polybutadiene of ref. [GHS98], whereby the dynamical order parameter $S = \sqrt{C(0)}$ and the trivial factor of $^1/_5$ have been left out. The simulations are scaled to $C(0) = 1$. The time axis for the simulation data is scaled empirically, as the direct model-free mapping to experimental times is not possible. The experimental times are measured in entanglement times, which are derived from viscosity measurements.

which has contributions from many more (*intra*-monomer) degrees of freedom. This manifests itself mainly in a different behavior at $t \to 0$. In the experiments the limit of $C_{\mathrm{DQ}}(0)$ for $t \to 0$ is called a *dynamical order parameter* $\mathcal{S}$, after removing the trivial factor of $^1/_5$ (appendix A). This is partly related to internal degrees of freedom, which are not present in the simple bead-spring model, so that the absolute values are not comparable. Experimentally, for the reorientation of the carbon-carbon double bond in polybutadiene, $\mathcal{S}_{\mathrm{C=C}} = 0.24$ is inferred. $C_{\mathrm{DQ}}(t)$ is shown in figure 5.5a for systems with different persistence lengths at $N = 200$, whereby entanglement effects play a role.

As discussed in section 2.5, in the time interval between the entanglement time τ_{e} and the Rouse time τ_{R}, for which the inner degrees of freedom of the chain are relaxed, a $t^{-1/4}$ regime of $C_{\mathrm{DQ}}(t)$ is expected. Later, in the regime, where the chain simply reptates as a whole in its tube, a $t^{-1/2}$ behavior should be found. The algebraic decay comes relatively close to the $t^{-1/2}$ dependence (tab. 5.3). The simulations can explain the qualitative features of the relaxation found in NMR measurements, if one focuses on the interplay between entanglements and stiffness. The local stiffness leads to more persistence on local scales, therefore shifting the decay to longer times. A $t^{-1/4}$ dependence of the correlation was found experimentally by Graf *et al.* for a system with very long and, therefore, highly entangled PB chains (with a molecular weight of 76 times the entanglement molecular weight M_{e}). They also observed a $t^{-1/2}$ power-law for a system with a molecular weight of $11M_{\mathrm{e}}$. Figure 5.5b compares simulation and experiment directly. The chain lengths (measured in N_{e}) of experiment and simulation are not the same, however, only the regimes slightly and far above the entanglement length are important. The curves have been superimposed by empirically scaling the time axis by 0.153 and 0.5 for $N = 50$ and $N = 1000$ respectively. This may be used to infer a direct model-free mapping to experimental times. The experiments, however, rely on the time-temperature superposition principle, as the time window in NMR is fixed. Thus, the detailed mapping includes a specific temperature. At T = 223 K, the

x	α
1.5	0.68
3.0	0.50
5.0	0.40
5.0*	0.29

Table 5.3: Algebraic fits ($t^{-\alpha}$) of decay of double-quantum correlation functions C_{DQ} for $N = 200$ (see text and figure 5.5).
* The bottom line for $x = 5.0$ has chain length $N = 1000$ but the system is not equilibrated.

experimental times are $\tau_{\mathrm{e}} = 0.15$ ms and $\tau_{\mathrm{R}} = 300$ ms for polybutadiene of a molecular weight of 128000 g/mol [Gra98]. The simulations presented here are well in the millisecond range for such low temperatures.

As the experimental times in fig. 5.5 are measured in entanglement times the mapping of simulation to experiment leads to an entanglement time $\tau_{\mathrm{e}}' < 10$ which is remarkably smaller than the $\tau_{\mathrm{e}} \approx 1500$ estimated from the mean-square displacements (section 5.3). This indicates that the standard reptation picture has at least to be modified.

Algebraic fits of the decay curves in the linear region of the double logarithmic plot yield the exponents shown in table 5.3. The systems under study are not very long, as they are at most about 30 times the entanglement length (except for $N = 1000$, $x = 5$). The exponents α are, therefore, closer to $1/2$ than to $1/4$. The system with persistence length 5 is the most entangled. It is found to reorient slowest with an exponent α between 0.25 and 0.5. The system with persistence length $l_{\mathrm{p}} = 1.4\,(x = 1.5)$, shows an algebraic decay faster than $t^{-1/2}$. This is probably because it is only weakly entangled, so that the effects of entanglements just start to play a role leading to the algebraic decay. The exponents decrease systematically with persistence length which, as discussed earlier, indicates an increasing degree of entanglement. The dependence on the degree of entanglement is supported by the finding of a very low exponent $\alpha = 0.29$ for a system with $l_{\mathrm{p}} = 5$ and chain length $N = 1000$. This, however, was a short run and due to computational limitations it could not be explored in greater detail, so the question whether a crossover to a $t^{-1/2}$ behavior as predicted by Ball *et al.* [BCS97] occurs could not be answered. The correlation functions of the chains of length 200, however, indicate a crossover.

5.1.3 Interdependence of reorientation and translation of segments

In the reptation picture the reorientation process should depend on the motion of the polymer in its tube. A useful quantity to investigate is therefore the orientation correlation function versus the mean-squared displacement of the corresponding monomers irrespective of time. This is averaged over a finite time $2t_{av}$ which does not necessarily start at $t = 0$. If the tube itself relaxes during some time t_m the correlation function disappears with time. Figure 5.6 shows the second Legendre polynomial of bond vectors against the mean-squared displacements of its constituent monomers.

$$C_{\mathrm{reor}}(\Delta r^2) = \left\langle P_2\left[\vec{u}(0)\vec{u}(\Delta t)\right]\right\rangle_{t_m - t_{av}, t_m + t_{av}}, \tag{5.3}$$

$$\Delta r^2 = \left[\vec{r}(\Delta t) - \vec{r}(0)\right]^2, \tag{5.4}$$

i.e. both C_{reor} and Δr^2 depend parametrically on Δt. In the curves for $t_m = 15000$ and $t_m = 75000$ a plateau is found (fig. 5.6) which indicates an almost non-reorienting regime at a certain spatial distance for chains long enough (entangled) and stiff enough ($l_{\mathrm{p}} = 5$). The presence of the plateau can be explained as follows: a polymer chain of finite length has a preferred orientation; i.e. at

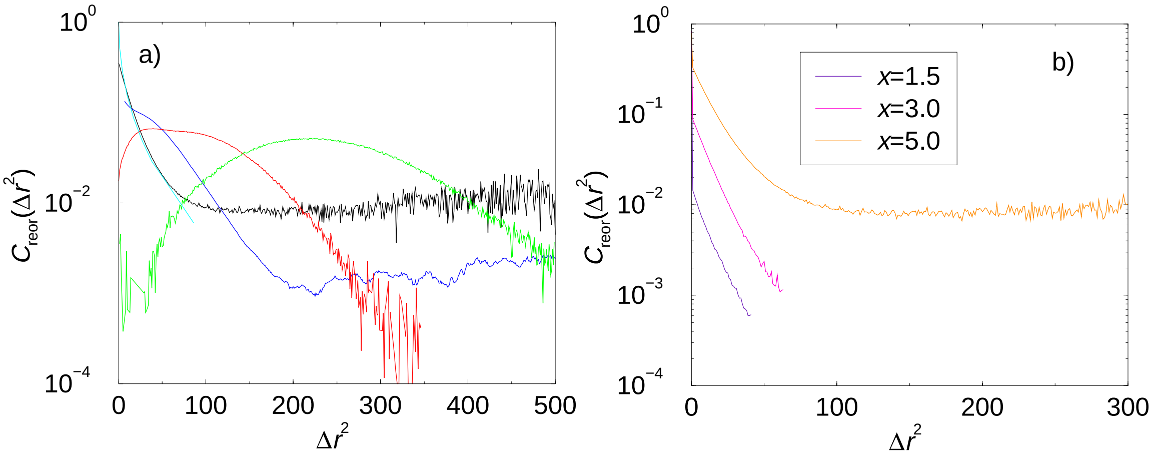

Figure 5.6: Reorientation correlation function depending on the mean-squared displacement of monomers ($N = 200$).
a) $x = 5$ three different time intervals t_m and comparison to static correlation. For reasons of statistics averages over $2t_{av} = 30000$ are shown, i.e. $t_m = 15000$ means $0 \leq t_m \leq 30000$. The static case is measured against topological distance, because distance in real space is not appropriate as the chain can fold back which leads for packing reasons (section 4.2) to perpendicular alignments. The different colors correspond to the following t_m black: 15000, blue: 75000, red: 135000, green: 25500, and the light blue curve is the static correlation. The maximum of the green curve corresponds to an average angle of 52.7°, which is rather close to the *magic* angle of 54.7° where the second Legendre polynomial vanishes.
b) Different systems at $0 \leq t_m \leq 30000$.
A running average was applied after the initial decay in order to show the possible plateau more clearly for the curve of $t_m = 75000$ in figure a) and the curve for $x = 5$ in figure b).

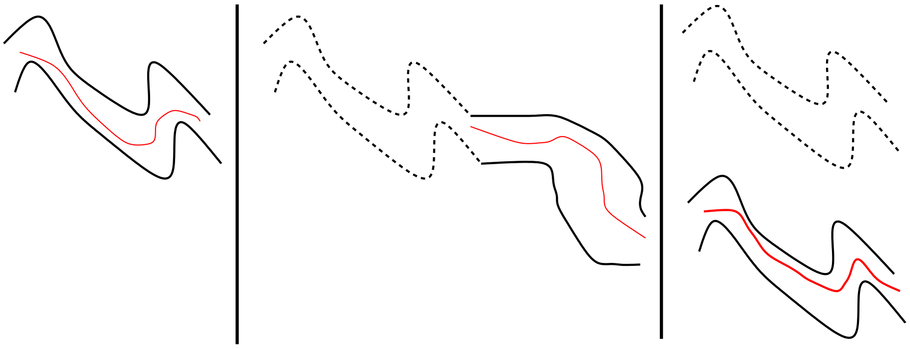

Figure 5.7: Illustration of the idea of reptation under shifting the tube without loosing orientation. This can lead to the observed behavior in the reorientation with diffusion.
This scheme is, of course, exaggerated in order to show the idea. The correlations are far from 100%. Chain visualization, however, show the transverse shift without full loss of orientation (fig. 5.14).

every instant of time there will be an excess component of the tangent orientation in the direction of the end-to-end vector that leads to a residual orientation correlation of segments a distance r apart. If the overall chain direction is preserved during the averaging time – or, more stringently, if the tube does not disappear on this time-scale – the residual correlation will also appear in $C_{\text{reor}}(\Delta r^2)$. The plateau is not a consequence of diffusion of the center of mass of the system as a whole. It has been made sure that this possible artifact of Brownian dynamics simulation has been accounted for in the analysis. For longer times the residual orientation propagates in space. There is no definitive answer, yet, as to what causes this behavior. However, a scenario that would fit the observation is that, in addition to reptation, there is a diffusive (or more probably sub-diffusive) motion of a part of the chain as a whole through space. If an array of vectors moves rigidly through space orientation is preserved fully but transported through space. By reorientation of the vectors as shown above, this correlation decreases. Still, there is a clear peak related to translational motion which moves with t_m and transports the orientation. This would mean a motion of the tube without changing orientation. Support for this idea is found by visualizations of the chain in the tube (fig. 5.14 in sec. 5.4 or title picture). Figure 5.7 illustrates the idea of a reptating chain in a shifted tube.

For comparison, also the static correlation function along the chain is plotted in figure 5.6. For very short times the dynamical correlation is almost the same as the static, for longer distances it is even slightly larger which results from contributions from $t \neq 0$. The more flexible chains have a plateau at a lower value. This is difficult to see due to the low statistical accuracy (fig. 5.6b). The actual plateau value decreases with t_m (fig. 5.6a), but it is still visible at $t_m \approx 75000$. The time dependence of the plateau value gives information about the stability of the initial neighborhood. It measures the “similarity”, i.e. the correlation of the neighborhood with the neighborhood at an earlier point in time as experienced by the chain coming back. The neighborhood, of course, changes with time which, however, happens on a much longer time scale.

These results support the presence of reptation in the systems under study, as the chains come back to their former surrounding which has undergone only small changes in the meantime. As this memory effect preserves information about orientations, a tube picture is still a suitable concept although the tube itself cannot be considered immobile. The chains do not behave simply as the standard reptation picture suggests. The reptation is considerably modified by their stiffness.

Stiffer chains reptate in a more pronounced way, i.e. they follow closer the primitive path of the tube. This leads to a higher degree of orientation memory for chains of the same length (fig. 5.6b).

5.1.4 Implications

The reorientation of polymer chains in dense melts is subject to two subsequent processes. The first leads to an algebraic decay of the reorientation correlation function and the second to an exponential decay. Both processes depend on chain length as well as on stiffness. Chain stiffness leads to a substantial slowdown of the reorientation on both time scales. The double-quantum correlation function shows an algebraic decay with a stiffness-dependent exponent. The dynamic reorientation exponents which are encountered in NMR experiments of systems not too far above the entanglement molecular weight could be reproduced. Therefore, even this simplistic model which is probably the simplest possible one incorporating stiffness and excluded volume, is successful in describing qualitatively the dynamics to a satisfying degree of accuracy. As the results are validated against experimental data, the reorientation correlation functions $C_{\mathrm{reor}}(t)$ can be regarded as meaningful.

To find an appreciable dynamic order parameter, local stiffness is required. Otherwise, the initial orientation memory is lost almost immediately in the short-time regime. Additionally, entanglements are needed in order to have an exponential second decay slow enough to observe the dynamic order on experimentally relevant time scales (milliseconds for the NMR experiments discussed). This means that, in principle, both processes are always present. To be observable, though, they have to govern a range big enough in amplitude and time.

The reorientation correlation functions are found to be in qualitative agreement with experiments [GHS98] and theoretical predictions [BCS97]. Still, this does not imply an increased static order by entangling the polymer chains. The static order increases with chain stiffness but does not at all depend on chain length (chapter 4, [FKMP99]). Therefore, the experimental results should be interpreted in dynamical terms only. To fully understand the processes leading to the experimental observations, more efforts are needed from experimental, theoretical and simulational points of view.

The reorientation behavior supports the concept of reptation. However, the existence of a time-dependent plateau value of reorientation with diffused way means that the motion of the tube itself has to be considered, and that it probably corresponds to a subdiffusive translation with orientation largely preserved. The reptation can be more clearly seen if the chains are stiffer. This increased stiffness leads to two effects. The local bending rigidity is increased, and the degree of entanglement ($^{N}/_{N_{\mathrm{e}}}$) is enhanced. This confines the chain more closely to the primitive path of the tube. Here indications of the scenario of the transition from *loosely entangled* to *tightly entangled* semiflexible chains, as suggested recently, can be seen (sec. 2.4.4) [Mor98b]. However, the limit $l_{\mathrm{e}} \gg l_{\mathrm{p}}$ is not reached.

5.2 Rouse mode analysis

The presented simulations cover the transition from full flexibility to an appreciable degree of stiffness. It is of interest to which extent the Rouse model is still applicable. Additionally, the chain lengths range from dimers to lengths in the entangled regime.

According to the Rouse model the normalized auto-correlation functions of all Rouse modes (in the following denoted by the index p) collapse onto a master curve for one system if time is

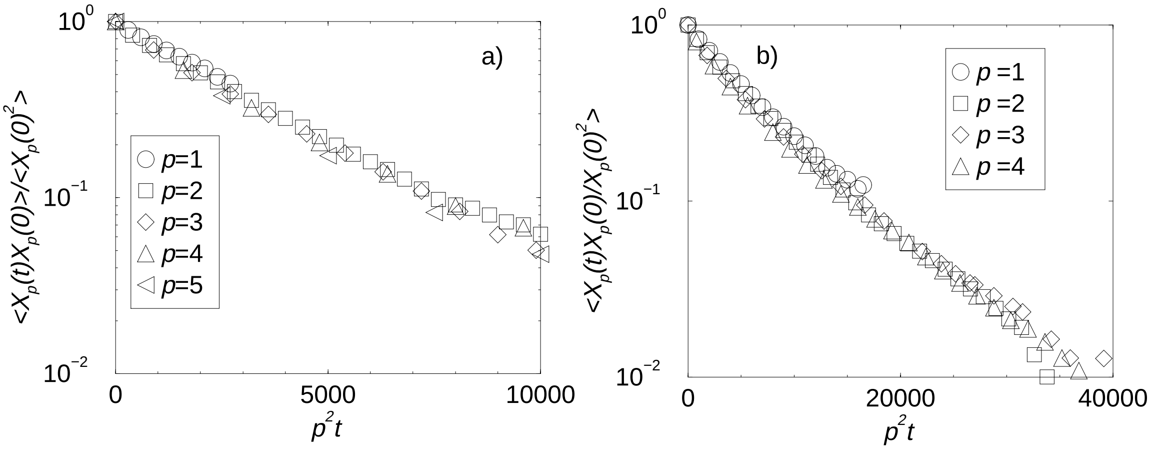

Figure 5.8: Collapse of Rouse modes for relatively short and flexible systems. The time axis is rescaled by the mode number squared. The amplitudes are normalized to $\langle X_p(0)X_p(0)\rangle = 1$.
a) $x = 0,\ N = 50$, b) $x = 1.5,\ N = 50$.

rescaled by the square of the mode number (see section 2.2). Moreover, the correlation functions of segments of the same length in systems of different chain length but same stiffness coincide. To decide whether the Rouse model is the appropriate description of a polymer melt, it is necessary to determine the Rouse modes. Furthermore, the Rouse times may help to transform times into lengths by regarding the time as the relaxation time of a subchain. This is useful for determining an entanglement length from a plot of the mean-squared displacement (sec. 2.3). This, of course, can only be applied if the Rouse model describes the system appropriately at least for short chains.

The Rouse time τ_R is the relaxation time of the slowest mode. Therefore, it can be used to determine the equilibration of the systems. Even if the Rouse model is no longer applicable, the decay time of the first Rouse mode is still a useful estimate of the relaxation time. A second estimate is the time it takes for centers of mass of the chains to move their own size, i.e. one gyration radius. For some of the shorter systems the relaxation times multiplied with the mode number of the first few modes are given in table 5.4. Without a rescaling of the friction coefficient an increase of the Rouse time τ_R with chain extension, i.e. linear with l_p, would be expected [DE86]. However, the relaxation times increase in an even stronger fashion. Additionally, for fixed stiffness the increase with N^2 as expected from the Rouse model is not observed, but the slowdown is more pronounced, indicating an earlier onset of influences of entanglements with increasing persistence length (compare tab. 5.1). For $x = 5$, the decay times can be no longer rescaled by the squared mode number whereas for more flexible chains this remains possible (tab. 5.4). Still, the lowest Rouse mode always has the longest relaxation time.

5.2.1 Short chain systems

Figure 5.8 shows the decay of Rouse modes for different systems in Rouse scaling. The Rouse collapse can be nicely seen for the fully flexible and the weakly stiffened chains at the moderate length of $N = 50$, which is already slightly more than the respective entanglement lengths (sec 5.3).

Increasing local stiffness leads to deviations, especially at high Rouse modes, which is seen in figure 5.9b. The higher modes have shorter wave length and are, therefore, more hindered by local stiffness, as the wave-length and the persistence length come into the same order, e.g. the mode

System	p	N	$p^2\tau_p$	τ_1/τ_p
0-1	1	25	735	1
0-1	2	25	723	3.93
0-1	3	25	776	9.50
0-1	1	50	3029	1
0-1	2	50	3443	3.52
0-1	3	50	3357	8.12
1.5-1	1	15	385	1
1.5-1	2	15	424	3.62
1.5-1	3	15	426	8.12
3-1	1	15	867	1
3-1	2	15	795	4.36
3-1	3	15	874	8.92
3-1	1	17	1096	1
3-1	2	17	1058	4.14
3-1	3	17	1078	9.07
3-1	1	20	1936	1
3-1	2	20	1738	3.59
3-1	3	20	1809	8.41
3-1	1	25	3184	1
3-1	2	25	3193	3.99
3-1	3	25	3092	9.27
5-1	1	5	637	1
5-1	2	5	339	7.51
5-1	3	5	1640	3.48
5-1	1	20	3905	1
5-1	2	20	3462	4.51

Table 5.4: Selected decay times of Rouse modes for different systems and modes. The scaling is at least for $x = 5$ questionable on all length scales.

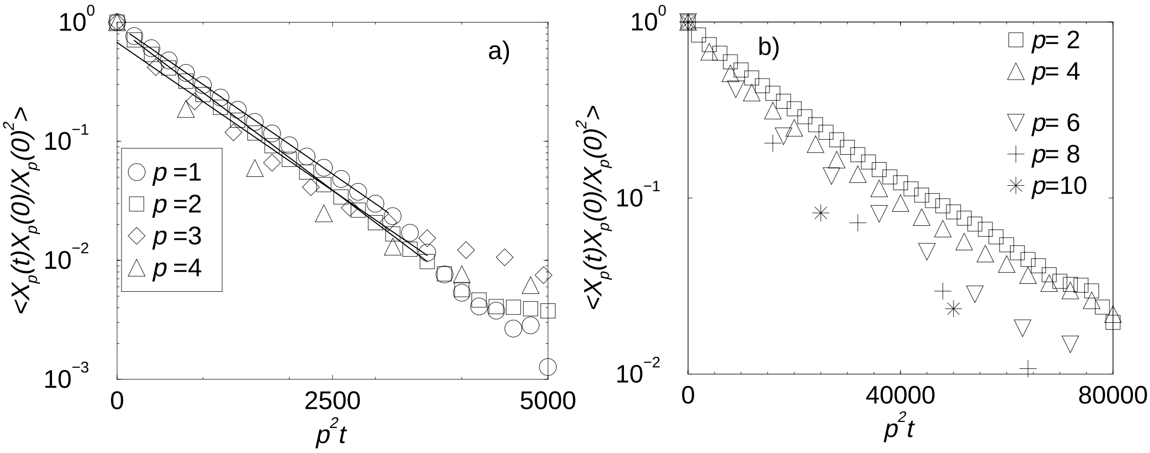

Figure 5.9: Rouse modes for $l_p = 3$, $N = 15$(a)/50(b) in Rouse scaling. The high modes show strong deviations, as they are hindered by semiflexibility. To see the slight differences, not all points actually investigated are included in the plots. The three lines in figure a) are the fits leading to the decay times denoted in table 5.4.

with $p = 10$ has for $N = 50$ a wave-length of 5 monomers which is less than two persistence lengths at $x = 3$. For the lower modes the collapse is correspondingly better.

5.2.2 Long chains

On long time scales (fig. 5.10a) the system with chains of length $N = 200$ and stiffness $x = 5$ might appear Rouse-like. It shows, however, remarkable deviations at short to intermediate times (fig. 5.10b). The collapse is no longer possible by simple rescaling with p^2. The dynamics of these chains is different; the Rouse model breaks down. The reorientation (sec. 5.1) already hints that these chains are entangled. Also, the Rouse relaxations are much slower than for chains of the same length but with full flexibility [DGK98]. As they prefer to move along their contour the Rouse model cannot be expected to hold.

In figure 5.10b the modes with indices 3 and 4 collapse quite nicely. The two lowest modes cannot be decided yet, as they are not well relaxed. There is some indication that they decay more slowly than the higher modes. This would be in line with the influence of entanglements acting on long distances; the higher modes ($p \approx 5-7$) decay in Rouse scaling apparently faster than the lower modes. Even with full flexibility, the Rouse scaling breaks down at $N = 350$ (fig. 5.10c). As there is evidence that the long and stiff chains cannot be described by the Rouse mode, other descriptions have to be looked for. Also, it will be shown that the reptation concept is not able to describe these systems satisfactorily.

5.2.3 Chain-length dependence and friction coefficient

According to the Rouse model the modes of systems with different length, but otherwise same parameters, can be rescaled onto a master curve. At $x = 1.5$ this is not possible for $p = 1$ (fig. 5.11a). Analyses of higher modes yield analogous results. For the flexible system the scaling works well at least up to $N = 50$ [Püt99]. The discrepancies from the predicted scaling behavior increase with chain length. The Rouse model seems to work approximately for short chains $N \lesssim 20$, although even there influences from chain length are visible. For longer chains, the relaxation time is not

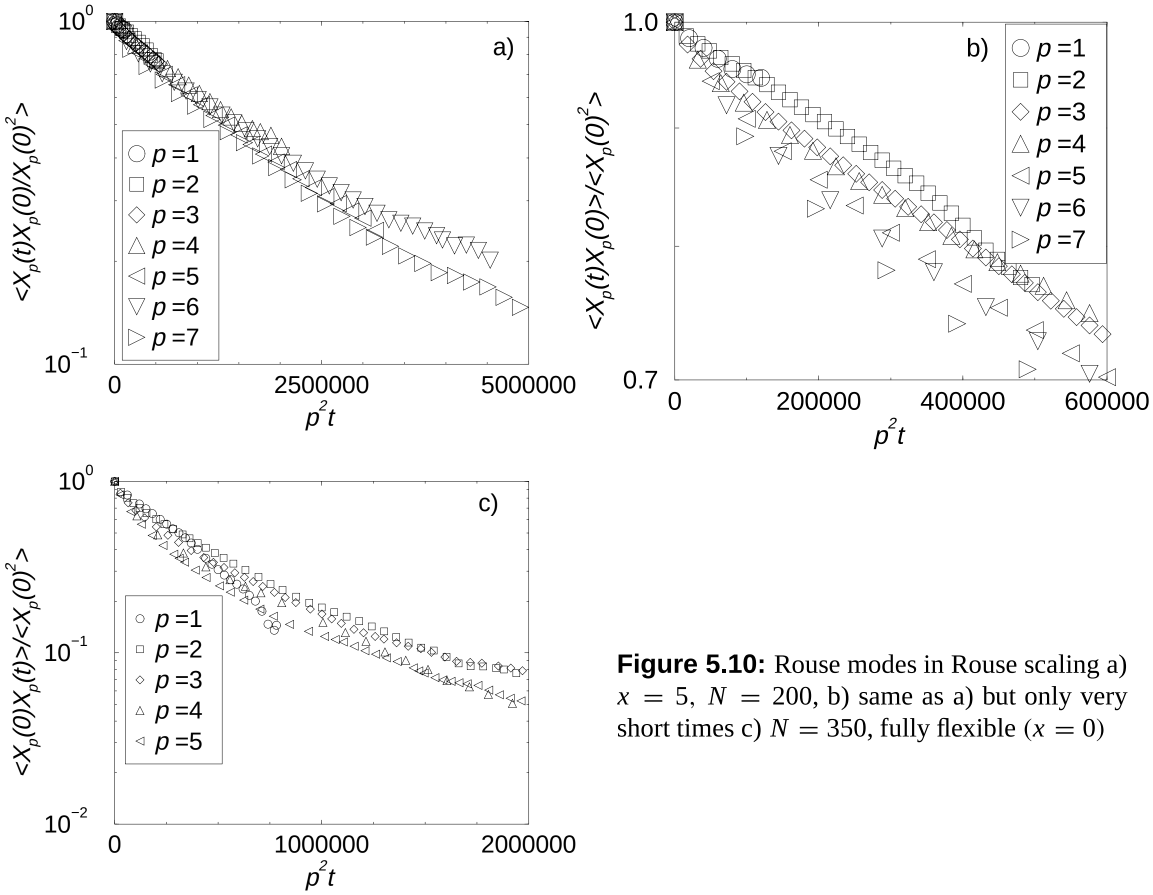

Figure 5.10: Rouse modes in Rouse scaling a) $x = 5$, $N = 200$, b) same as a) but only very short times c) $N = 350$, fully flexible ($x = 0$)

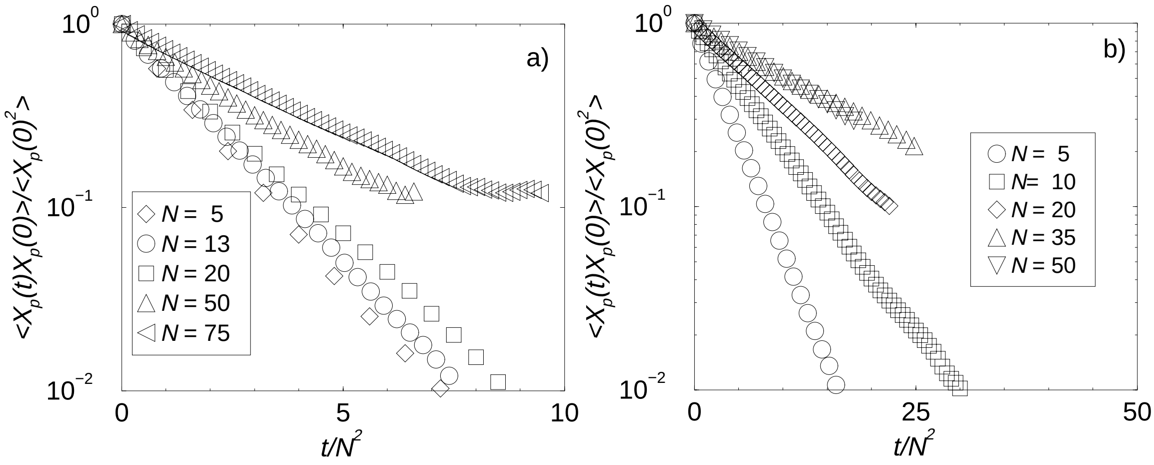

Figure 5.11: The first modes for different chain lengths do not obey a perfect Rouse scaling. Part a) shows this for $x = 1.5$ and part b) for $x = 5$.

x	N	ζ
0	50	24
1.5	20	25
3	20	34
5	20	45

Table 5.5: The friction coefficients of the Rouse model depending on chain stiffness. Only a limited range of chain lengths can be used.

quadratically dependent on chain length. Thus, the onset of entanglement influences is supported. For $x = 5$ there is no Rouse scaling at any chain length (fig. 5.11b).

From the Rouse times the friction coefficient can be calculated (sec. 2.2):

$$\zeta = \frac{3\pi^2 k_B T}{N\langle R^2_{\text{e-e}}\rangle}\tau_{\mathrm{R}} \; . \tag{5.5}$$

This is only possible as long as the Rouse model is the appropriate description. Thus, in table 5.5 not only the friction coefficients but also the chain lengths from which they are calculated are presented. The friction increases for weak stiffness only slightly. For stronger stiffnesses the concept as a whole becomes questionable.

5.2.4 Applicability of the Rouse model

With increasing stiffness the Rouse model is no longer appropriate. It may still be used to estimate relaxation times. However, the Rouse scaling fails, as the dynamics is changed on local scales. Even for the weak stiffness of $x = 1.5$ there are only about 6 Kuhn-segments in the range of the entanglement length (see section 5.3). There is less than a decade of chain lengths, where the Rouse model may describe the dynamics. Therefore, chains of different lengths cannot be mapped onto each other by Rouse scaling.

One can say that the Rouse model works satisfactorily for flexible and weakly stiff chains $x \lesssim 3$ of lengths between persistence and entanglement length. The stiffer systems have a different underlying dynamics, and the longer chains are entangled, which leads to a violation of the assumption of free motion parallel and perpendicular to the backbone. The Rouse regime is “dissolved” between the two extremes. The long wavelength side is suppressed by the entanglement, whereas the short modes are prevented from Rouse motion by the stiffness.

The long Rouse times for semiflexible chains suggest relatively short entanglement lengths, as τ_{e} does not increase so drastically, which again is in line with the other observations concerning entanglement length versus persistence length (sections 5.1 and 5.3).

5.3 Chain diffusion and mean-squared displacements of monomers

5.3.1 Center-of-mass diffusion

As discussed in sections 2.2 and 2.3, the mean-squared displacements of inner monomers and of the center of mass, which corresponds to the diffusion of the whole chain, are key observables for describing the dynamics of polymer chains in the melt. From the center of mass diffusion an entanglement length l_{e} can be determined, which is not necessarily the same as defined by the experimental plateau modulus. However, l_{e} is a characteristic chain length above which the

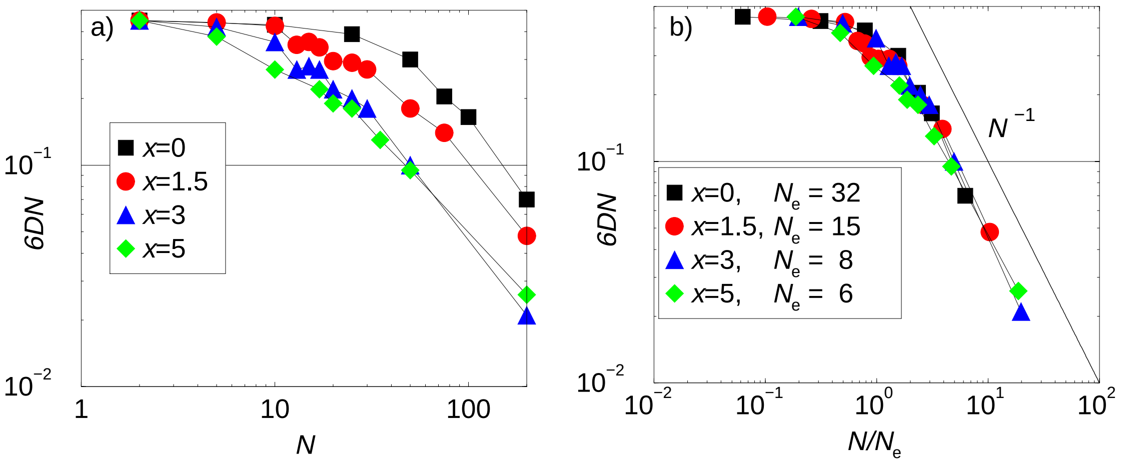

Figure 5.12: Overall chain diffusion coefficient multiplied with chain length. A plateau denotes Rouse behavior. a) Simple presentation of the data for the different stiffness parameters. Some of the values for $x = 0$ are from refs. [KG90, DGK98]. The crossing of the lines at $N \approx 100$ is not to be taken too serious as there is still statistical uncertainty. However, below $N \approx 50$ the errors are at most of the order of the size of the symbols. b) Same as a) but rescaled empirically to define an entanglement length. The rescaling was done with $N_e(x)$ shown in table 5.6. The solid line has a slope of -1, indicating $D \propto N^{-2}$ as expected from reptation theory.

dynamics of the chains becomes much slower, which is associated with the constraining of the chains into tubes.

The following definition of an entanglement length will be used: the “point”, where the diffusion constant starts to deviate from the Rouse behavior of $D \propto N^{-1}$, i.e. the kink in the plot of the diffusion constant multiplied by chain length against chain length. According to the Rouse model the center-of-mass, i.e. long-time, diffusion coefficient decreases linearly with chain length. With the onset of entanglements the diffusion coefficient drops even faster than $\propto N^{-1}$ (N^{-2} for reptation). If the diffusion coefficient multiplied by chain length is plotted versus chain length a plateau indicates simple Rouse behavior, and a drop with $1/N$ indicates reptation. In section 5.2 it was shown that the Rouse model is not fully appropriate to describe the short-chain dynamics. Still, it is used here as point of reference.

The overall chain diffusion constant could be determined for the shorter chains (up to $N = 75$) at all stiffnesses; For longer chains prohibitively long simulation times prevented an exact determination; and for the fully flexible case the results of Kremer *et. al.* [KG90] could be reproduced: up to $N_e = 32$ the diffusion coefficient decreases with $1/N$, as expected from the Rouse model (fig. 5.12). In the fully flexible case there are several detailed determinations of N_e producing similar results [KG90, Püt99, PKG00].

The behavior of $D(N)$ changes remarkably if the chains have an additional bending potential (figure 5.12a). For weak stiffnesses ($x = 1.5$, $x = 3$) two plateaus are found. The influence of stiffness on the very short chains ($N \lesssim 10$) is negligible. The diffusion constants coincide with the plateau value for fully flexible chains. Then the diffusion decreases faster than $1/N$ and arrives at a second plateau in $DN(N)$. The second plateau ends before $N = 32$; thus, l_e certainly decreases with increasing l_p. From this data one cannot elucidate the exact dependence of l_e on l_p. A linear decrease would be supported by the data. As there is still an uncertainty of about $10 - 20\%$, more simulations at different stiffnesses are necessary in order to decide on this question.

x	l_p	N_e	$N_e l_p$	d_T
0.0	1.0	32	32	6
1.5	1.4	15	22.5	5
3.0	3.0	8	24	4.5
5.0	5.0	6	30	–

Table 5.6: Values of entanglement lengths depending on persistence length determined by scaling the final decrease of DN for $N \to \infty$ with chain length (compare figure 5.12). The definition of the entanglement lengths is by no means unique, and they have an error of at least 10%. However, they decrease systematically with x, independent of definition. The tube diameters are estimated from the crossover from $t^{1/2}$ to $t^{1/4}$. For $x = 5$ this is not possible.

At first sight it is not clear, which of the two lengths marking the ends of the corresponding plateaus is the entanglement length. As the reptation model predicts for long chains $D \propto N^{-2}$, and in the motion of inner monomers with time (sec. 5.3.2) there is no hint for a slowdown before the end of the second plateau, the rescaling in figure 5.12b was done in order to match the final decay ($N \to \infty$) to define l_e.

For even higher stiffness ($x = 5$) both plateaus vanish completely. Therefore, no Rouse regime remains (compare section 5.2). At short scales, the local bending, dominated by the persistence length l_p, does not allow the chain to move perpendicular to its contour. At only slightly longer length scales, the influence of entanglements sets in early. The persistence length and the entanglement length are in the same order of magnitude (table 5.6). Therefore, the dynamics cannot be described by one of the two effects alone.

Figure 5.13b shows the mean-square displacement of the center of mass of entangled chains. For $x = 1.5$ one sees the difference between $N = 75$ and $N = 200$. Although the chains of length 75 are already entangled (see g_1 below) this is not observed in g_3. At $N = 200$, in contrast, the center-of-mass motion shows a slowdown on intermediate time scales. For the stiffest chains the motion is slow and close to a $t^{1/2}$ behavior. The chain and with it the center-of-mass moves diffusively in the tube and, thus, subdiffusively in cartesian space. For $t \ll \tau_d$ the center of mass is in the standard reptation picture expected to move with $t^{1/2}$ [DE86].

In studies of blends of flexible chains of different lengths it was observed that the diffusion of chains shorter than the entanglement length is slowed down if the longer species is entangled [Bar00]. This supports the picture that for short times the neighbor chains form a quasi static matrix in which the chain has to move.

5.3.2 Mean-squared displacements of central monomers

Figures 5.13a,c,d show $g_1(t) = \langle [\vec{R}(t)_{N/2} - \vec{R}(0)_{N/2}]^2 \rangle$ for different systems. The fully flexible bead-spring case is quite well understood by theory and simulation [de 71, DE86, KG90, PKG00]. Results of former simulation could be reproduced where available. Increasing the local stiffness, one finds first a slight decrease of the tube diameter d_T, determined by the kink from $t^{1/2}$ to $t^{1/4}$ (fig. 5.13a). A definition of d_T is the length at which the monomer motion starts to be constrained in a tube, i.e. where it has explored its transversal degrees of freedom. This length scale, thus, determines the transition from isotropic to anisotropic motion leading to a change in the dynamic exponent (sec. 2.3). With increasing stiffness this happens on shorter lengths. The tube diameter shrinks, which can be explained by the fewer transversal degrees of freedom of the chain as a result of the stiffness (tab. 5.6). If the chain stiffness becomes too strong, i.e. the persistence length approaches the entanglement length, as is the case for $l_p = 5$, the overall scenario changes again

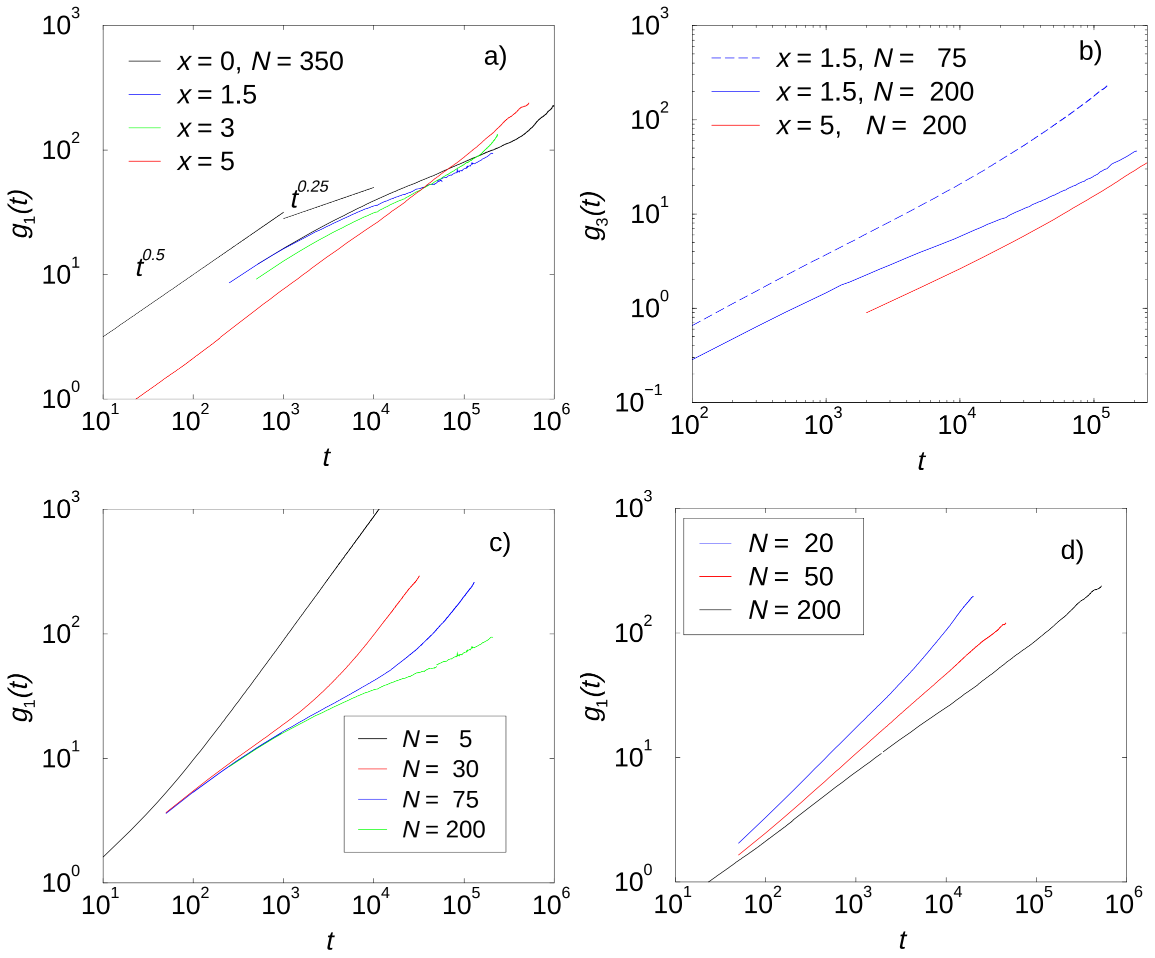

Figure 5.13: Mean-squared displacements of a) chain inner monomers (g_1) for different systems ($N = 200$) under study in comparison to b) center of mass (g_3) diffusion. c) g_1 for $x = 1.5$ at different chain lengths. d) same as c) but $x = 5$. The two thin lines in figure a) indicate the slopes for $t^{1/2}$ and $t^{1/4}$.

drastically. Here the $t^{1/4}$ regime is no longer observed; g_1 starts with $t^{1/2}$ and retains this exponent until free diffusion. However, as discussed earlier, these chains are highly entangled. There is no Rouse scaling, and the reorientation shows the typical reptation exponent clearly indicating a non-isotropic motion. So one has to conclude that the motion of these chains starts directly with the second $t^{1/2}$ regime, although at first sight g_1 looks as expected from the Rouse model. The chain reptates from the beginning as the tube diameter approaches its lower limit, which actually is the chain thickness. If one looks very optimistically at the $x = 5$ curve, a weak “s-shape” is found in the initial part of the $t^{1/2}$-regime of g_1 which is probably the remainder of the $t^{1/4}$-regime. The curve for $x = 3$ is inbetween the two extremes. It already cuts through the curves of weaker stiffness but still exhibits the intermediate slowdown. Thus, there is a smooth crossover between the two scenarios. The shape of the $x = 3$ curve indicates the second intersection between $x = 3$ and $x = 5$ as proposed in section 2.4.7 but does not reach it.

Comparing chains of the same stiffness and different lengths allows one to observe the crossover from unentangled to entangled motion (fig. 5.13c, d). Especially for the chains with stiffness 1.5 one clearly sees that with increasing chain lengths the mean-squared displacement “leaves” the $t^{1/4}$ earlier or does not reach it at all. For stiffness 5 there is no qualitative difference, as the entanglement length is very short.

It is questionable whether the standard reptation picture still applies to the highly entangled stiff chains, as the underlying assumption of a Rouse dynamics governing short chains is violated. But, the other extreme is not yet reached in the models under study. This would be a slightly flexible rod characterized by a quantity like the deflection length of Odijk [Odi83], whereby a rod is pressed into a curvilinear tube being deflected from wall to wall (see section 2.4.3). In this case the nematic ordering transition would be crossed for melt densities. However, overall isotropy is ensured for all the model polymer melts under study. Since the models do not fall into any of the theoretically understood limits and, on the other hand, do have stiffnesses of experimental polymers, simulation appears to be the only way to study them for the time being.

It is not easy to define an entanglement length uniquely, as there are several different definitions leading to different lengths. One often defines the time, when the free Rouse regime in g_1 ends, as an entanglement time, and then relates this to an entanglement length. The entanglement times estimated this way are $\tau_e \approx 1500$ for $x \leq 3$ rather independent of stiffness, for $x = 5$ this estimate does no longer work. This needs a model to relate a relaxation time to the length of a correspondingly relaxing subchain for given stiffness. The Rouse model provides this link for flexible chains. The l_e defined this way is for flexible chains compatible with the value defined as above in the scaling behavior of the diffusion coefficient. For higher stiffness the definition from the crossover from free Rouse motion to Rouse motion in the tube is no longer applicable.

Simulations with deformation might be helpful, as they provide a more direct link to the experimental definition of the entanglement length. For the fully flexible case it was shown that the two lengths, the one defined here and the other extracted from the plateau modulus, differ by about a factor of 2 [Püt99, PKG00].

Recently, it was demonstrated that non-interpenetrating semiflexible ring polymers have two dominant length scales even in the *statics*, one of which connects to the topological interplay between chains [MWC00]. In that case entanglements influence the statics of the chains as well. For N bigger than a characteristic length associated to the entanglement length, the ring diameter scales no longer with $\nu = 0.59$, i.e. slightly stretched like a chain in good solution, but with $\nu = 1/3$ indicating a compact object. Thus, the rings collapse with increasing chain length and stiffness. The length scale, where this transition occurs defines a local scale of freedom which is used by Müller *et. al.* to define a tube diameter. This is not possible for the systems presented here, as in

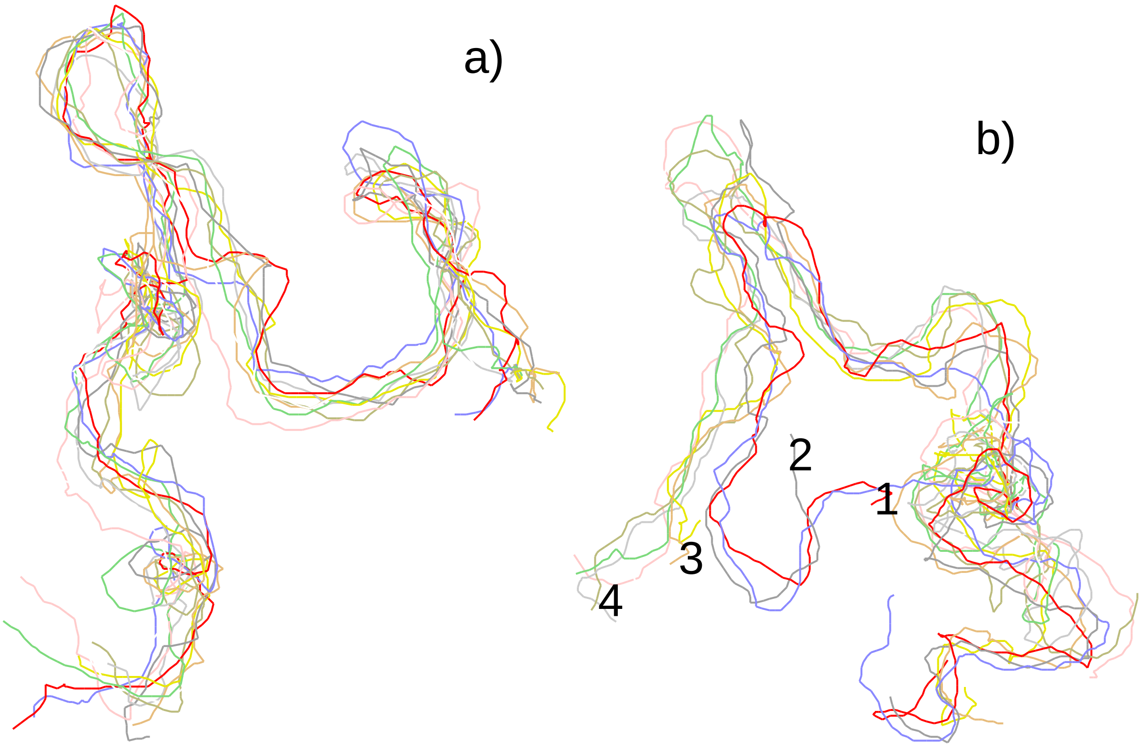

Figure 5.14: Visualization of the reptation tube for the system with $N = 200$, $x = 5$. The monomer positions encountered at snap shots of time interval a) $\Delta t = 10000$, b) $\Delta t = 100000$ are recorded. One clearly sees that the ends start to explore their freedom whereas the inner parts remain in the tube. Even for $t = 100000$ the inner part of the tube remains intact. Note the transverse shift of chain parts under conservation of orientation.
The program VMD [HDS96] was used for the visualization.

linear chains this only shows up in the chain dynamics.

5.4 Motion along the tube

An illustrative picture of reptation in a tube is provided in figure 5.14, where over some time the positions of all the monomers of a chain are plotted in one figure. The tube-like arrangement of the average position is seen clearly; especially in part b the end on the left hand side shows the destruction and rebuilding of the tube, as the end explores the positions marked with numbers of 1 to 4. In contrast to former visualizations of flexible chains [KG90, Püt99], not the primitive chain but the chain itself is shown here.

Additionally, the correlation of the direction of a displacement of a monomer with the local chain direction clearly indicates the anisotropy of the segmental motion (fig. 5.15). The following correlation function

$$\Pi(t) = \left\langle P_2 \left(\frac{\vec{R}_n(t) - \vec{R}_n(0)}{|\vec{R}_n(t) - \vec{R}_n(0)|} \cdot \frac{\vec{R}_{n+i}(t_0) - \vec{R}_{n-i}(t_0)}{|\vec{R}_{n+i}(t_0) - \vec{R}_{n-i}(t_0)|} \right) \right\rangle \tag{5.6}$$

allows a closer analysis. In figure 5.15 $t_0 = 0$ as well as $t_0 = {}^t/_2$ are chosen. $\Pi(t) = 1$ indicates motion exclusively along the contour, $\Pi(t) = 0$ corresponds to isotropic motion. For $t = 0$ (as

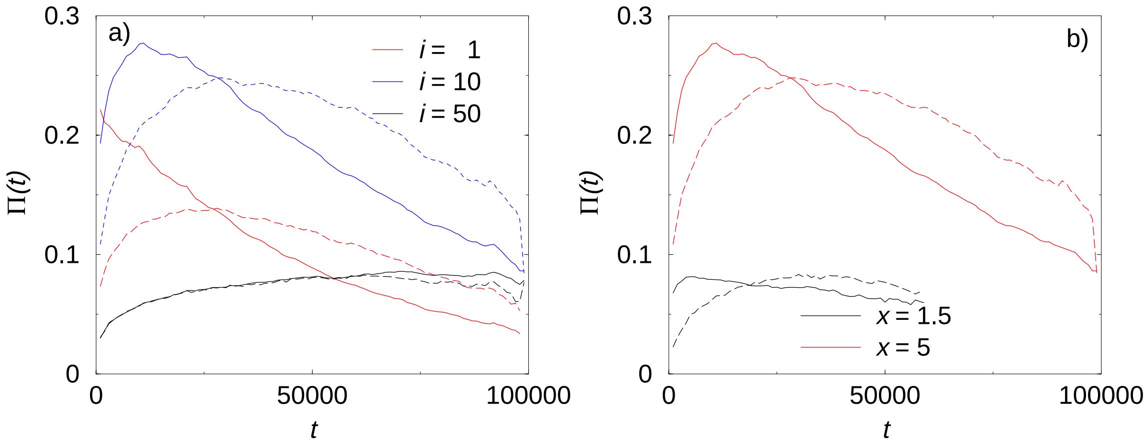

Figure 5.15: Correlation of chain direction vectors with displacements demonstrated using the function Π defined in eq. (5.6). The solid lines denote $t_0 = 0$, the dashed lines $t_0 = {}^t\!/2$.
a) Different lengths of segments for $x = 5,\ N = 200$.
b) Different systems at $i = 10,\ N = 200$.

x	p	$N_e^{(\text{pack})}$
0	0.697	62.7
1.5	0.436	15.3
3	0.223	2.1
5	0.133	0.4

Table 5.7: Entanglement lengths derived by applying the packing length concept (for $N = 200$, except for the fully flexible, whereby $N = 350$). They vary much more than observed in simulations. Additionally, the packing lengths themselves are given.

well as for $t_0 = t$ by time-inversion symmetry) the correlations decrease with increasing time, for $t_0 = {}^t\!/2$ there is an increase in the beginning, as the time to which the displacement is correlated is in the center of the interval. Figure 5.15a shows that the tube has a correlation length, as for $i = 10$ the correlations are bigger than for $i = 1$ and for $i = 50$: on the very short scale there is still some transversal motion possible. At $i = 10$, which corresponds to a direction vector of the size of two Kuhn lengths, there is a high degree of persistence of the tube. On longer length scales the overall random walk character already shown in the single chain structure factor (sec. 4.3) shines through as long segments ($i \gg l_\text{p}$) average over uncorrelated parts of the tube. The chains of higher stiffness follow the tube more closely, as there is more correlation between the displacement vectors and the direction of the chain (fig. 5.15b).

5.5 Comparison to theoretical predictions

In subsection 2.4.5 the concept of a packing length was presented. From this one should be able to calculate entanglement lengths from static chain properties by using the formula [FLG99]

$$M_\text{e} = 218 \rho p^3. \tag{5.7}$$

The proposed dependence $l_\text{e} \propto l_\text{p}^{-3}$, however, is not confirmed by simulation. The entanglement lengths calculated by this concept are shown in table 5.7. For $x = 1.5$ the prediction agrees well with the definition in section 5.3; for full flexibility it deviates by a factor of two; for the higher stiffnesses the entanglement lengths are clearly too short. The packing length p itself (or more stringently about $40p$) may be more appropriate than the derived N_e to describe entanglements, as apparently there is a linear dependence between the two lengths supported by simulations. The data of table 5.7 has to be interpreted with some caution, as the mass and length mapping are not really established. Here monomer numbers and masses are the same. If stiffness is not too strong, the packing length concept can provide a rough estimate of the entanglement lengths. Between full flexibility and $x = 1.5$ the calculated values differ only in the range of factors of 2 to 3 from the data resulting from simulations.

The Morse concept (sec. 2.4.4) suggests a slight increase of the entanglement length with l_p. The conceptual picture of the high entangling resembles the motion encountered in the simulations. Still, the scaling of l_e fails, at least for the parameter area investigated here as l_e does not rise with l_p. The Wu concept (sec. 2.4.1) cannot at all describe the observations.

5.6 Dynamical structure functions

Neutron-spin-echo experiments measure the dynamic structure function of polymer melts [ER97]. Evidence for reptation was claimed for polyethylene chains [SFL⁺98]. For the Rouse model (see e.g. [DGK98]) and for short semiflexible chains [HWR97] this property can be derived analytically

$$\text{Rouse} \quad : \quad \frac{S(k,t)}{S(k,0)} \propto e^{-const\cdot k^2 t^{1/2}} \;, \tag{5.8}$$

$$\text{Semiflexible} \quad : \quad \frac{S(k,t)}{S(k,0)} \propto e^{-const\cdot k^2 t^{3/4}} \;. \tag{5.9}$$

For reptating chains de Gennes has calculated the structure factor [de 81], from which Kremer and Binder derive the following expression, which has the advantage that in contrast to the original formulation it decays exponentially with $t \to \infty$ [KB84]

$$\begin{aligned} \frac{S(k,t)}{S(k,0)} &= \left\{ 1 - \left(\frac{k d_\mathrm{T}}{6}\right)^2 f\left[k^2 l_\mathrm{b}^2 \left(\frac{3 k_B T}{l_\mathrm{b}^2 \zeta} t \right)^{1/2} \right] \right\} \times \\ & \qquad \frac{8}{\pi^2} \sum_{p=1}^{\infty} \frac{1}{(2p-1)^2} \exp\left(- \frac{t(2p-1)^2}{\tau_\mathrm{d}} \right) \;, \end{aligned} \tag{5.10}$$

$$f(u) = \exp\left(\frac{u^2}{36}\right) \operatorname{erfc}\left(\frac{u}{6}\right) \;. \tag{5.11}$$

Influences from the tube express themselves by a plateau-like time domain in in the decay of the structure factor. The dynamic structure factor for different systems is shown in figure 5.16. Increasing stiffness changes the behavior; the plateau arising from the tube increases indicating a stronger confinement, i.e. a tube diameter shrinking with l_p.

The modulus k of the wave vector has to fall in the range $2\pi/R_\mathrm{gyr} \lesssim k \lesssim 2\pi/d_\mathrm{T}$ to be in the scaling regime between the tube diameter and the radius of gyration. On these length scales constraints from the tube are expected. For flexible chains the tube diameter is estimated to be $d_\mathrm{T} \approx 7$ from mean-square-displacements and the radii of gyration are for $N = 200$ between 88 ($l_\mathrm{p} = 1.4$) and 277 ($l_\mathrm{p} = 5$). Thus, the k-vector range of [0.1..0.7] should be appropriate for the analysis. A slowdown of modes at persistence length five is even found for $k = 2.0$, whereas for the flexible case this mode decays very fast indicating that on scales of about 3 monomer diameters tube influences are found for stiff ($x = 5$) chains but not for the more flexible ($x = 1.5$) case (fig. 5.16c).

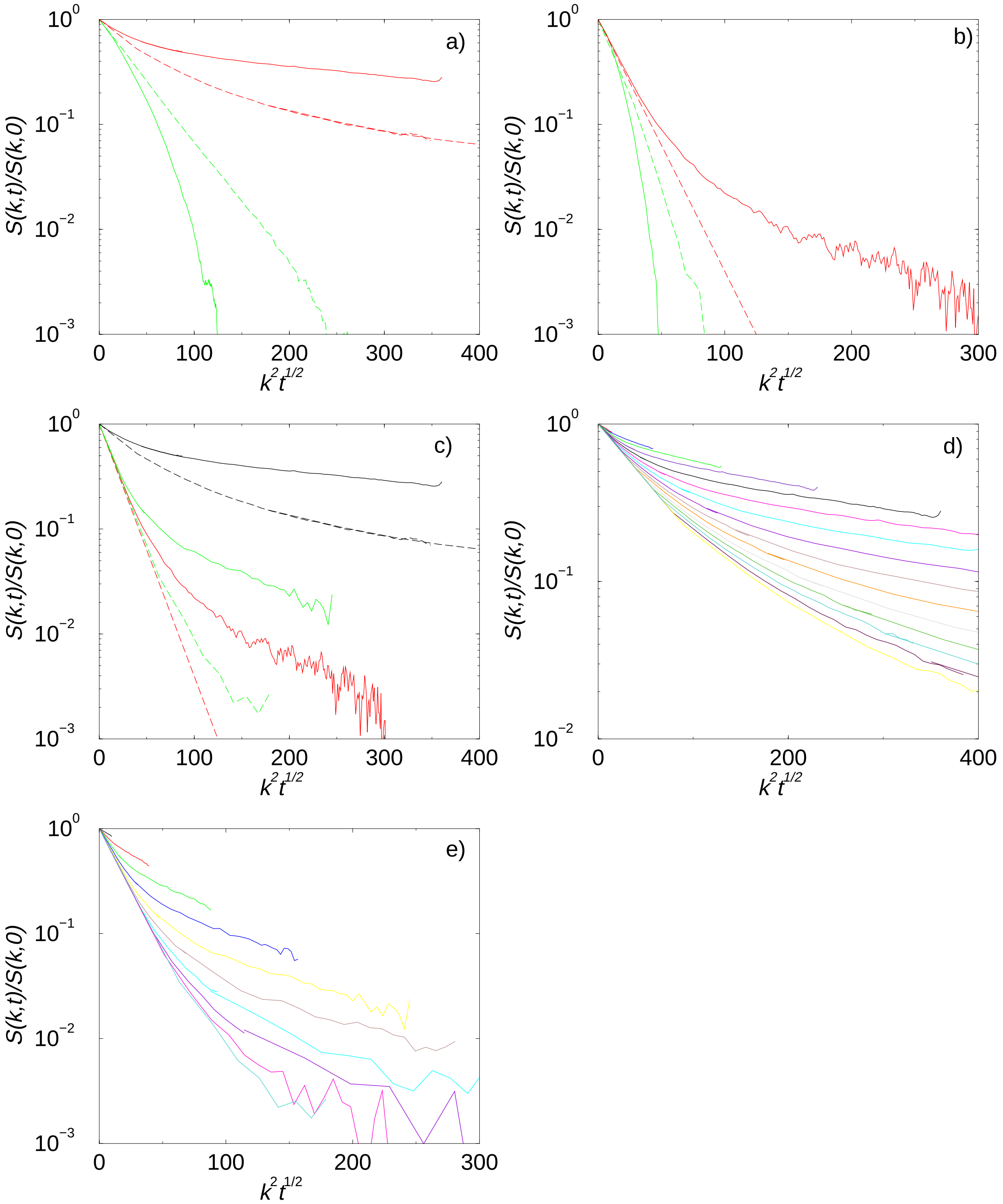

Figure 5.16: Dynamical structure functions for a) systems with persistence length 5, b) fully flexible systems.
In part a) and b) the red lines correspond to chains of length 200, the green to chains of length 25. The solid lines are $k = 1.0$ and the dashed lines $k = 2.0$.
c) compares for $N = 200$ and different persistence lengths 1.0 ($N = 350$, red), 1.5 (blue), and 5 (black). The solid lines are $k = 1.0$ and the dashed lines $k = 2.0$.
d) wavelength dependence for $N = 200$, $l_\mathrm{p} = 5$. From top to bottom the wavelength increases in steps of 0.2 from 0.2 to 3.0. e) Same as d) but $l_\mathrm{p} = 1.5$, $k_\mathrm{max} = 2.0$.

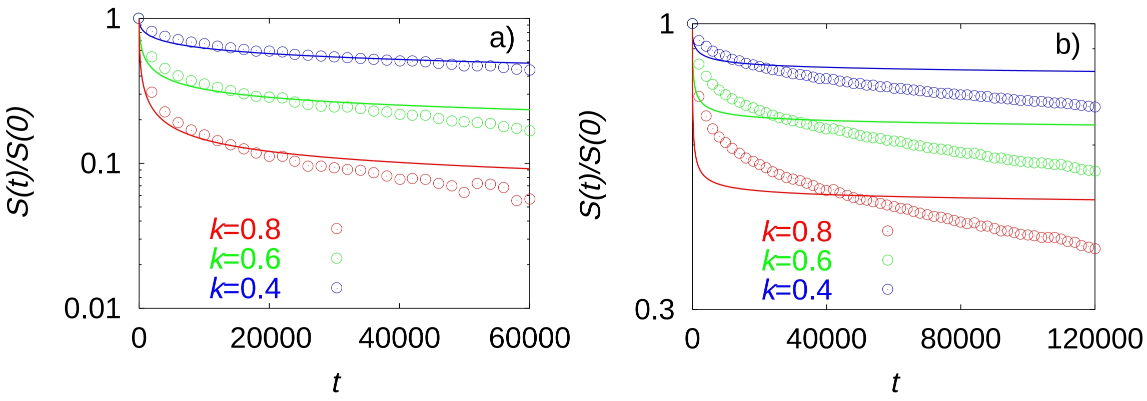

Figure 5.17: The dynamic structure functions are fitted with eq. (5.10) for $N = 200$.
a) $x = 1.5$ b) $x = 5$. Note the different scales on the axes.
The tube diameters obtained by fitting are too big. For $x = 5$ the classical reptation model is not appropriate.

Comparing parts d and e of figure 5.16 one sees that the Rouse scaling for short times works quite well for the rather flexible case of $x = 1.5$, whereas it fails for $x = 5$. For long times the structure factors deviate clearly from Rouse behavior in both cases. The decay is much slower leading to a real plateau for the rather stiff chains.

By fitting

$$\frac{S(k,t)}{S(k,0)} = \exp\left(-2\sqrt{\frac{k_B T}{12\pi\zeta}} C_\infty l_b^2 k^2 \sqrt{t}\right) \tag{5.12}$$

to the initial decay the friction coefficient of the Rouse model can be estimated [KG90, Püt99]. Pütz has determined $\zeta = 27$ for fully flexible chains close to the value derived from the decay of Rouse modes. For $x = 1.5$ one arrives at $\zeta = 30 \pm 5$, which matches the value derived from the Rouse times for $N \leq 20$ where scaling with N^2 applies (sec 5.2). For $x = 5$ a coefficient of $\zeta \approx 45$ can be estimated. However, the Rouse model is not the true dynamical description.

With the Rouse friction, equation (5.10) can be fitted to the dynamic structure factors (fig. 5.17) in the intermediate range of scattering vectors and for big times but $t \ll \tau_d$. The tube diameters fitted this way come to $d_T(1.5, 200) = 12.2$, $d_T(3, 200) = 8.7$ and $d_T(5, 200) = 6.1$. The fits were performed at $k = 0.6$ and $k = 0.8$ respectively. The disengagement time τ_d was estimated using the standard reptation picture (eq. (2.29)). Better fits would be possible if additionally ζ and τ_d would be changed. However, the values of d_T do not change much then. For $x = 1.5$ and chain length $N = 75$ a tube diameter of $d_T(1.5, 75) = 15.4$ was determined this way. For $x = 5$ the friction coefficient is not well defined (see above), but changing ζ changes the tube diameter only little. The discrepancies for the other k-vectors in figure 5.17b indicate again that the formula derived from the classical reptation model is only a weak approximation to the observed structure factors as the classical reptation picture is a weak approximation to the dynamics of the system.

Figure 5.18 shows a data collapse for $x = 1.5$ and chains of length 75 and 200 in one single

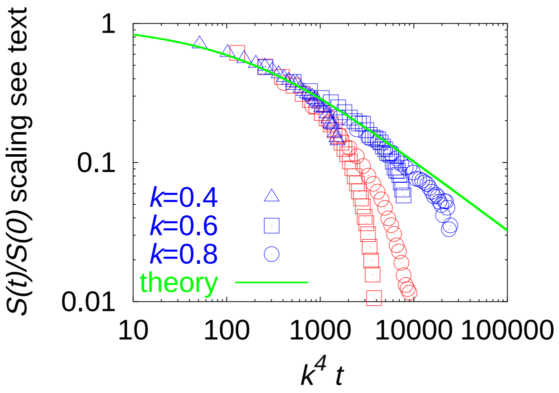

Figure 5.18: Data collapse of the dynamic structure factor $N = 75$ (red) and $N = 200$ (blue) at $x = 1.5$. Additionally the analytical shape of the expected curve is shown for comparison (green).

plot. To do this, the sum in equation (5.10) was approximated by an integral. This yields

$$\begin{aligned} f(t,N) &:= \frac{8}{\pi^2}\sum_{p=1}^{\infty}\frac{1}{(2p-1)^2}\exp\left(-\frac{t(2p-1)^2}{\tau_\mathrm{d}}\right) \\ &= \exp(-64{}^{x}/{}_{\pi^4}) - 8\frac{\sqrt{x}}{\pi^{3/2}}\operatorname{erfc}\left(8\frac{\sqrt{x}}{\pi^2}\right), \\ x &= \frac{t}{N^3}\,. \end{aligned} \tag{5.13}$$

Rescaling time with the square of the modulus of the wave-vector and plotting

$$S = \frac{\frac{S(k,t)}{S(k,0)}\cdot f^{-1}(t,N) - \exp(-{}^{k^2 d_\mathrm{T}^2}/{}_{36})}{1-\exp(-{}^{k^2 d_\mathrm{T}^2}/{}_{36})} \tag{5.14}$$

allows to collapse curves with a chain length dependent tube diameter. The tube diameters were "by hand" determined in order to yield the best collapse: $d_\mathrm{T}(200) = 14$ and $d_\mathrm{T}(200) = 17$. Especially for the longer chains the collapse works well. For $N = 75$ the limit $t \ll \tau_\mathrm{d}$ is violated as the chains move freely at $t \approx 10^5$. This leads to the red curves leaving the master-plot early.

The tube diameters are apparently too big compared with the value from mean-squared displacements. This is in line with recent results for flexible chains where tremendous finite chain length effects are observed. The tube diameter calculated from the structure factor shrinks by about a factor of two by increasing the chain length from 700 to 10000 [PKG00]. Thus, chains of length 200 are very short for this determination, especially at $x = 1.5$. And from $N = 75$ to $N = 200$ a decrease in the tube diameter is found. The obtained values are therefore (much too high) upper limits. Still, relative numbers are meaningful.

The dynamic structure factors round up the picture which is indicated by reorientation, mean-squared displacements and visualization. The introduction of local stiffness leads to a more pronounced reptation. The standard reptation picture, however, is for the stiffest systems $l_\mathrm{p} = 5$ no longer appropriate. One has to look for alternative descriptions where the confinement in a tube is still included but without underlying Rouse dynamics.

5.7 The dynamics: A short overview

Concluding the dynamics of the model chains, one finds that for a given chain length local stiffness leads to a slowdown of all relaxations. This can be found in Rouse times, in reorientation

x	$d_\mathrm{T}^{(\mathrm{msd})}$	$d_\mathrm{T}^{(\mathrm{str})}$	$N_\mathrm{e}^{(\mathrm{diff})}$	τ_e	$N_\mathrm{e}^{(\tau)}$
1.5	5	12.2	15	1300	25
3	4.5	8.7	8	1300	18
5	–*	6.1	6	–	–

Table 5.8: An overview of the results of this chapter: The influences of stiffness onto the key observables discussed in the preceding sections. The two tube diameters arise from the mean-squared displacements and from the motion of central monomers as expressed in the dynamic structure factor.

The entanglement times are determined by the (weakly defined) crossover from $t^{1/2}$ to $t^{1/4}$ in g_1. There are errors in the range of 25%.

The two different entanglement lengths come from the kink in the diffusion coefficient and from relating the entanglement time tentatively to a length.

*: The tube diameter for $x = 5$ is too small to be measured by the mean-square displacement and τ_e is not definable.

correlation functions relevant for the NMR experiments, and in the chain diffusion. The influence of constraints from the surrounding is, additionally, more important for stiffer chains.

Most theoretical concepts presented in section 2.4 lead into this direction except for the topological hooking model, which can be ruled out. The other models are mainly valid in the limit of very weak flexibility. But this limit is not of interest here. So there is need for new theoretical considerations in the interplay of topology and local stiffness.

The systems under study cover the range from short fully flexible, i.e. Rouse, chains to locally stiff and highly entangled chains, a limit not yet described by theory. Table 5.8 gives an overview over the different entanglement characteristics as a function of stiffness. The entanglement lengths defined by relating the crossover time to a length differ by about a factor of two from the one by the diffusion coefficient. Only for long flexible chains coincidence can be expected as the standard theory applies.

Increasing chain length leads, as discussed, from unentangled to entangled motion of polymers. Thus, one can classify the systems (tab. 5.9). NMR results for polybutadiene can partly be explained by the reptation of stiff chains. However, the term *reptation* may be misleading as it is often associated to the de Gennes/Edwards picture. There is a snake-like motion of a chain in a tube, not a primitive path of a chain moving in a tube allowing locally a great degree of freedom.

	short	long
flexible	Rouse almost exponential reorientation	standard reptation algebraic reorientation on low value
stiff	no simple description almost exponential reorientation	nonstandard reptation tight tube strongly anisotropic algebraic reorientation on a high value

Table 5.9: Overview over the covered range of models. The flexible simulations are rather well understood, whereas the stiff systems are (especially the long stiff systems) are not covered by existing theories.

6 Atomistic simulations of polyisoprene

For a detailed comparison with experiments on local length scales, it is not sufficient to investigate simplified models as in chapters 4 and 5. They allow to infer generic scaling laws, but do not provide actual numbers which can be compared to experiments. Therefore, an atomistic model of *trans*-1,4-polyisoprene is developed. With this model extensive simulations are performed and analyzed for a detailed comparison to experiments.

The simulations use a stereo-regular isotactic polyisoprene with only head-to-tail connections. The two chain ends in polyisoprene are not equivalent which leads to a directionality of the chain. The monomers along a chain are numbered from left to right as in figure 6.1, so are the carbon atoms.

6.1 Technical details

Three different systems were simulated at ambient conditions (300 K, 101 hPa, tab. 6.1). One of them, in the following referred to as system 1, used constant temperature and constant volume (NVT); the two others were simulated at constant temperature and constant pressure (NpT), and are referred to as systems 2 and 3. System 1 consisted of a monodisperse sample of 100 oligomers of 10 monomers each. Systems 2 and 3 were polydisperse with again 100 chains and an average chain length of 10 monomers. The maximum of the distribution was very sharp (see below). Polydispersity is characterized by the polydispersity index, which is the ratio between the mass averaged molecular weight M_w and the number averaged molecular weight M_n. ${}^{M_w}/_{M_n} = 1$ means monodispersity

$$M_w = \frac{\sum\limits_{i=1}^{\#l} M_i^2 n_i}{\sum\limits_{i=1}^{\#l} M_i n_i} \,, \qquad M_n = \frac{\sum\limits_{i=1}^{\#l} M_i n_i}{\sum\limits_{i=1}^{\#l} n_i} \,. \tag{6.1}$$

Here n_i denotes the number of chains of mass M_i and the sum runs over all different chain lengths. System 3 was simulated at 413 K as well to look for influences of temperature. This temperature was chosen because molecular dynamics simulations of the *cis*-conformer of polyisoprene at this temperature are known [ME96, ME99].

The simulations described in this chapter were executed with the simulation package YASP originally developed by F. Müller-Plathe [MP93]. YASP uses the *leap frog*-algorithm for integrating the equations of motion (section 3.1) [AT87]. Constant temperature and, for some of the simulations, constant pressure were enforced using the Berendsen algorithm (see section 3.1) [BPvG$^+$84] with coupling times of 0.2 ps (temperature) and 8.0 ps (pressure, system 2) or 12.0 ps (pressure, system 3) respectively, at a time step of 1 fs. The pressure coupling time in system 1 was changed several times because the Berendsen manostat led to instabilities. Therefore, this system was finally simulated under constant volume conditions close

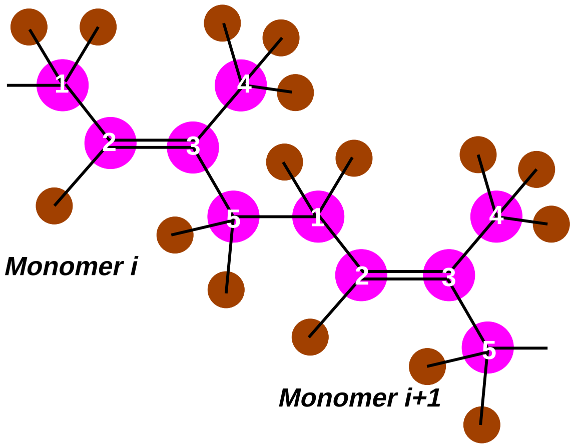

Figure 6.1: Sketch of *trans*-1,4-polyisoprene. The carbon numbers are used in the following discussions. Monomer numbers run from left to right.

System	T [K]	M_w/M_n	Ensemble	ρ [kg/m^3]	ff	t_{sim} [ps]
1	300	1.00	NVT	890	a	1184
2	300	1.05	NpT	917.4	b	2012
3	300	1.05	NpT	916.8	b	1737
3b	413	1.05	NpT	826	b	792

Table 6.1: Characteristics of the different simulated systems. The letter “a” for the force-field means that some 1-5 and 1-6 interactions are excluded. Letter “b” denotes that only non-bonded interactions up to the 4th topological neighbor are excluded (see text).

to the experimental density. The whole state of the simulation was saved every 1000 simulation steps corresponding to 1 ps of real time.

Non-bonded atoms interact by a Lennard-Jones potential [Jon24]

$$V_{\text{LJ}} = 4\epsilon\left(\left(\frac{\sigma}{r}\right)^{12} - \left(\frac{\sigma}{r}\right)^{6}\right) \tag{6.2}$$

with strength ϵ and interaction radius σ. Interactions between different atoms rely on the Lorenz-Berthelot mixing rules [AT87]

$$\sigma_{12} = \frac{\sigma_1 + \sigma_2}{2}\,, \tag{6.3}$$

$$\epsilon_{12} = \sqrt{\epsilon_1 \epsilon_2}\,. \tag{6.4}$$

The cutoff for the non-bonded interactions was set to 0.9 nm and the cutoff for the neighbor list, which was rebuilt every 10 steps to 1.0 nm [AT87]. Atoms connected by any bonding potential did not interact by the Lennard-Jones potential. Additionally, the following non-bonded interactions were suppressed: all within one monomer, and all C−C, C−H and H−H interactions between the second half of the carbons of one monomer (atoms C_3-C_5) and the first half of its following neighbor (C_1, C_2) including the hydrogens connected to them for system 1 (force-field “a”). For system 2 and 3 the latter C−H and H−H interactions were not excluded (force-field “b”, only up to “1 − 4” interactions), which leads to differences as the different torsion states bring the atoms variously to contact so that the effective energies of the torsions are shifted.

There was no electrostatic interaction in the simulation. Only carbons and hydrogens were contained in the system leading merely to weak dipole moments. The quadrupole moment of the double bond leads to very short ranged interactions which can be absorbed into effective LJ parameters. Thus, electrostatics would decrease the simulation speed without much improvement of the force-field.

6.2 The force-field

Detailed atomistic simulations need detailed force-fields. There are many different “philosophies” of how to construct them. For small molecules quantum-chemical calculations can produce useful force-fields. But even for molecules as simple as methane, today’s computer resources are at their limit, if very high accuracy is desired [RP99].

A common, empirical approach is to tune the potential parameters to reproduce experimental thermodynamic data [vGB90, MP97]. Recently, this procedure was increasingly automated by using different numerical optimization methods to actually fit potentials against the relevant properties [NvGMP95, DG99, FSBMP99, HH99]. These methods use chemical or physical insight only to guess initial values. Strictly speaking, they are formalizations of the common trial-and-error approach. Due to this nature one cannot necessarily assign a physical meaning to an individual parameter of the force-field. Only the potential energy function as a whole has a meaning in the sense that it reproduces experimental data.

Here a combination of quantum chemistry and automatic fitting against experiment was used: *Ab initio* quantum chemistry was applied to calculate the torsion potentials of the three single bonds between the monomers. The non-bonding interactions were obtained by fitting thermodynamic data of small molecules by the simplex method. Geometric data, such as bond lengths and angles, were taken from a Hartree-Fock calculation. The values are close to standard values (see tab. 6.7 below). The double bond was kept planar by a harmonic dihedral angle potential.

6.2.1 Torsion potentials

Polyisoprene has three single bonds per monomer along the backbone (fig. 6.1). The torsion angles are the relevant quantities for describing the conformation. Therefore, reliable force-field parameters are especially necessary for these degrees of freedom. In the following, a procedure to obtain the parameters is described based on quantum chemistry.

All quantum chemical calculations reported below were performed with the quantum chemistry program package GAUSSIAN 94/98 [FTS$^+$95, FTS$^+$98]. They were executed for the isoprene-dimer, which is the smallest molecule possessing all the torsion types and methyl groups present in the polymeric chain. As first guesses all torsions can be expected to be in *trans* (180°) or *gauche* (±60°) states.[1] First, the 27 possibilities were investigated with the relatively “cheap” semi-empirical MNDO method [DT77]. Four of these structures could be ruled out immediately

---

[1] Additionally *cis* (0°) and *skew* (±120°) states will be needed.

Number	Class	ΔE[kJ/mol]
1	ttt	42.96
2	g^+tg^-	0.07
3	$g^+g^-g^+$	2.05
4	$g^+g^-g^-$	2.07
5	g^+tg^+	0.0
6	$g^-g^-g^+$	5.99
7	$g^-g^-g^-$	7.08

Table 6.2: Relevant conformations of the single bonds in the isoprene dimer with their respective relative energies after the Hartree-Fock geometry optimization using the 6−31G basis-set (see text).

Conf.	Torsion 1 $C_2-C_3-C_5-C_1$	Torsion 2 $C_3-C_5-C_1-C_2$	Torsion 3 $C_5-C_1-C_2-C_3$	ΔE[kJ/mol]
1	180.0	180.0	180.0	42.56
2	−111.2	176.1	115.7	0.33
3	117.4	−62.9	133.5	2.87
4	115.3	−63.8	−124.0	2.28
5	−109.3	−177.7	−115.3	0.00
6	−94.9	−70.5	123.6	4.91
7	−86.0	−59.0	−108.3	6.72

Table 6.3: Relevant torsion conformations after geometry optimization using the hybrid method 6−311G**/B3LYP.

due to chemical rearrangement (ring formation), which would lead to overlap in the chains, where chemical changes are not allowed.

A subsequent *ab initio* Hartree-Fock calculation in a 6−31G basis set [DHP71] reduced the number of relevant states to 13. The other conformations rearranged to one of these during the geometry optimization. Thus, they are no stable minima. The interchange of all *gauche* states with their respective counterparts, i.e. flipping all torsions around the hypothetical *cis*-state, is a symmetry operation, as isoprene monomers have a symmetry plane. It is the plane defined by the double bonded carbons and the methyl carbon. This symmetry further reduced the number of unique conformations to seven (tab. 6.2). To obtain more accurate energy differences, more elaborate quantum-chemical methods were applied. First, geometry optimizations with a Hartree-Fock calculation using a 6−311G** basis set [MC80] were carried out. Afterwards, in a further refinement, a density functional calculation in the same basis set using the B3LYP (Becke's three-parameter hybrid functional using the LYP Correlation Functional [Bec93]) method was used, resulting in the data shown in table 6.3. The relevant minima exhibit *gauche* and *trans* states for the central torsion, whereas the two other occur only in the *skew* state, except for state 1 which is far above the others in energy.

Torsion 1	ΔE[kJ/mol]	ΔE[kJ/mol]
0	2.74	5.60
30	6.50	10.99
60	8.30	16.54
90	1.83	3.73
120	0.45	0.51
150	8.60	8.61
180	18.73	20.83
210	8.67	17.76
240	0.28	9.32
255		7.88
270	1.48	5.56
285		5.45
300	8.44	7.42
315		8.43
330	6.58	7.30
247.4	0.0	
117.3		0.0

Table 6.4: Quantum-chemically (HF/6−31G**) calculated energy barriers for torsion 1. Middle column torsion 2 in *trans* state, right column in *gauche* state

Barriers between torsional states

The torsion potentials are not only described by positions and relative energies of the minima, but for the dynamics the barrier heights are of equal importance. Therefore, a locally constrained optimization with one dihedral angle fixed was performed. In a first step, one starts with a modified optimized geometry, i.e. the torsional angle is fixed in a certain position. This position was changed in steps of 15 to 30 degrees. All other degrees of freedom were then optimized and the energy for every angle was recorded. These calculations were done in the Hartree-Fock approximation using the 6−31G** basis set which generates better results on barrier heights, whereas density functional calculations produce better results on the relative energies of minima [MP]. This is not inconsistent because the barriers are important for the dynamics, whereas the energy differences are needed for the chain conformational statistics.

Barrier calculation for torsion 1

The first investigation started with the energywise lowest configuration 5. Torsion 1 was fixed in the position to be investigated. The rest was taken from geometry 5. Only angles and dihedral angles were optimized. Bond lengths were fixed to save time and to be able to compare the results more directly. The relevant energies are shown in table 6.4 and figure 6.2. The zero-point of the energy was set to the minimal energy after full optimization in the same HF basis set. The torsion potential has three minima, whereby the *cis* minimum is higher than the others. A *trans* state is energetically extremely unfavorable, especially two *trans* states in neighboring torsions.

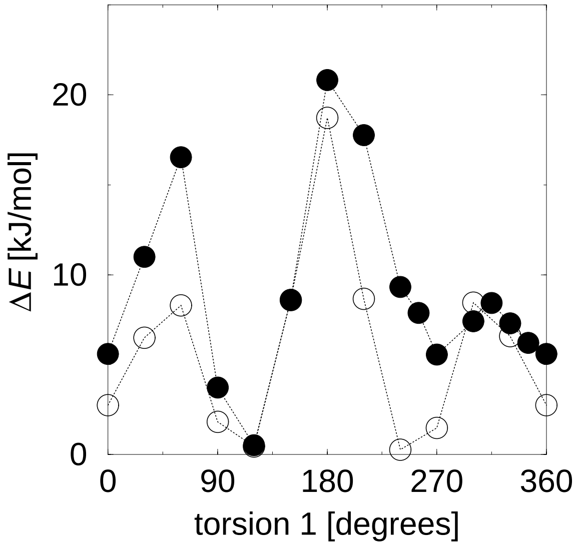

Figure 6.2: The energy barrier of torsion 1 depending on whether torsion 2 is in *trans* (open symbols) or *gauche* state (filled symbols).

The same procedure was repeated for torsion 2 in *gauche* position. The optimization was based on geometry 4, which has the lowest energy of the states with torsion 2 in *gauche*. These energies are shown shown in table 6.4 as well.

Barriers for torsions 2 and 3

With torsion 1 fixed in the *skew* state, torsion 2 was investigated starting again from configuration 5. This configuration shows three minima in the *trans* state and the two *gauche* states respectively. Then the second torsion was fixed in *trans* state, the third torsion was calculated. It differs from torsion 1 because of the additional methyl group. Minima are at the *skew* positions with a small barrier over *trans* and a much higher over *cis* (tab. 6.5 and fig. 6.3).

Optimization of the force-field against quantum chemistry

As the simulation package YASP [MP93] allows only cosine shaped torsion potentials, a non-linear fit to the quantum chemistry result was applied.[2] Interdependencies were neglected in the torsion potentials. They are, however, present as is seen in fig. 6.2 and are accounted for by the *intra*-molecular non-bonded interactions. For torsions 1 and 3 the first four terms (up to $\cos(3\tau)$) of the Fourier expansion were necessary

$$V = A_0 + A_1\Big[1 - \cos(\tau)\Big] + A_2\Big[1 - \cos(2\tau)\Big] + A_3\Big[1 - \cos(3\tau)\Big]. \tag{6.5}$$

Torsion 2 is simpler as it is reproduced well by only two cosines resulting in the force-field constants in table 6.6

$$V = 7.1\Big[1 - \cos\Big(3(\tau - 180°)\Big)\Big] + 4.9\Big[1 - \cos(\tau - 180°)\Big]. \tag{6.6}$$

Figure 6.3 shows the quantum chemical result in comparison to the fitted data.

---

[2] The fit was performed using the program XMGR [Tur97].

Dihedral	ΔE_2[kJ/mol]	ΔE_3[kJ/mol]
0	25.09	22.40
30	14.23	22.19
60	2.70	10.51
90	7.06	1.57
120	14.69	0.30
150	7.80	2.50
180	0.02	3.79
210	5.81	2.22
240	14.28	0.06
270	12.82	1.41
300	7.84	10.34
330	16.00	22.56
182.3	0.0	
244.8		0.0

Table 6.5: Relative torsion state energies for torsion 2 (middle column) and torsion 3 (right)

	Torsion 2 = 60°	Torsion 2 = 180°	Dihedral τ_0[°]	Barrier k_τ[kJ/mol]	Periodicity p
A_0^1[kJ/mol]	(5.67468)	(1.5339)			
A_1^1[kJ/mol]	2.83198	2.4393	0	5.2	1
A_2^1[kJ/mol]	−3.83546	−3.6502	0	−7.4	2
A_3^1[kJ/mol]	4.47921	5.5562	0	10.0	3
A_0^2[kJ/mol]	(10.9579)				
A_1^2[kJ/mol]	5.09897		180	9.7	1
A_3^2[kJ/mol]	7.30499		180	14.1	3
A_0^3[kJ/mol]	(24.8409)				
A_1^3[kJ/mol]	−10.5627		0	−21.1	1
A_2^3[kJ/mol]	−6.18701		0	−12.3	2
A_3^3[kJ/mol]	0.258146		0	0.5	3

Table 6.6: Fitted values for the Fourier expansion of force-field parameters. Numbers in brackets denote neglected additive constants, as they are only an overall shift of the energies. The notation of the force-field parameters A_p^t conforms to eq. (6.5), whereby the upper index denotes the torsion number. The parameter k_τ denotes the value used in the final potential. Note the factor of 2 occurring in the definition of the torsion potential $V = \sum_p {}^{k_\tau^p}/_2\{1 - \cos[p(\tau - \tau_0)]\}$.
Actually, torsion 2 was optimized “by hand” but the differences to the fitted values are negligible.

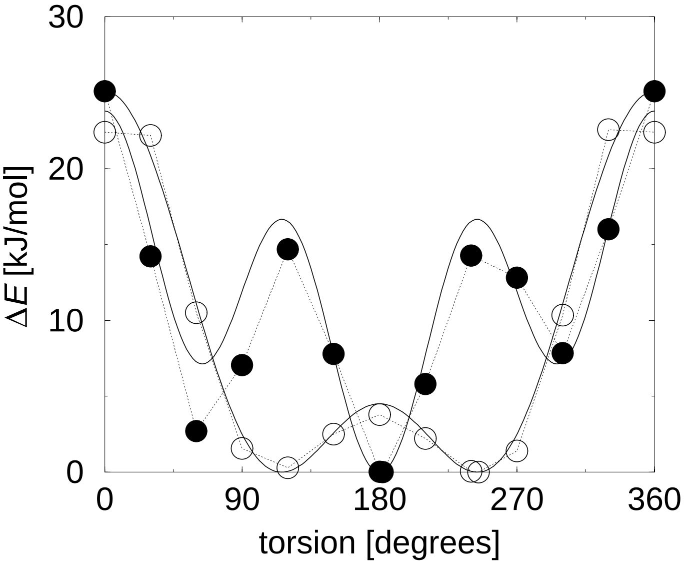

Figure 6.3: Comparison of QC calculated and fitted data for torsions 2 and 3. Differences are negligible for classical simulations. The circles are the quantum chemistry data (●: torsion 2, ○: torsion 3). The solid lines are the corresponding fitted potentials. The potentials used in the simulations differ by a shift (cmp. tab. 6.6).

6.2.2 Angle potentials and bond lengths

The potentials of atomistic angles serve the only purpose to keep the correct molecular shape without freezing the degrees of freedom completely. Therefore, only the average angle and not the exact value of the force constant are relevant for the purpose under study. For spectroscopic frequencies they would have to be adapted more carefully. The force constants were taken from former simulations of small molecules like cyclohexene [SFMP99]. The respective angles with their harmonic potentials are shown in table 6.7. The lengths of the atomistic bonds were constrained using the SHAKE algorithm [RCB77, MPB91] in order to allow for longer time-steps.

To maintain the double bond planar, a harmonic potential with a strength of 160 kJ/(mol rad^2) was applied to the following three dihedrals: $C_1{-}C_2{-}C_3{-}C_4$, $H_{C2}{-}C_2{-}C_3{-}C_5$, and $C_2{-}C_3{-}C_4{-}C_5$.

6.2.3 Non-bonded potential

The relevant parameters for the non-bonded interactions of the different atomic types were generated by optimizing a force-field for low-molecular-weight liquids against thermodynamic properties. To derive polyisoprene parameters, cyclohexene was used as model compound. These studies used a new method of force-field optimization [FSBMP99]. A similar approach was independently proposed by an Italian group [DG99]. Other automatic ways of force-field optimization are discussed in the literature as well, e.g. a Berendsen-like coupling [NvGMP95] or genetic algorithms [HH99].

Force-Field optimization by means of the simplex technique

In the process of optimization, the properties of the physical system are regarded as (unknown) functions of the simulation parameters. The root mean squared deviation from the experimental target values is, therefore, a single-valued function describing the “quality” of a force-field. This function was minimized using the simplex method for optimization in many dimensions. The main aspects of this method are briefly summarized in the following. Experimental values for density

Angle	$\phi_0[°]$	k[kJ/(mol rad^2)]	Bond	l_b[nm]
$C_1-C_2-C_3$	128.7	250	C_1-C_2	0.150
$C_2-C_3-C_4$	124.4	250	$C_2=C_3$	0.1338
$C_2-C_3-C_5$	120.2	250	C_3-C_4	0.151
$C_4-C_3-C_5$	115.4	250	C_3-C_5	0.1515
$C_3-C_5-C_1$	114.5	250	C_5-C_1	0.155
$C_5-C_1-C_2$	112.7	250	C−H	0.109
$C-C_{sp3}$-H	109.5	250		
C_1-C_2-H	114.4	250		
C_3-C_2-H	114.4	250		
H−C−H	109.5	250		

Table 6.7: Force-field for angles and bond lengths for the atomistic simulations. The equilibrium values were derived from Hartree-Fock calculations and experimental data.

and enthalpy of vaporization of cyclohexene at ambient conditions were taken as targets, which are to be reproduced by the model. From enthalpy of vaporization H_{vap} and system density ρ the single valued penalty function

$$f\Big(\{p_i\}\Big) = \sqrt{w_1\left(1 - \frac{H_{\mathrm{vap}}}{H_{\mathrm{vap}}^{(\mathrm{target})}}\right)^2 + w_2\left(1 - \frac{\rho}{\rho^{(\mathrm{target})}}\right)^2} \tag{6.7}$$

is calculated. The weights w_j allow to focus the effort on the more "difficult" property which typically is the enthalpy of vaporization. Of course, other experimental quantities may be used in the optimization as well. These, however, should converge rapidly in order to cut down necessary simulation time. This method can be applied as well for optimization against structural quantities like radial distribution functions [MBF$^+$00].

The geometry was fixed to the experimental bond lengths and angles obtained by microwave spectroscopy [Lid95]. Due to both sp^2 and sp^3 carbons being present in the molecule, three different atomic types were necessary. A six-dimensional optimization with all interaction strengths ϵ and all LJ radii σ would be too time consuming. Therefore, 4 non-bonded parameters were included in the optimization process, whereas the other non-bonded parameters were fixed. The latter are marked by an asterisk in table 6.8.

A major issue for a simulation is a careful equilibration. Normally, one checks "by eye" looking on different system properties whether the system is equilibrated and data collection can begin. This is obviously not possible in an automatic procedure. Therefore, an algorithm was devised to decide upon equilibration. Two different possibilities were chosen. The first was a linear regression of a time series of a system property - the density was used. Then the first and last values of the simulation were compared to their values in the linear regression. If they coincide within error, and if the slope of the regression is zero within error the system is deemed equilibrated. The second approach was to split the time series in pieces and calculate averages and standard errors of all of them. If the system is equilibrated, all the averages have to coincide within their errors. Both these approaches were tested against the "human eye" approach and found to be more restrictive. This is

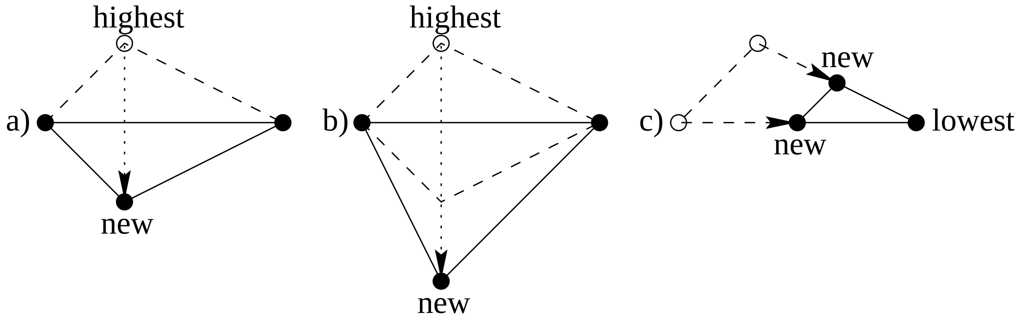

Figure 6.4: Illustration of the moves in the simplex optimization:
a) reflection, b) expansion, c) contraction around the best.

necessary as any badly converged f can mislead the optimization algorithm and cost unnecessary computer hours. During the optimizations both approaches were used.

A calculation of one penalty function value consists of the following steps: first, several equilibration runs follow each other until the test is passed, or the system cannot be equilibrated at all. Then a production run is performed to collect the data. With these data the penalty function f is calculated. The simplex algorithm, as described e.g. in ref. [PTVF92], minimizes single-valued functions in d dimensions. In the initial stage, $d+1$ points in d dimensional space are chosen in a way that any d of them are linearly independent. This set of points is called a *simplex*. The function f is evaluated at all these points. Now an iterative procedure starts. The simplex is *reflected* away from its worst point, i.e. the point with the highest function value. Reflection means that the worst point is reflected at the hyper-plane defined by the other points. The function value of the new point is evaluated. If it is better than the best point so far, a further expansion into this promising direction is applied. If it is worse than the second worst, a contraction towards the hyper-plane is performed. In any other case a new iteration with a reflection follows. If even the one dimensional contraction leads to a very bad point a contraction around the best point is applied, i.e. all points are moved in the direction of the best point. Thus, the simplex shrinks. If the algorithm expanded farther away from the hyper-plane the better of the two points is chosen. All these geometrical transformations of the simplex are illustrated in figure 6.4.

The power of force-fields developed by this method was demonstrated by the fact that although the optimization aimed only at simple thermodynamical observables of liquid cyclohexene, other properties as complex as mixture diffusion coefficients, reorientation times and the structure of a mixture with cyclohexane were reproduced satisfactorily for all available experimental data [SFMP99].

The so produced force-field was modified slightly for the polyisoprene simulations, as the density did not fully match the experimental density. However, it would not have been possible to do the optimization with the polymer because of limitation in the available CPU power. The final non-bonded parameters are shown in table 6.8.

Atom	m [amu]	σ [nm]	ϵ [kJ/mol]
C_{sp2}	12.01	0.321^*	0.313
C_{sp3}	12.01	0.311^*	0.313
H	1.00782	0.24^+	0.2189

Table 6.8: Non-bonded interaction parameters for the atoms in the polyisoprene simulations. The σ values of the carbons (asterisks) were fixed during the optimization. +: The σ of the hydrogens was slightly changed from the cyclohexene simulations.

6.3 Preparation of the melt

6.3.1 Starting configuration from quantum chemical torsion distributions

Since simulated times in atomistic simulations are very short (a few nano-seconds at the most), it is important to keep equilibration times as short as possible. One, therefore, wants to start close to an equilibrated structure. Since the torsion distribution is the most important prerequisite for the overall structure, special attention was paid to it.

The energy differences of the torsion states are known from the quantum chemical calculations. With these energies, a Boltzmann distribution of the torsions was generated for system 1, whereby always three torsions in a row were populated, i.e. the polymers were set up monomer by monomer. The three connecting torsions together were in one of the seven states calculated (tab. 6.3). The total energy of this set of torsions was known. A new monomer was now set up with a connection in one of these states with the according Boltzmann probability.

The bond angles were set up in the respective equilibrium values. The first simulations were performed at constant volume in a cubic box of edge length 9.0 nm and a very low soft core potential [MP93] of $V_{\mathrm{sc}}(r = 0) = 1.5$ kJ/mol using an extremely short time-step of 0.01 fs.[3] Step by step, the repulsion in the soft-core potential was increased until a simulation with the "true" Lennard-Jones potential (still with short time-step) was possible. Afterwards, the time-step could be increased in steps to 1 fs.

The simulation box was rescaled (compressed) several times and intermediately relaxed at constant volume. This procedure turned out to be more effective than starting at the under-dense conditions with constant pressure. After approaching the target density to about 90%, the simulations were changed to NpT with non-isotropic box-fluctuations to be better able to relax stresses in the different directions.

6.3.2 Application of end-bridging Monte Carlo

Systems 2 and 3 were set up after equilibration by an *end-bridging* Monte Carlo (EBMC) simulation (section 3.2.1) [KT95, MBZT99]. The end-bridging program is limited to a united atom description of the polymer chains which are pre-equilibrated like in subsection 6.3.1. The carbons

---

[3] The soft-core potential prevents instabilities in the initial stages of the simulation. It removes the divergence of the LJ potential at $r = 0$ by applying a spline to a finite value of $V(0) = V_{\mathrm{sc}}$. Thus, two atoms can overlap, although this is energetically unfavorable.

Interaction	σ[nm]	ϵ[kJ/mol]
C−C, C−CH, CH−CH	0.38	0.4186
$C-CH_2$, $CH-CH_2$	0.4257	0.4249
$C-CH_3$, $CH-CH_3$	0.4257	0.6299
CH_2-CH_2	0.45	0.3918
CH_2-CH_3	0.45	0.6095
CH_3-CH_3	0.45	0.9479

Table 6.9: Nonbonded parameters used in the united atom end-bridging Monte Carlo simulations of *trans*-polyisoprene. Bond lengths, angles and torsion potentials are the same as in the all atom simulations [Dox]. All the interactions within a topological distance of up to 3 bonds are excluded as they are taken into account in the torsion potentials.

move	rate[%]
rotation	0.8
CB-reptation	0.6
intrabridge	0.003
end-bridge	0.09
volume fluctuation	35.3

Table 6.10: Acceptance rates for the different moves in the end-bridging Monte Carlo calculations. The intrachain bridge move is ineffective due to the short chains. For end-bridging and intra-bridging the efficiency increases with chain length at overall constant number of interaction sites [MBZT99].

were taken as interaction centers for the end-bridging MC. The hydrogens were reintroduced into their resting positions after the end of EBMC. In order to keep the subsequent MD simulation stable the overlaps resulting from this reintroduction were removed by a short soft-core simulation with very short time steps.

As end-bridging leads to polydispersity, the chains in these simulations only had on average the same molecular weight as the monodisperse system (682 g/mol, 10mers). Oligomers between 5 and 15 monomers were found in the system. Two independent starting configurations with different chain mixtures were used as starting points for the atomistic MD simulations (fig. 6.5).

The values of the simulation parameters are shown in table 6.9. The angles and bond lengths between the atoms were fixed in the end-bridging procedure for sake of speed, as only the global structure is to be relaxed. In about six weeks of computer time on a DEC Alpha processor with 433 MHz, a melt of 100 chains with an average length of 10 monomers could be brought near equilibrium. About every second chain had changed length by then. The acceptance rates of the different moves are shown in table 6.10. On average, every chain experienced 2.81 successful end-bridging moves during this time, which shows that a reasonable amount of moves was performed.

The non-bonded interactions were not changed from the *cis*-polyisoprene simulations. The density was about 20% too low after the simulation due to a problem in the calculation in the potential energy during the volume changing move [Dox]. This is not a problem, as the subsequent atomistic MD was equilibrated close to the experimentally correct density (about 2% deviation from experiment) before data recording started. It was not the task to use the Monte Carlo procedure to simulate polyisoprene. The method was only employed to produce possibly independent starting configurations for the atomistic simulations.

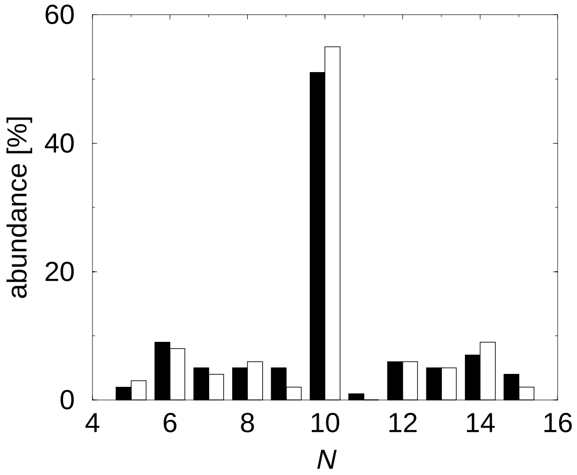

Figure 6.5: Chain length distributions of the polydisperse systems 2 (filled bars) and 3 (open bars) in monomer numbers.

6.4 Thermodynamic observables

The two systems simulated under constant pressure conditions arrived at densities of $\rho_{sys2} = 917.4\ \mathrm{kg/m^3}$ and $\rho_{sys3} = 916.8\ \mathrm{kg/m^3}$, corresponding to a discrepancy to the experimental value of less than 2%. These are the two systems pre-equilibrated by end-bridging Monte Carlo. Experimentally heptamers of polyisoprene have a density $\rho_{7\mathrm{mer}} = 900\ \mathrm{kg/m^3}$ and hexadecamers $\rho_{16\mathrm{mer}} = 899\ \mathrm{kg/m^3}$. The density drops slightly with increasing chain length at least up to 34 monomers [FLG99].

The constant volume simulation at $890\ \mathrm{kg/m^3}$ of system 1 had an average pressure of $p = -5000$ hPa which means that it would like to contract. It had, however, huge fluctuations with a standard deviation of 9000 hPa. All densities were close to the experimental value, which has some uncertainty as well. It was determined for a mixture of *cis*- and *trans*-polyisoprene. Thus, a closer refinement of the non-bonded parameters was deemed unnecessary. The density also depends weakly on the intrachain part of the potential. When the torsion potentials were switched off, the density increased by about 2% because the chains can pack more effectively. At a higher temperature of 413 K, the simulation density was $\rho_{413\,\mathrm{K}} = 826\ \mathrm{kg/m^3}$ in comparison to the experimental value of $\rho^{\mathrm{exp}}_{413\,\mathrm{K}} = 836\ \mathrm{kg/m^3}$ for long chains [BI75], which shows that the thermal expansion coefficient α was reproduced reasonably well ($\alpha_{\mathrm{sim}} = 0.92 \cdot 10^{-3}\ \mathrm{K^{-1}}$ vs. $\alpha_{\mathrm{exp}} = 0.65 \cdot 10^{-3}\ \mathrm{K^{-1}}$).

6.5 Conformations of the chains

The mean-squared end-to-end distance of polyisoprene was measured between the terminal carbons for the different systems. The respective result for 300 K, 5.94 $\mathrm{nm^2}$, corresponds to a value of 0.0087 $\mathrm{nm^2mol/g}$ for the monomer-weight-specific end-to-end distance. This is closer to polybutadiene or hydrogenated polyisoprene (both 0.0088 $\mathrm{nm^2mol/g}$) than to polyisoprene with 0.0060 $\mathrm{nm^2mol/g}$. The experimental values are determined by Small angle neutron scattering for a mixture of *trans* and *cis* polyisoprene chains [FLR$^+$94, FLG99]. The discrepancy to experiment may arise from finite chain length effects.

The average of the end-to-end distance itself arrived at 2.23 nm, which is less than half a box

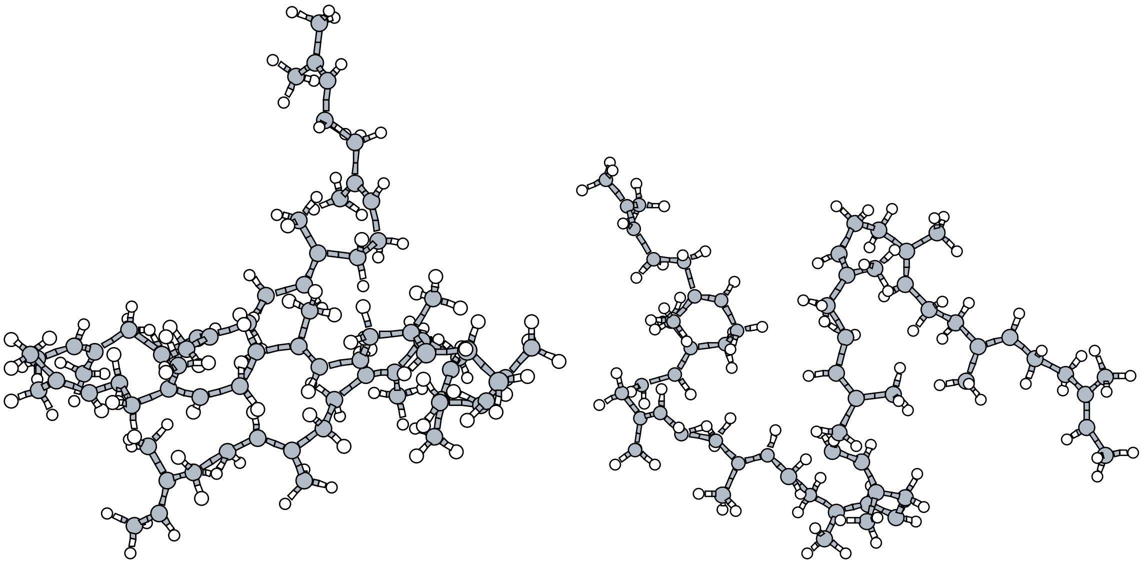

Figure 6.6: Two example conformations of atomistic chains encountered in the simulation. The left hand side shows a 14mer, the right hand side a 12mer. Both are contained in system 3. The chain on the left hand side is a kind of a helix, whereas the right hand picture shows a chain which is locally extended and then folded. The monomers themselves are always stiff and planar. Only the connections between the monomers lead to the different conformations.

length. Thus, self-interactions are effectively avoided. For 413 K the results were 2.44 nm for the mean distance and 6.92 nm^2 for the mean-squared distance.

Experimentally, the local stretching ratio C_∞ was measured by intrinsic viscosity and light scattering measurements in Θ-solution [HZF82]. The results are $C_\infty^{\mathrm{light}} = 5.2$ and $C_\infty^{\mathrm{visco}} = 5.1$. The C_∞ in an atomistic model cannot be as easily defined as in a bead-spring model but a Kuhn length can be calculated. The most stretched configuration of polyisoprene is the all-*trans*-state with a distance between the two terminating carbons of 4.827 nm for a decamer, which is about the edge length of the box (4.80 nm × 5.16 nm × 4.98 nm). With the average length this value leads to a Kuhn segment length $l_\mathrm{K} = 1.06$ nm. The stretching $C_{10} \approx 3.3$ could only be estimated as the bond length is not well defined on this scale. Here the length per monomer in the all-*trans* configuration was chosen. As seen above by the monomer-weight-specific end-to-end distance, the short polyisoprene chains are experimentally even more compact ($C_7 \approx 2.05$). Therefore, the static chain conformations are acceptable. In figure 6.6 example conformations taken from simulations are shown.

6.5.1 Persistence length

The persistence length l_p was calculated using tangent vectors $\vec{u}$ along the backbone (fig. 6.7). The function $\langle \vec{u}(n)\vec{u}(m) \rangle$ with $\vec{u}(n)$ the tangent vector at monomer n denoting the monomer index was fitted by the exponential $\exp[-{}^{|n-m|}/_{l_\mathrm{p}}]$. There is some freedom of how to define the tangent vector in an atomistic model. The vectors connecting the C_1 (or the C_2) atoms between different monomers were investigated. Additionally, intra-monomer vectors along the double-bond and vectors connecting the two end carbons of the monomer ($\mathrm{C}_1 - \mathrm{C}_5$) are included. The bond-correlation functions are not really exponential (fig. 6.7), as the interactions are complex and the chains are only short. Thus, persistence lengths deduced from the fitting procedure can only to be taken as

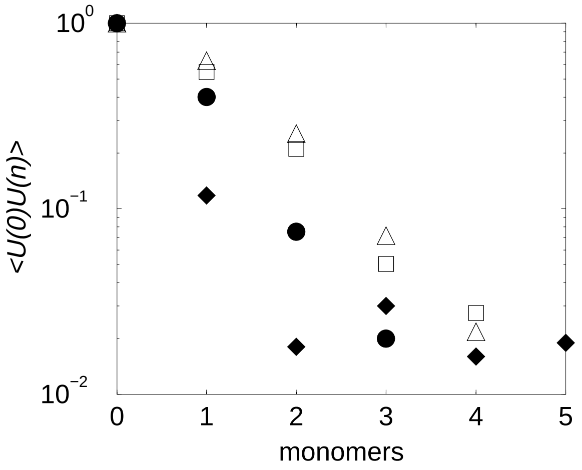

Figure 6.7: Bond correlation functions for the atomistic polyisoprene simulations of system 1. The filled symbols are correlations between direction vectors in the monomers. (diamond: double-bonds, circle $C_1 - C_5$) The open symbols correspond to vectors connecting neighboring monomers (squares: C_2, triangles C_1).

estimates. End-effects were not excluded here for reasons of statistics. The correlation functions of the respective vectors are different. The vector connecting to the shortest distance (the double-bond) has the shortest correlation length. The persistence lengths differ between 0.5 monomers (for the double bonds) and 1.5 monomers (for the intermonomer vectors). Polyisoprene is therefore rather flexible on the length scale of a few monomers. The monomer itself is intrinsically stiff, but the three torsions between neighboring monomers provide a flexible link.

The Kuhn length was estimated above to be $l_K \approx 1$ nm. As the persistence length is in the case of a long chain with only short-range correlations half a Kuhn length one can estimate a monomer size of 0.5 nm. This is again consistent with the length of the all-*trans*-chain above.

6.5.2 Distribution of torsions

The torsion distribution of the atomistic chains at 300 K does not differ strongly between the systems (fig. 6.8). Torsions 1 to 3 within one system, however, are remarkably different. The central torsion 2 is similar to a *standard* torsion distribution. There are three maxima, the most highly populated state is the *trans* state. The two *gauche* states are much less populated. This is expected for a single bond torsion along a chain.

The two other dihedrals, however, are different. They both occur mostly in the *skew* state and weakly in *cis*. The difference in torsion 3 between the systems comes from the C−H and H−H interactions which are excluded for system 1. So the *trans* state is accessible as transition state in system 1, whereas in system 3 the methylene hydrogens at C_1 and the methyl side group repel each other. In torsion 1 the population at *cis* is more pronounced if the hydrogen interactions between the methyl group and the methylene at C_1 from the preceding monomer are suppressed. This shows that caution has to be taken in the analysis of torsion populations, as only slight differences in the force-field have important consequences.

In the dynamics it will be shown, however, that the transition rates leading to reorientation of the C−H vectors are for both cases comparable to experimental data (sec. 6.7).

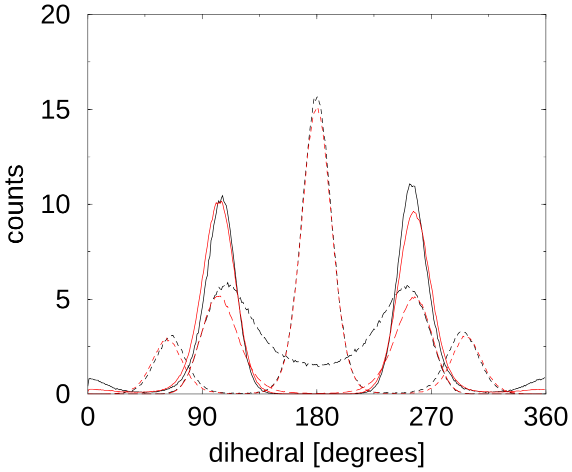

Figure 6.8: Torsion distributions of the atomistic simulations. System 1 (black) and system 3 (red) are shown. The solid curves correspond to torsion 1, the dotted to torsion 2 and the dashed to torsion 3. The absolute amplitudes are meaningless.

6.6 Melt structure

6.6.1 Radial distribution functions and local molar fractions

One important characteristic of the local structure in the melt are the different pair distribution functions. Figure 6.9 shows radial distribution functions of all atomic species. The curves between the different systems differ only slightly due to the different densities. Only the inter-chain part is shown. There is a low value at short distances, as chains cannot easily interpenetrate. There is very little structure in the all-atom $g(r)$, which is in contrast to e.g. the C$-$C distribution function with its clear peaks.

Figure 6.10 shows the center of mass distribution of the whole chains. They can approach as close as 0.2 nm. There is no real equidistribution, as the centers of masses did not move very much in the simulated time (see sec. 7.1). But on distances of more than 1 nm the distribution is quite flat.

Carbon-carbon radial distribution functions resolved according to carbon type allow to look for preferential arrangements between different chains. Partial pair distribution functions between the five different carbons present in polyisoprene were recorded (fig. 6.11). The methyl carbon (C_4) is the most exposed and can, therefore, approach closest to the others ($\approx$ 0.4 nm). At this closest distance there is also a shoulder in the C_1, C_2 and C_5-RDF indicating direct contact. C_3 is the most “shielded” carbon. However, it shows with C_1 a very slight shoulder at direct contact. Since C_3 is connected to C_2, C_4 and C_5, it is often found as second contact ($\approx$ 0.55 nm), as it is drawn with them. The two methylene carbons C_1 and C_5 are coordinated very similarly. C_2 shows the weakest structure. It is easily accessible, as it has only one hydrogen connected but is rather immobile, as it is on the double bond in the backbone.

Integration of the pair distribution function yields the number of neighbors of an atom in a shell. These numbers are shown in table 6.11 in shells inspired by figure 6.11. The shell boundaries apply to almost all curves in the figure as they resolve different regions. By relating the local number density $\rho_{\text{local}} = \frac{\#\text{C}}{V}$, $\#$C being the number of carbons, to the overall concentration $\rho(\infty) = 8.102\ \text{nm}^{-3}$ local enrichment ($x > 1$) and depletion ($x < 1$) of the respective carbon type is found in the neighborhoods. The results confirm the findings from the RDFs: in the closest shell ($r < 0.45$ nm) of all carbons methyl groups (C_4) are enriched, sp^2 carbons (C_2 and especially

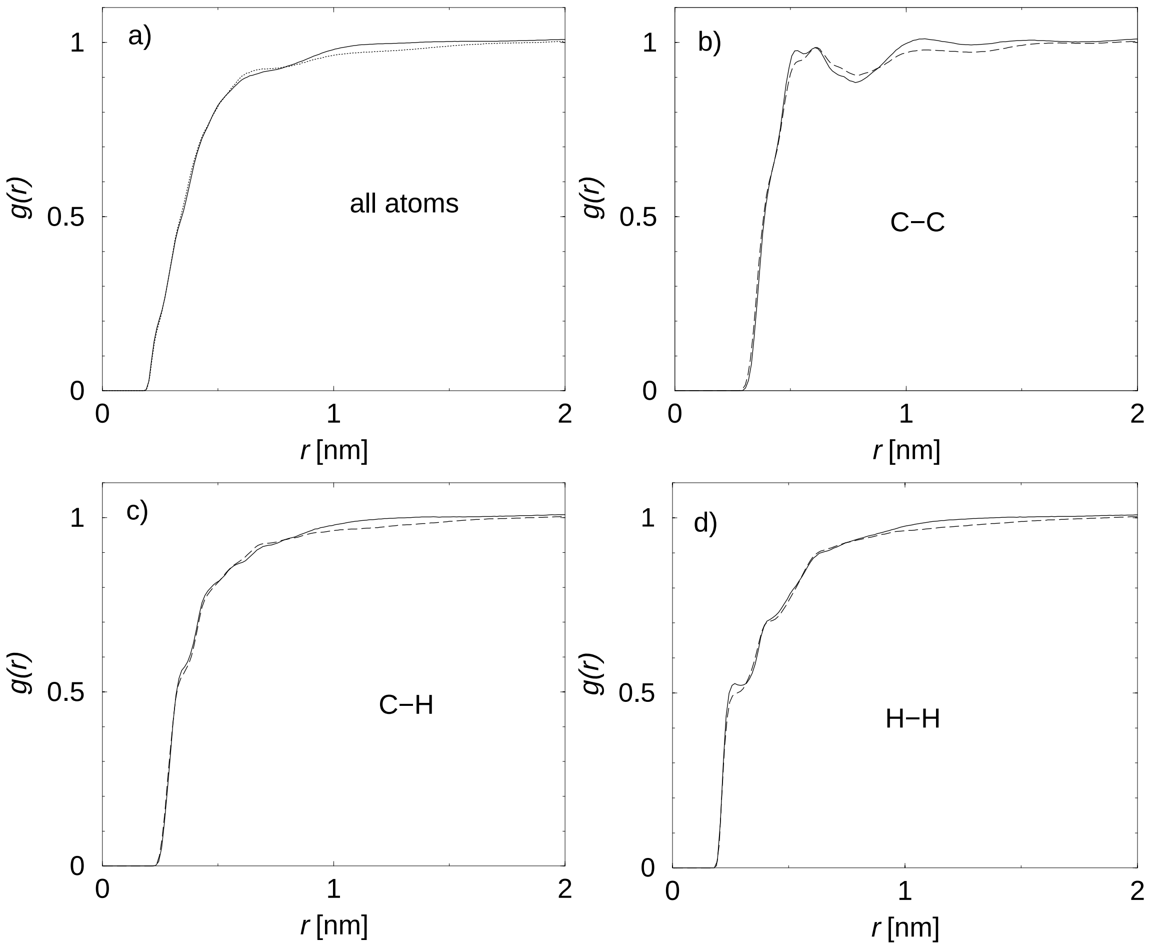

Figure 6.9: Interchain radial distributions of the different atom-pair-types. The solid lines are the mono-disperse system 1, the dashed lines system 2. a) All atoms. b) All carbons. c) All hydrogens. d) All carbon hydrogen pairs. The specific carbon-carbon distribution resolved according to the position in the monomer is shown in fig. 6.11.

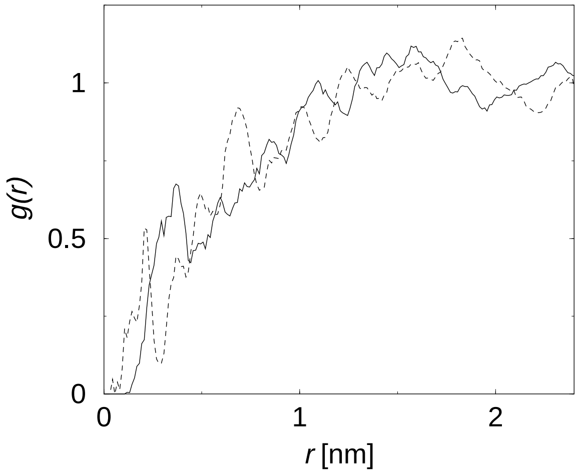

Figure 6.10: Center of mass radial distribution function of the atomistic polyisoprene chains. A correlation hole on local scales is seen, on bigger length scales the distribution is nicely flat. The solid line corresponds to system 2, the dashed line to system 3.

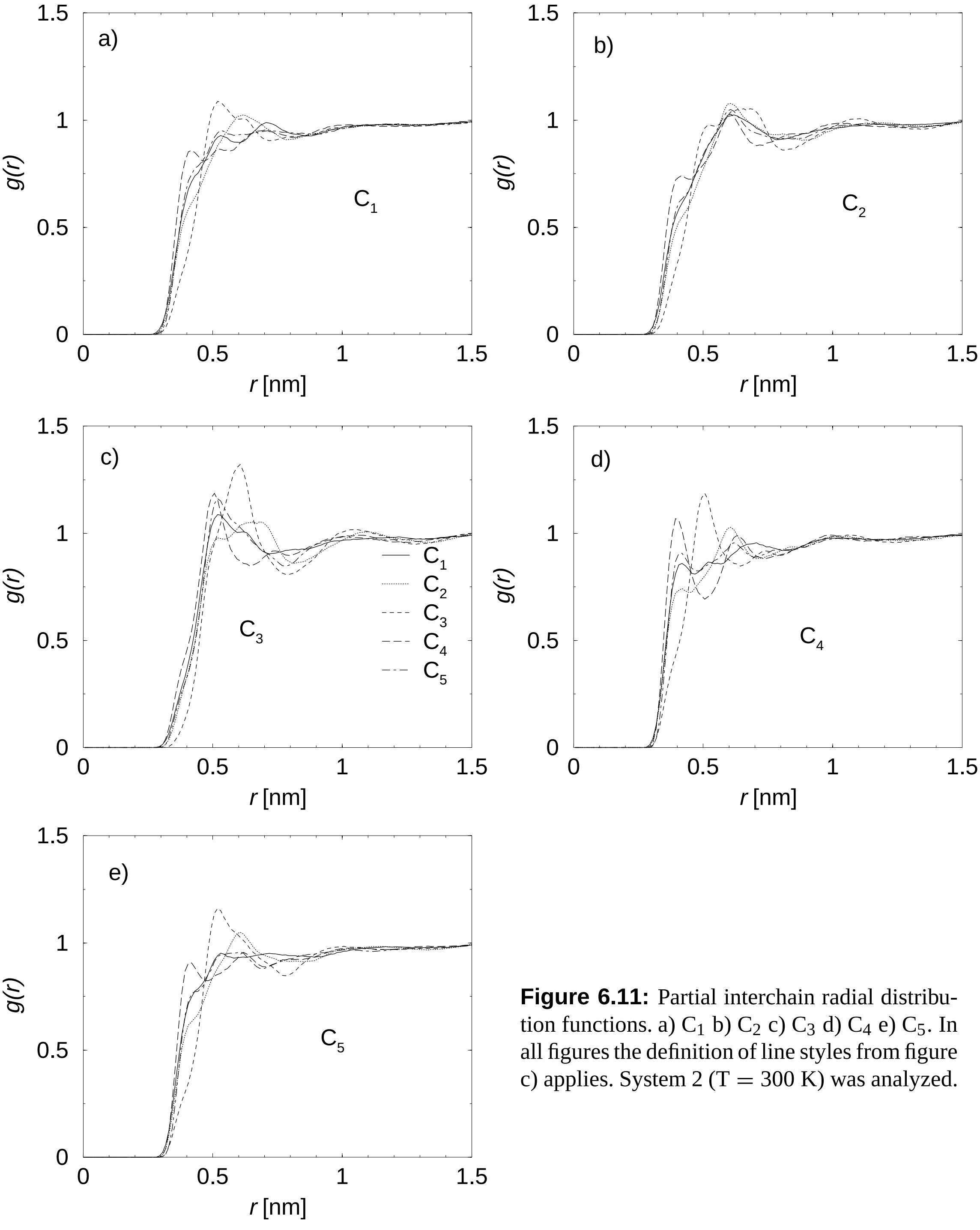

Figure 6.11: Partial interchain radial distribution functions. a) C_1 b) C_2 c) C_3 d) C_4 e) C_5. In all figures the definition of line styles from figure c) applies. System 2 (T = 300 K) was analyzed.

$C_a - C_b$	$\frac{x(r<0.45\ \text{nm})}{x(\infty)}$	$\frac{x(0.45\ \text{nm}<r<0.57\ \text{nm})}{x(\infty)}$	$\frac{x(0.57\ \text{nm}<r<0.65\ \text{nm})}{x(\infty)}$	$\frac{x(0.65\ \text{nm}<r<0.8\ \text{nm})}{x(\infty)}$
$C_1 - C_1$	1.05	0.98	0.96	1.02
$C_1 - C_2$	0.92	0.96	1.06	1.00
$C_1 - C_3$	0.71	1.13	1.05	0.98
$C_1 - C_4$	1.25	0.93	0.95	1.00
$C_1 - C_5$	1.07	1.00	0.98	1.00
$C_2 - C_1$	1.09	0.99	0.99	1.00
$C_2 - C_2$	0.95	0.95	1.03	1.02
$C_2 - C_3$	0.57	1.13	1.01	1.02
$C_2 - C_4$	1.31	0.95	0.97	0.96
$C_2 - C_5$	1.08	0.99	1.00	0.99
$C_3 - C_1$	1.15	1.00	0.97	1.00
$C_3 - C_2$	0.78	0.97	1.01	1.04
$C_3 - C_3$	0.64	0.98	1.20	0.94
$C_3 - C_4$	1.39	1.03	0.84	0.98
$C_3 - C_5$	1.03	1.03	0.98	1.04
$C_4 - C_1$	1.05	0.97	0.98	1.03
$C_4 - C_2$	0.93	0.97	1.07	0.99
$C_4 - C_3$	0.72	1.22	0.93	0.99
$C_4 - C_4$	1.24	0.85	1.02	0.99
$C_4 - C_5$	1.06	0.99	1.01	1.00
$C_5 - C_1$	1.09	0.98	0.95	1.02
$C_5 - C_2$	0.93	0.95	1.06	1.00
$C_5 - C_3$	0.65	1.16	1.04	1.03
$C_5 - C_4$	1.29	0.92	0.97	0.98
$C_5 - C_5$	1.04	0.98	0.97	0.98

Table 6.11: Local molar fractions (of system 2, T = 300 K) normalized to the overall concentration of atom *b* from foreign chains surrounding atom *a* by integration of the pair distribution function.

C_3) are depleted, whereas the methylenes (C_1 and C_5) are close to bulk average concentration. In the second shell, this is partly reversed, as C_3 is enriched and C_4 is weakly depleted. At distances larger than 0.65 nm all species are found at bulk concentration.

All in all one can say, that the methylene carbons occur at the same density almost everywhere. The methyl and the double bond carbons (esp. C_3) show much more structure. Monomers of different chains, thus, approach each other typically with their side groups as closest contact. Orientational influences from the double-bond, which keeps the monomer planar, play a role, too (below). The whole overall structure in the RDFs extends about two monomer sizes ($r < 1$ nm), whereas the concentrations of different carbons levels out to the same values already at 0.65 nm. The center-of-mass RDF shows that there is additionally a correlation hole (fig. 6.10).

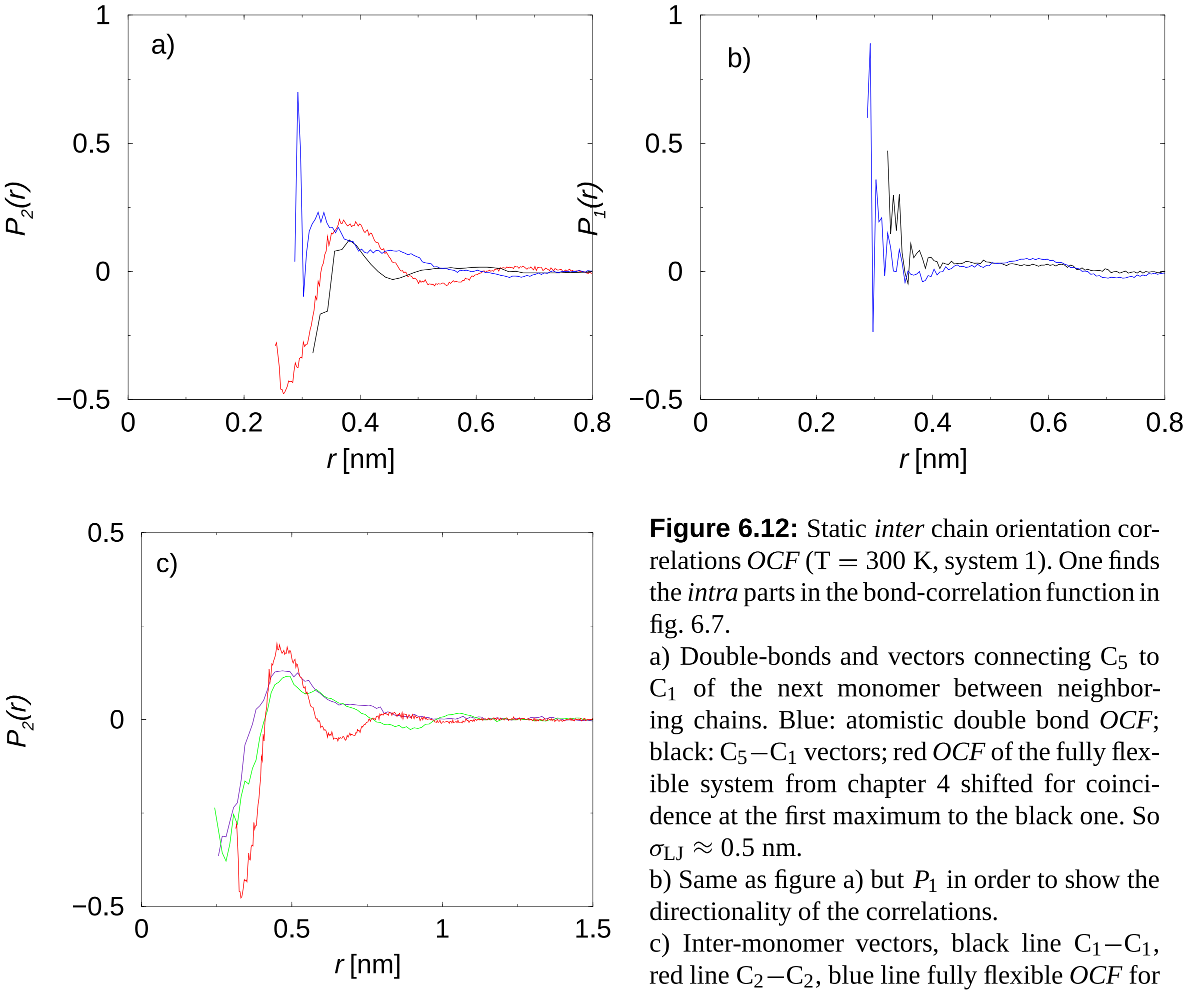

Figure 6.12: Static *inter* chain orientation correlations *OCF* (T = 300 K, system 1). One finds the *intra* parts in the bond-correlation function in fig. 6.7.
a) Double-bonds and vectors connecting C_5 to C_1 of the next monomer between neighboring chains. Blue: atomistic double bond *OCF*; black: C_5-C_1 vectors; red *OCF* of the fully flexible system from chapter 4 shifted for coincidence at the first maximum to the black one. So $\sigma_{LJ} \approx 0.5$ nm.
b) Same as figure a) but P_1 in order to show the directionality of the correlations.
c) Inter-monomer vectors, black line C_1-C_1, red line C_2-C_2, blue line fully flexible *OCF* for comparison. Note the changed ordinate scale.

6.6.2 Static orientation correlations

The local structure is not fully described by the (spherically averaged) radial distribution functions. Mutual orientation of chain segments is important as well (fig. 6.12). It was measured by the orientation correlation function *OCF* introduced in section 4.2

$$OCF(r) = P_2(r) = \frac{1}{2}\left[3(\vec{u}_i u_j)^2 - 1\right] . \tag{6.8}$$

As in the definition of the persistence length, there are several possible choices for the tangent vectors $\vec{u}_i$. Orientation correlations of the vector connecting the methylenes (C_1-C_5) extend over several interatomic distances (fig. 6.12a). They resemble the packing of coarse-grained chains. At small distances, a perpendicular orientation is found. Then a parallel ordering peak is encountered at about 0.4 nm. The first Legendre polynomial ($(\vec{u}_i\vec{u}_j)$, fig. 6.12b) shows that these interchain contacts have a preference to be parallel, the two neighboring chains run along each other. At larger distances the explicit atomistic structure is no longer important. But there are still structural effects originating from the packing visible up to about 0.7 nm, about two chain diameters.

The order of the double bonds between the chains exhibits more atomistic details. As the double bonds with the sp^2-carbons lead to a planar configuration of the environment, there is more parallel orientation. The parallel alignment of the neighbors especially at short distances ($r \lesssim 0.4$ nm) is again visible in the first Legendre polynomial. The high peak at $r \approx 0.28$ nm is not sound as there is only weak statistics.

The inter-monomer vectors (fig. 6.12c) in contrast, display even more generic features already seen in the bead-spring model. As they describe segments of larger size compared to the intramonomer vectors discussed above, the features are less accentuated (note the smaller ordinate in fig. 6.12c). On close contact an almost perfect perpendicular order is found. At intermediate distances a preferred parallel alignment, and for the case of the C_2-C_2 vector the next perpendicular region shows up. The differences between the two different intermonomer vectors are weak. So for orientations on length scales as small as monomer sizes, the bead-spring models already provide a useful description. Recall, however, that both the coarse-grained model (sec. 4.1) and the atomistic polyisoprene model (sec. 6.5.1) have similar persistence lengths of about $1-1.5$ monomer diameters. It remains to be seen, whether coarse-grained models can capture the packing of stiffer polymers, as well (sec. 7.1).

This shows that the generic packing effects discussed in sec. 4.2 are important for the understanding of the structure of atomistic models. However, the fine structure at short distances, as found in the first Legendre polynomial, cannot be explained by generic arguments as here the detailed chemistry of the polymer is important.

6.6.3 Melt structure function

Radial distribution functions give an illustrative picture. However, the observables in scattering experiments are structure functions. The static melt structure factor

$$S_{\mathrm{melt}} = \frac{1}{N}\left\langle \left| \sum_{m=1}^{N_{\mathrm{C}}} \sum_{j=1}^{N} \exp(ikr_j^m) \right|^2 \right\rangle . \tag{6.9}$$

is shown in figure 6.13 in comparison to simulations of *cis*-polyisoprene and experiments on a mixture dominated by the *cis*-conformer. The melt structure factor shows a clear peak at about 15 nm^{-1}. In addition, there is some smaller structure. The lower limit of resolution is set by the size of the box, which is about 5 nm in every direction corresponding to a minimum $|\vec{k}|$-vector of about 0.4π nm^{-1}. At higher temperature the overall structure flattens out with less pronounced peaks as expected.

Moe and Ediger performed simulations on pure *cis*-polyisoprene at 363 K and 413 K. The densities were much lower than the experimental values (798 vs. 869 and 775 vs. 836 $\mathrm{kg/m}^3$ respectively). Their system contained only one chain of 100 monomers [ME96, ME99]. This, obviously, reduces the influence of end effects. The structure functions of both simulations are, however, comparable at 413 K. Neither simulations compare really satisfactorily to the experimental structure factor. The double-maximum structure of the first peak is not reproduced, the lower maximum (≈ 13 nm^{-1}) being enhanced, the higher (≈ 18 nm^{-1}) being reduced to a shoulder. The positions of the peaks, however, are in reasonable agreement. This also applies to the second peak slightly below 30 nm^{-1}. As the experimental temperature is not given, one cannot say whether the discrepancy is a low temperature effect indicating the formation of a glass. Both simulations are performed deep in the melt. Another reason for the disagreement could be the fact that the short chains presented are still oligomers. The alternative would be one long chain as in [ME96, ME99]. However, due to the periodic boundary replication one chain can only interact

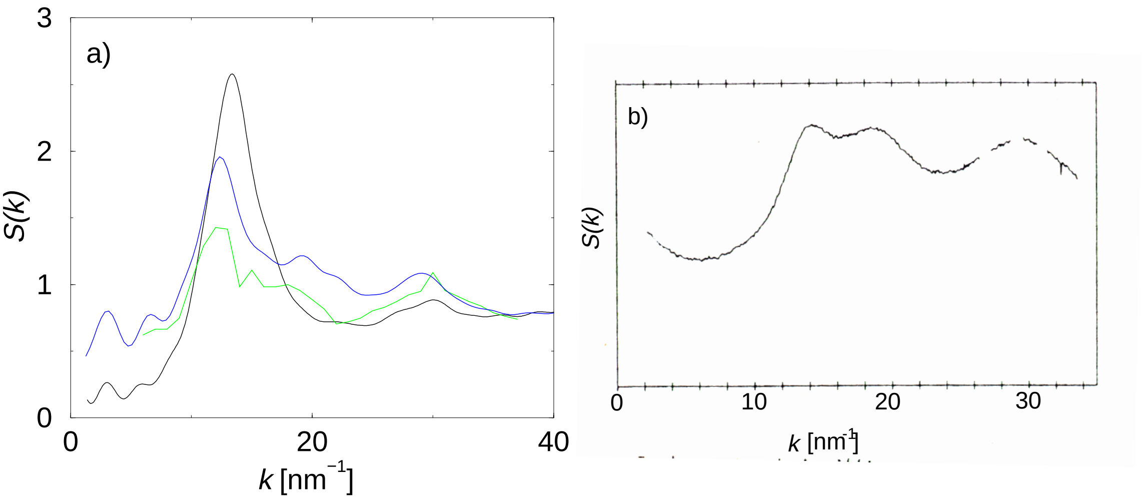

Figure 6.13: Static melt structure function of a) *trans* polyisoprene from this work (300 K, system 2: black, 413 K: blue), the scattering lengths of all atoms are taken to be the same in comparison to the *cis*-conformer (413 K: green, simulation data from ref. [ME99]) and b) experiment. The experiment was performed on a mixture of (76:18:6) *trans*:*cis*:*vinyl* polyisoprene. The experimental temperature is not given, and the amplitude of the experiments is in arbitrary units [ZRF$^+$92].

with itself, which is a questionable ansatz. It is not yet possible to fully equilibrate melts of true atomistic polymers of sufficient length.

There are positronium annihilation experiments of polyisoprene [DFA98]. The atomistic simulations were additionally investigated according to their free volume in comparison and come to reasonable agreement [SMPF00].

6.7 Dynamics of atomistic polyisoprene oligomers

6.7.1 Reorientation

The reorientation behavior of simulation models may be investigated by means of the auto-correlation function of Legendre polynomials of direction vectors. Due to the connection to NMR the second Legendre polynomial was chosen [Sli90, SRS94] (compare sec. 2.5)

$$C_{\mathrm{reor}}(t) = \left\langle P_2\left[\vec{u}(t)\vec{u}(0)\right]\right\rangle . \tag{6.10}$$

End-to-end vector

Figure 6.14 shows for the two polydisperse systems the reorientation correlation function (first and second Legendre polynomial) of the end-to-end vector, which is defined as the vector connecting the two terminating carbons $C_1^{\mathrm{mono}\,1}$ and $C_5^{\mathrm{mono}\,n}$. The relaxation time is clearly longer than the time accessible in the simulations. Even system 2, which was simulated for more than 2 ns, did not relax completely on this time scale; local vectors of course are much faster. At the higher temperature of 413 K the relaxation speed increases drastically. Still, one has to be cautious discussing length scales of more than a monomer. This figure shows that there is some scatter between the two

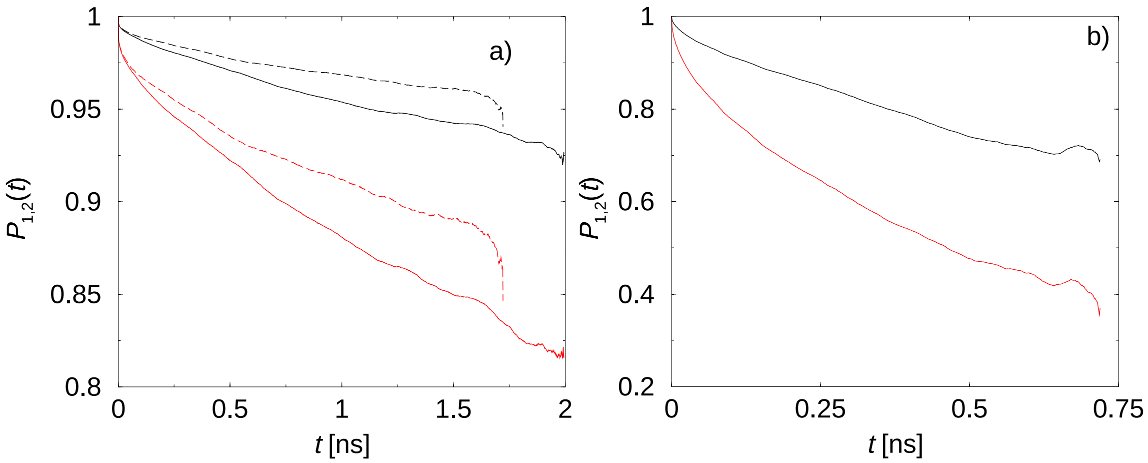

Figure 6.14: Relaxation of the end-to-end vector. Black curves are first Legendre polynomials, red curves second Legendre polynomials.
a) T = 300 K: of both pairs, the upper curve is the correlation function for system 3 and the lower one for system 2.
b) For T = 413 K (system 3b) the relaxation times are much shorter.

systems. This may be taken as a rough estimate of the error of the simulations.

Longer simulations were prohibited by the demand of computing power; besides, it was not the goal of these simulations to look at the overall properties. For that purpose bead-spring simulations, as presented in the preceding chapters, are more appropriate.

Backbone C=C vectors

The reorientation of local segments can be illustrated with the double-bonds in the chain. As seen in figure 6.15a, the reorientation depends on the position along the chain. The ends reorient much faster than the inner monomers. The 6 innermost monomers are comparable. So chains of length 10 have already a “bulk” part, although they are still oligomers. The difference between the two ends is easily explained, as on the one end (monomer 1) only one methyl group has to be moved, whereas on the other end (monomer 10) there are two methyl groups, the terminating methyl and the methyl side group.

There is a two step process seen in the reorientation. On very short time scales a fast drop is observed relating to bond angle vibrations which occur on a time scale of less than 1 ps. This is not resolved here. As the bond lengths are fixed, they cannot contribute to the reorientation. Then for the inner monomers a long-time process sets in. Its decay is on the order of the reorientation of the whole chain.

There is little difference in the dynamics of chains of different lengths, at least in the limited range under study here: the end monomers are free to move regardless of the rest of the chain (fig. 6.15b) and, for central monomers, the relaxation is the same within the (large) statistical error (fig. 6.15c). As seen in fig. 6.5, except for length 10 there are very few chains.

C-H vectors - Comparison to experiments and simulations on *cis*-PI

Experimentally the reorientation of vectors connecting carbons and hydrogens can be measured by NMR (section 2.5). To study specific vectors, carbons and/or hydrogens can be selectively

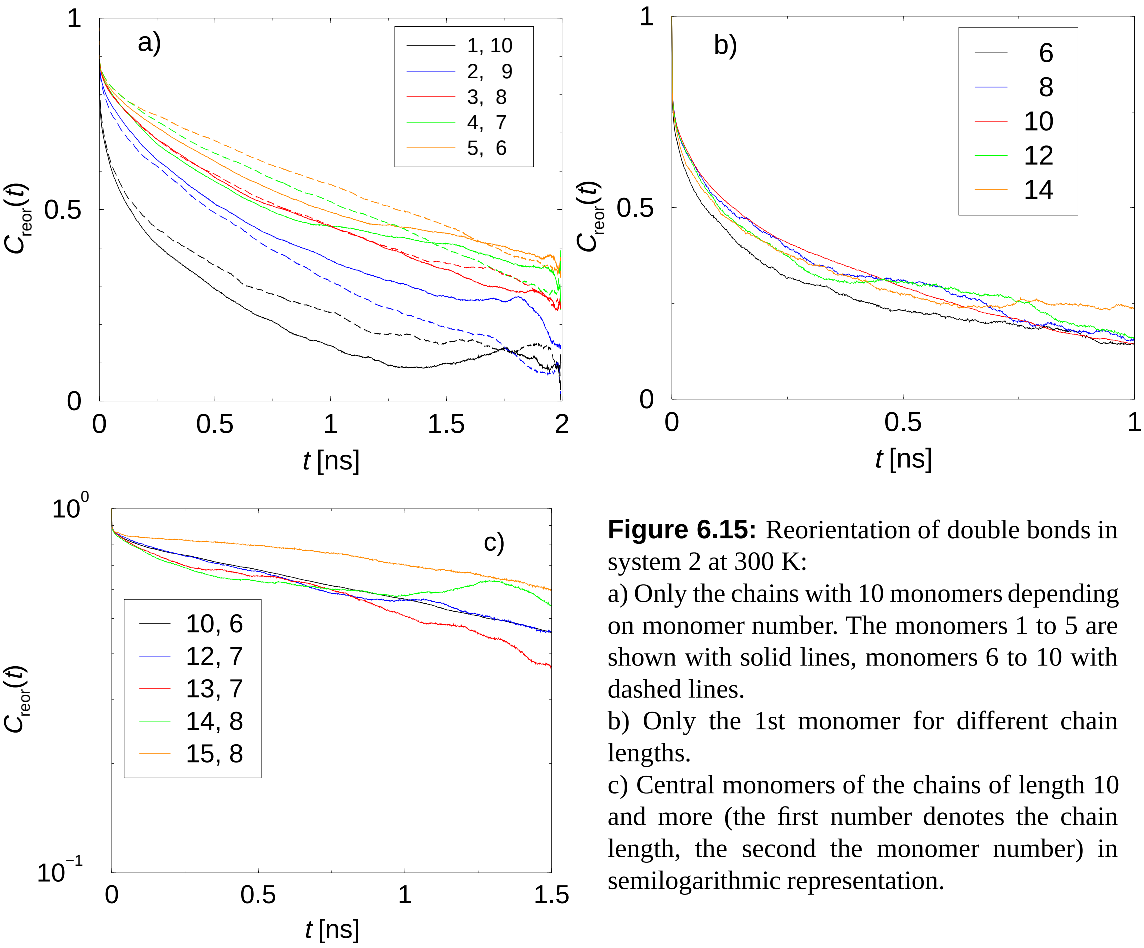

Figure 6.15: Reorientation of double bonds in system 2 at 300 K:

a) Only the chains with 10 monomers depending on monomer number. The monomers 1 to 5 are shown with solid lines, monomers 6 to 10 with dashed lines.

b) Only the 1st monomer for different chain lengths.

c) Central monomers of the chains of length 10 and more (the first number denotes the chain length, the second the monomer number) in semilogarithmic representation.

substituted by ^{13}C or D. Both of them have a nuclear magnetic moment as has simple hydrogen, so that NMR can be applied.[4]

Reorientation in polyisoprene melts was measured by the group of Monnerie [DLM89, LBM93]. The sample contained 92% *cis*-conformer. Furthermore, there was an investigation with a higher *trans* content of 22% [DP89]. They focused, however, on the *cis*-conformer. Experimentally, the T_1 time is the direct observable (see section 2.5). Note that a shorter T_1 corresponds to a longer relaxation. Recently, a cooperative kinematics (CK) theory likened the experimental results to the local dynamics of torsions in polyisoprene [SBE$^+$99]. CK involves four elements: the backbone geometry, side groups, the environment, and the conformational energetics, i.e. the potential. When a bond undergoes an isomeric transition, the rest of the degrees of freedom are assumed to behave in a way such that the energy difference is minimized. This analysis revealed that the reorientation works mostly by local transitions in dihedral angles. Only on long time scales, the overall chain motion becomes important. This is possible for the carbon-hydrogen vectors, as the overall backbone does not need to change significantly in order to rearrange the hydrogens.

The C$-$H vector reorientation could be observed in simulations. To be not obscured by chain-end effects only the inner-chain monomers are included in figure 6.16. Comparing figures 6.15a and 6.16a, one sees that the hydrogen connected directly to the backbone at carbon C_2 reorients with the backbone. It is strongly tied to it, although there is an additional angle vibration which leads only to an initial decrease. Even such local quantities as bond vectors can be used as observables which relate at least to the dynamics of intermediate-size chain segments.

Figure 6.16b illustrates that different torsion potentials and the side group have considerable influences on the reorientation of vectors. The atoms C_1 and C_5 are both sp^3 hybridized and parts of methylene groups. Still, the reorientations differ. As C_5 is neighbored by the methyl group, the sterical hindrance for the hydrogens tied to it is more pronounced. Thus, the initial stage of the reorientation, which is present for the other methylene $C_1{-}H$ vector, is completely absent for $C_5{-}H$. This is still visible at 413 K (fig. 6.16c), although all relaxations are faster. The above-mentioned experiments [DLM89, DP89] on *cis*-polyisoprene melts showed the same tendency. The spin-lattice relaxation time is shorter for the methylene neighboring the methyl side group than it is for the other methylene. The $C_2{-}H$ vector is even slower (shorter T_1), again in line with the data presented here.

The experimental data [DLM89] provide evidence for a two stage process, whereby the initial stage decreases the correlation function to a value of $1-a$, as there is in the most simple description a fast decay and then a second decay which is not simply exponential. The experimental data were interpreted using the model correlation function

$$C_{\mathrm{reor}}(t) = a e^{-t/\tau_0} + (1-a) e^{-t/\tau_2} e^{-t/\tau_1} I_0({}^{t}\!/\!{}_{\tau_1}) \ , \tag{6.11}$$

whereby τ_0 is the local libration time, τ_1 the time of conformation jumps, and τ_2 is connected to damping. I_0 is a Bessel function. The separation of time scales for polyisoprene is ${}^{\tau_1}\!/\!{}_{\tau_0} \geq 150$ for the two faster characteristic times [LBM93]. Additionally, the two slow processes (τ_1, τ_2) differ by a factor of 40. A separation of motions was used by Lipari and Szabo as well to analyze NMR data of polymers [LS82a, LS82b]. The correlation function they used has the simpler double exponential shape

$$C_{\mathrm{reor}}(t) = \mathcal{S}^2 e^{-t/\tau_1} + (1-\mathcal{S}^2) e^{-t/\tau_2} \ , \tag{6.12}$$

---

[4] In principle the carbon-carbon vectors can be measured as well by selectively substituting both interesting carbons with ^{13}C. However, in practice the amplitudes are too low.

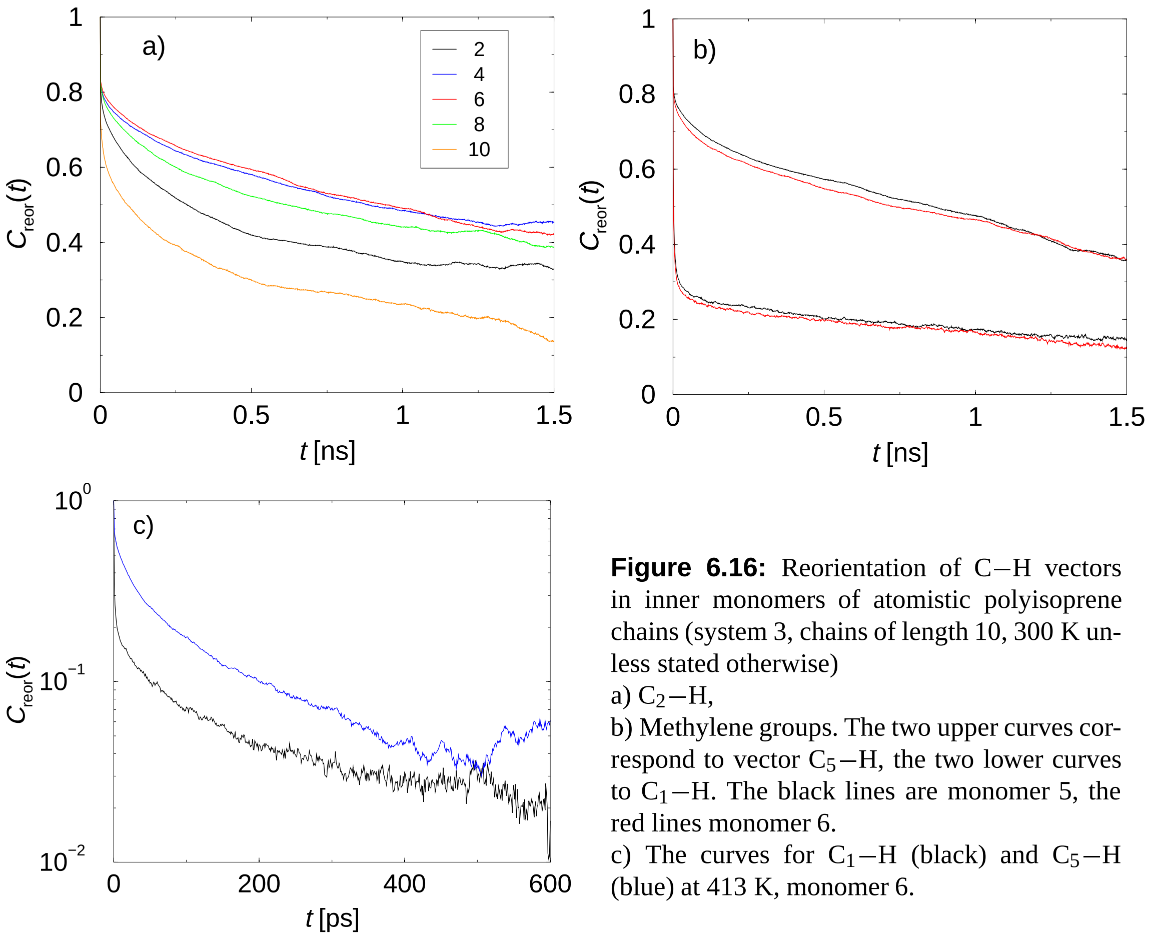

Figure 6.16: Reorientation of C−H vectors in inner monomers of atomistic polyisoprene chains (system 3, chains of length 10, 300 K unless stated otherwise)
a) C_2−H,
b) Methylene groups. The two upper curves correspond to vector C_5−H, the two lower curves to C_1−H. The black lines are monomer 5, the red lines monomer 6.
c) The curves for C_1−H (black) and C_5−H (blue) at 413 K, monomer 6.

vector	a^{cis}_{exp} [DLM89]	a^{trans}_{fit}	$a^{trans}_{1\text{ ps}}$	a^{cis}_{sim} [ME99]
$C_1 - H$	0.40	0.75	0.42	0.28
$C_2 - H$	0.17	0.29	0.16	0.16
$C_5 - H$	0.48	0.29	0.18	0.23

Table 6.12: Comparison of the experimental (*cis*-PI) and simulation (*cis* and *trans*-PI) data for the efficiency of the initial stage of the reorientation process. a_{fit} originates from an exponential fit of the second stage extrapolated to $t = 0$ and $a_{1\text{ ps}}$ is the value of $1 - C_{\text{reor}}$ at 1 ps. In the analysis of the simulations for *cis*-polyisoprene a stretched exponential second process was assumed. The experiments used a range of temperature between 283 K and 363 K. The *trans* simulations were at 300 K and the *cis* simulations at 363 K.

whereby $\mathcal{S}$ relates to the parameter a of Lauprêtre *et. al.* [LBM93] and is the generalized order parameter. Thus, the reorientation motion is described by a local and a global reorientation which simply add up here, as there is no reptation in such short oligomers.

Actual numbers for the three times of the model eq. (6.11) are not provided in refs. [DLM89, LBM93], but only values for a. The values for a for the different vectors are comparable between simulation and experiment (tab. 6.12). The simulation data were determined by an exponential fit of the second part, which is not exactly correct, as the Bessel function was neglected but gives a good estimate. The second to last column shows the values of a, if one takes the value at 1 ps which is the shortest time resolved in the simulations ($a_{1\text{ ps}} = 1 - C_{\text{reor}}(1\text{ ps})$), which would mean that the first process is too fast to be resolved here. This is closer to the experimental data. Thus, the simulations are in fair agreement to experiments. If the conformational jump time is regarded as the time for torsion rearrangement (see below), and keeping in mind that the two times differ at least by a factor of 150 the guess for $a_{1\text{ ps}}$ is probably more realistic. Still, the simulations underestimate the difference between C_1 and C_2 and overestimate the one between C_1 and C_5. One has to keep in mind that the data provided here is for a sample of pure *trans*-polyisoprene oligomers which is presumably quite different from real *cis*-polyisoprene with some added *trans*-conformer. Moreover, the discrepancy becomes weaker for system 1 (below). Recent simulations on *cis*-polyisoprene at higher temperature (T = 363 K and T = 413 K) were interpreted in terms of a two stage correlation, too. There, a separation between the exponential first stage and a stretched exponential second process was deduced [ME99]. The corresponding a-parameters are included in tab. 6.12. Except for the C_5−H vector they are comparable to the data presented here. For C_5−H they are even smaller than the experimental value.

In the reorientation of the C_4−H vectors of the methyl side group the two-stage reorientation is clearly visible (fig. 6.17). The short time reorientation is almost as fast as the reorientation of low-molecular liquids like cyclohexene or cyclohexane, which occurs on time scales of about 3 − 4 ps [SFMP99]. Here the monomer index has almost no influence, which shows that only the very local surrounding contributes. On this time scale the vector does not experience the connection to the chain. Only the rotation of the methyl group and bond angle vibrations show up.

The long time tail, however, is again linked to the overall reorientation. The bonding to the chain leads to a bias in the orientation of the methyl group, which prevents the correlation function from total decorrelation on the short time scale. This second process is influenced by chain end effects. It is exponential with decay constants of $\tau_{\text{end}} \approx 1.0$ ns and $\tau_{\text{center}} \approx 3.1$ ns respectively. The decay times were determined by an exponential fit of the time region between 500 and 1250 ps.

Correlation times for the reorientation of *cis*-polyisoprene in the melt were calculated by Moe

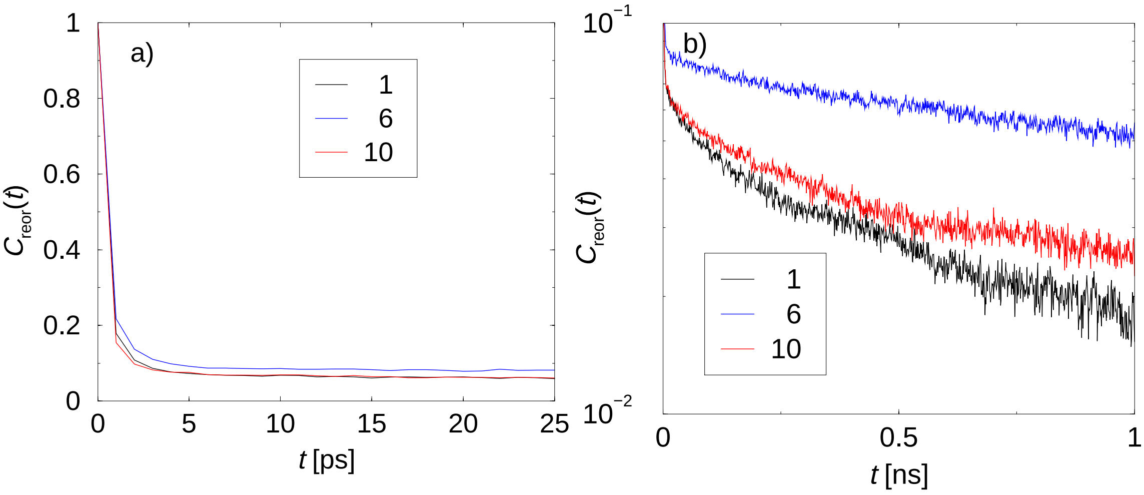

Figure 6.17: a) Short time reorientation of methyl C−H vectors, monomer number as in legend. b) Long time. Clearly, the two stages are separate. (System 3, T = 300 K, only 10mers are included)

and Ediger, who used one long chain under periodic boundary conditions [ME96]. In table 6.13 the data of this work is compared to their data and the high temperature limit of the experiments. At 300 K, the correlation times were determined by numerical integration of $C_{\text{reor}}(t)$ over the first nano-second. Additionally, a correction for the long-time tail was applied with analytical integration of the fitted exponential decay. For the methyl groups the numerical integration extended only to 20 ps.

Heating to 413 K speeds the simulation up. Here the numerical integration was performed up to 100 ps except for the methyl groups (20 ps) and the C_1−H (200 ps). Beyond, the exponential function was integrated analytically. For the oligomers, however, the results are very similar to a numerical integration to 400 ps, which was performed additionally in order to directly compare to the data by Moe and Ediger. For real polymers there is probably more difference.

If the data is compared directly to extrapolated experimental data an overall discrepancy of about 50% of *trans*-simulations presented here from the experiments is found. The integration error in the simulation as well as the extrapolation of the experiments are sources of error. The systems are not the same and the simulation model does not reflect reality perfectly. The experiments themselves are not perfectly reliable. Witt *et al.* showed that NMR experiments for systems as simple as benzene can result in reorientation times differing by one order of magnitude [WSDMP00]. A direct comparison at lower temperature is not possible, as the model-free limit of extreme narrowing can be no longer applied then.

In the simulation system 2, the hydrogen at C_5 reflects too much the reorientation of the backbone as it reorients on the time scale of the double bond. Experimentally there is a difference between C_5−H and C_2−H. This may result from the interaction with the methyl group which repels the H at C_5 very effectively. In system 1 the difference is more pronounced, as the non-bonded interactions between the methyl hydrogens and the methylene hydrogen are switched off ($1-5$ interaction).

Denault *et al.* estimated for chains of molecular weights between 7×10^3 g/mol and 1.5×10^5 g/mol at 30 °C (303.15 K) a segmental reorientation time of 1.0 ns and at 100 °C (373.15 K) of 43 ps by analyzing their methylene reorientations [DP89]. For this, they used the

Vector	$\tau_{\text{reor}}^{trans,\text{sys}\,1}$[ps]	$\tau_{\text{reor}}^{trans,\text{sys}\,2}$[ps]	$\tau_{\text{reor}}^{trans,A}$[ps]	$\tau_{\text{reor}}^{trans,B}$[ps]	$\tau_{\text{reor}}^{(\text{exp})}$[ps]	τ_{reor}^{cis}[ps]
	300 K		413 K			
C=C	2400	1900	49	51	–	–
C_1−H	810	640	39	25	22	50
C_2−H	2400	1900	50	46	35	75
C_4−H	–	480	2.1	5.8	3.6	7.6
C_5−H	1200	1800	67	55	26	60

Table 6.13: Comparison of simulated reorientation times in *trans*-polyisoprene (this work) and *cis*-polyisoprene (ref. [ME96]) to data determined by extrapolation of experiments at lower temperatures into the extreme narrowing limit (sec. 2.5).
The *cis*-data were determined by numerical integration of the first 400 ps. For the *trans*-polyisoprene only the innermost monomers are used. At 413 K the analysis was done two-fold in order to compare more directly to the old simulations. A: numerical integration and exponential long-time tail (see text), B: numerical integration to 400 ps. The simulation errors are estimated to be about 20% (difference between systems).
The reorientation of the methyl group in the NVT simulation could not be calculated meaningful, as there was a force-field problem. The hydrogens were connected to the carbon with an additional torsion, which was too strong.

Schaefer model [Sch73] for segmental reorientation. In this model a χ^2-distribution of relaxation times is assumed arising from cooperative local motion.

The values are in the order of magnitude of the reorientation data presented here for 300 K. An Arrhenius-plot of the segmental reorientation of Denault *et. al.* in comparison to the simulated reorientation of the double bond shows a similar temperature dependence (fig. 6.18). The activation energies deduced are $E_A^{(\text{sim})} \approx 33$ kJ/mol and $E_A^{(\text{exp})} = 65$ kJ/mol at low temperature and $E_A^{(\text{exp})} = 19$ kJ/mol at high temperature. Thus, the simulated energy lies nicely in between. The fictitious experimental activation energy taking only the lowest and highest point into account arrives at $E_A^{(\text{exp})} \approx 40$ kJ/mol rather close to the simulation value. To decide if there is a similar behavior as in experiments with two temperature regimes more simulations would be necessary at intermediate temperatures.

The two different realizations of the force-field, differing in the inclusion of all $1-5$ and $1-6$ interactions, express themselves mainly in the different speeds of the methylene group at C_5. The suppression of the excluded volume interactions in system 1 between the hydrogens leads to relative reorientation times which come closer to experiments.

6.7.2 Torsion dynamics

The torsion distributions of figure 6.8 allow the classification of the torsion states. Torsions 1 and 3 were found mostly in the *skew* states (120 or 240°); torsion 2 has a high peak at *trans* and two lower maxima at the *gauche* states. This is comparable to the above mentioned analysis of *cis*-polyisoprene using cooperative kinematics theory, where qualitatively similar potentials were derived from experimental NMR results [SBE+99]. According to this analysis, the methyl group leads to considerable displacements of the atoms in conformational changes. So isomeric transitions in polyisoprene feel more resistance than e.g. in polybutadiene.

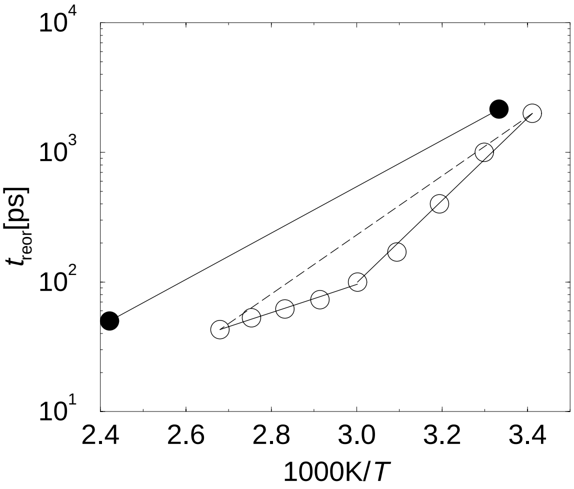

Figure 6.18: Arrhenius-plot of the comparison of the C=C reorientation time of the simulations (filled circles) to the segmental reorientation time inferred by Denault *et al.* from their experiments [DP89]. For the simulations the values of table 6.13 are averaged at 300 K and 413 K respectively.
The solid lines are exponential fits to the curves. The dashed line is the experimental "fit" disregarding all but the outermost points.

Torsion	State	Angles
1,3	*cis*	$-60° < \phi < 60°$
1,3	*skew*$^+$	$60° < \phi < 180°$
1,3	*skew*$^-$	$-180° < \phi < -60°$
2	*trans*	$120° < \phi < 240°$
2	*gauche*$^+$	$0° < \phi < 120°$
2	*gauche*$^-$	$-120° < \phi < 0°$

Table 6.14: The definition of torsional states used for calculation of the torsion correlation times. The torsions are defined in table 6.3.

The torsions were assigned to states between which transition times were calculated. The choices were inspired by the distribution and are summarized in table 6.14. The transitions between the states were calculated with the polymer split into two parts, which does not reveal a noteworthy end-effect. For some transitions even more events were found in the inner monomers. Equilibrium can be assumed, as there was no drift in the torsion distribution during the simulations. The numbers of forward and backward transitions is very similar.

For torsion 1, almost all transitions go above the two *gauche* barriers (tab. 6.15). The *trans* barrier is not impossible to cross but this transition is about two orders of magnitude slower. Torsion 2, on the other hand, does not show such large variations. Still, the rates are different (if only by a factor of 3) as are the populations. The dynamics of torsion 3 is almost the opposite of the first torsion. Nearly all transitions involve the low *trans* barrier between the *skew* states. The *cis* state is weakly populated and few transitions link to it.

6.8 General remarks

In this chapter it has become clear that for very local scales the atomistic details are important. The coordinations of the different carbons can only be treated if these carbons have a different environment. The different reorientation times of the respective C-H vectors show the need for a detailed atomistic treatment, too. On the other hand, even for the most local issues, such as the reorientation of the methyl hydrogens, the overall features shine through as the second time scale emerges. The different torsion potentials along the backbone show that local substitution of methyl groups for hydrogens can have important effects at least on the scale of a few monomers.

Torsion	Transition	all	inner	end
1	$s^+ \rightarrow c$	5.45	4.87	5.76
1	$c \rightarrow s^+$	5.45	4.86	5.77
1	$s^- \rightarrow c$	5.20	5.08	5.26
1	$c \rightarrow s^-$	5.20	5.09	5.26
1	$s^- \rightarrow s^+$	0.08	0.07	0.09
1	$s^+ \rightarrow s^-$	0.09	0.08	0.09
2	$g^+ \rightarrow g^-$	0.36	0.63	0.21
2	$g^- \rightarrow g^+$	0.35	0.62	0.21
2	$t \rightarrow g^-$	0.93	1.07	0.86
2	$g^- \rightarrow t$	0.94	1.08	0.87
2	$t \rightarrow g^+$	0.84	0.80	0.87
2	$g^+ \rightarrow t$	0.85	0.80	0.87
3	$c \rightarrow s^+$	0.13	0.19	0.10
3	$s^+ \rightarrow c$	0.13	0.19	0.10
3	$c \rightarrow s^-$	0.10	0.13	0.09
3	$s^- \rightarrow c$	0.10	0.13	0.09
3	$s^- \rightarrow s^+$	3.01	2.84	3.10
3	$s^+ \rightarrow s^-$	3.02	2.85	3.11

Table 6.15: Average number of transitions per nanosecond and per torsion between the torsion states for system 3 ($T = 300$ K). A torsion is defined as end-torsion if it is at most three monomers distant from the end. There are 314 inner and 586 end torsions.

There is the possibility of coarse-graining of these polymers, as the time and length scales are rather separate. Most local interactions do not affect the global structure. In fact, the generic model of section 3.3 captures many of the essentials of polyisoprene. This has become evident already in the mutual orientations of the chains (sec. 6.6.2). The following section will explore the connection between atomistic simulations and coarse-grained descriptions for polyisoprene in more detail.

The structure of the oligomer melt is comparable to a melt of longer chains, as is seen by the similar structure factors of Moe and Ediger for long *cis*-polyisoprene chains. A decisive structural element is the double bond in polyisoprene, as it keeps the monomers rigid and planar. Thus, the closest approach is a stacked conformation, which is in contrast to the perpendicular approach in a chain of spherical beads. The inclusion of all the hydrogens is deemed necessary as the local packing issues differs for a simple united atom sphere in comparison to e.g. a methyl group which is a sphere with three additional small “hills” on top. The directionality of packing interactions would be lost. However, for a slightly bigger scale than direct contact, united atoms are already sufficient. Generic features are important for the overall conformations and their relaxation. As long as intermediate scales ($r \gtrsim 0.5$ nm) are of interest, the generic models are sufficient. For the detailed input to them, however, atomistic simulations are important.

The decamers presented here are definitely not long chains. End-effects as well as finite chain length effects play significant roles. The inner monomers give an impression of the long chain limit as the correlation functions are similar for the, say, four inner most monomers. They are already sufficient, if local scales are of interest, and, as discussed above, for longer length scales the less detailed models can already reveal the important properties.

7 An attempt of unification

In this thesis, polymer-melt systems have been investigated for generic issues. The influence of the specific chemistry on the example of polyisoprene has been discussed as well. To sum up the results and in order to provide a general view, a mapping of the detailed model onto the simple generic model is performed. Finally, the main issues are summarized and conclusions are drawn.

7.1 Comparison of the dynamics of monomeric segments in atomistic and bead-spring models

The atomistic results of statics and dynamics of polyisoprene in chapter 6 give confidence that the simulated model is realistic. To link these simulations to the coarser model of chapters 4 and 5 containing only monomeric units, the large-scale dynamics of the atomistic data is now presented in comparison. First, the diffusion of the chains is compared to obtain a mapping of time and length scales. With this mapping, reorientation correlation functions of inter-monomer vectors are investigated and compared between atomistic and mesoscale models.

7.1.1 Mean-squared displacements

The mean-squared displacement of inner monomers $g_1(t)$ and of whole chains $g_3(t)$ for bead-spring models was discussed in section 5.3. The data for the atomistic polyisoprene oligomers at 300 K and 413 K are compared to the chains with the same number of monomers in the bead-spring case. For the atomistic chains, the segments are localized at the centers of mass of the double bond. For matching the length scales, the end-to-end distance of the decamers in both models is used. Therefore, in figure 7.1 the ordinates are rescaled by the squared average end-to-end distance. This results for the bead-spring system with stiffness $x = 1.5$ in a mapping of $\sigma(300\text{ K}) = 0.54$ nm or $\sigma(413\text{ K}) = 0.57$ nm respectively, whereby $x = 1.5$ was chosen, as the bond-correlation function for the inter monomer vectors decays approximately on the same scale (compare fig. 4.1 and fig. 6.7). As the fully flexible chains have a similar persistence length, they are displayed as well. Their distance mapping arrived at $\sigma(300\text{ K}) = 0.76$ nm and $\sigma(413\text{ K}) = 0.70$ nm. Thus, the Kuhn length, calculated in section 6.5 to be $l_K = 1.06$ nm for 300 K, corresponds to about two monomers.

The center-of-mass mean-squared displacements g_3 for the atomistic simulation at 413 K and the bead-spring simulation can be superimposed by scaling one parameter which is the Lennard-Jones time (fig. 7.1b). The curves overlap by one decade. At 300 K this is not possible as the atomistic simulations did not reach the displacements of the bead-spring chains. At 413 K the Lennard-Jones time units read $t^*(x = 1.5) = 68$ ps and $t^*(x = 0) = 126$ ps.

The mean-squared displacements of the central monomers (fig. 7.1a) do not coincide within the same mapping. There is about a factor of two difference, which has to vanish for longer times

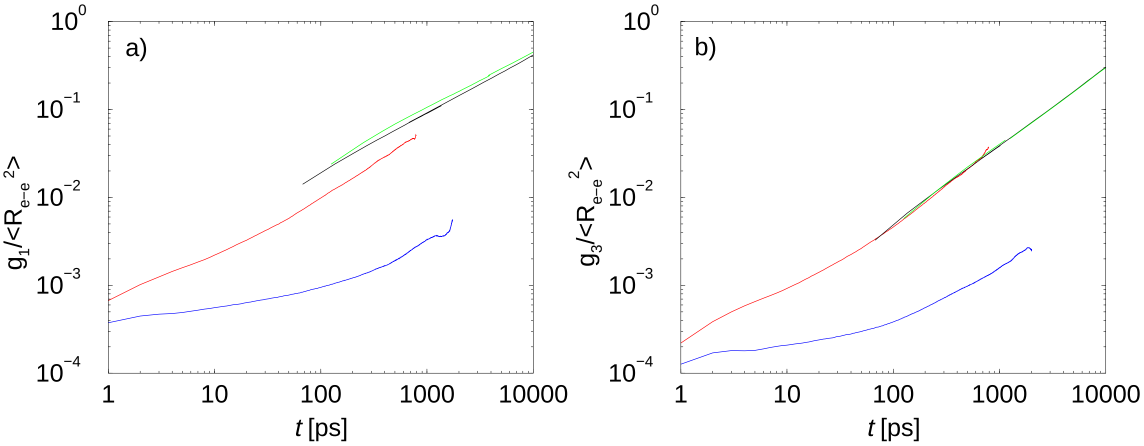

Figure 7.1: Comparison of the functions a) $g_1(t)$ and b) $g_3(t)$ for atomistically simulated polyisoprene to bead-spring chains with full flexibility and with $x = 1.5$. The red lines are the atomistic simulations at 413 K, the blue lines at 300 K, the black lines the bead-spring data for $x = 1.5$, and the green for full flexibility. In both figures the ordinates are rescaled by the mean squared end-to-end distance. The abscissas are rescaled in order to yield a mapping of times using $g_3(t)$.

when the center of mass dominates the motion completely. So one has to conclude that the local dynamics is qualitatively different.

7.1.2 Comparative Rouse mode analysis

For the comparative analysis of Rouse modes, the centers of mass of the double bonds act again as monomers for a simplified chain. To such coarsened chains a Rouse analysis, as explained in section 2.2, can be applied. If the Rouse model were confirmed properties such as viscosities could be deduced from the simulations [HMT98].

The Rouse modes for 300 K in figure 7.2a do not collapse onto a master curve. The different modes in Rouse scaling fall onto parallel lines for not too small times. This may be the influence of the short-time regime, in which Rouse modes do not perfectly obey the standard scaling, or the dynamics is truly different. The possible reasons cannot be separated in simulations of this length. There is a hint of an exponential decay of the higher modes on intermediate times.

At 413 K, at least the two lowest modes collapse onto a master curve (fig. 7.2b). Here, the Rouse modes for the bead-spring systems ($x = 0, 1.5$) at length 10 are shown for comparison. They can be brought to coincidence with the atomistic curve by taking $t^* = 36$ ps ($x = 0$) and $t^* = 23$ ps ($x = 1.5$). These LJ times are, however, different by about a factor of 3 from those obtained from matching the mean-squared-displacements (sec. 7.1.1). This may be related to the fact that even for $T = 413$ K full relaxation was not achieved. A longer simulation allowing the chains to diffuse several end-to-end distances would be desirable, in order to reliably compare the diffusion coefficients. Then it may be possible to perform a more reliable Rouse analysis.

Still, the simulations allow a rough estimate of the Rouse time at 413 K. From the first and second mode one deduces $\tau_R = 3.4$ ns. From this a viscosity of $\eta = \frac{\pi^2 \rho k_B T}{12M} \tau_R = 11.7$ mNs/m^2 can be estimated. M denotes here the (average) molecular weight of the chain. For comparison, a simulated atomistic oligoethylene (C_{46}) at $T = 450$ K has a value of 1.46 mNs/m^2 [HMT98] which is, however, clearly below the experimental value of 2.5 mNs/m^2. Experimental data for

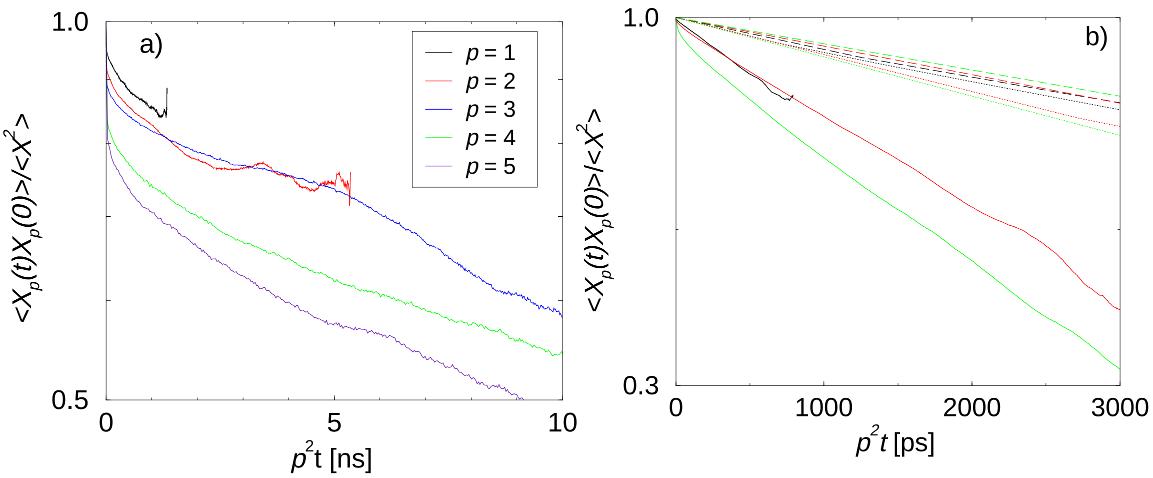

Figure 7.2: Rouse mode analysis of the atomistic simulations of
a) System 1 (300 K): The Rouse scaling fails.
b) Decamers in system 3b (413 K) and bead-spring systems. Solid lines: atomistic simulations, dashed: bead-spring flexible, dotted: $x = 1.5$. The black curves correspond to mode $p = 1$, red to $p = 2$ and green to $p = 3$.
For the bead-spring chains the time is mapped according to g_3 (fig. 7.1b) in order to be consistent with the other comparative figures.

polyisoprene are apparently not available in the literature. Still, comparing the polyisoprene decamers (C_{50}) to the polyethylene which is unbranched and at higher temperature suggests that the order of magnitude should be correct. More could not be expected by this determination.

7.1.3 Reorientation

To compare the reorientation behavior of the two models, vectors along the atomistic backbones connecting neighboring monomers have to be defined. They connect the same carbon type on different monomers (e.g. $C_1{-}C_1$). In figure 7.3 these reorientations are shown classified according to monomer indices. The end effects are much weaker than for the intramonomer vectors (sec. 6.7.1). For both the C_1 and the C_2 vectors, only monomer 1 has to be neglected, as the respective atoms are at the very end. It was also found that $C_1{-}C_1$ relaxes faster than $C_2{-}C_2$, as C_1 is not tied to the double bond (fig. 7.3a,b). However, this influence is weak. Already at this scale, the generic features of the correlation functions are dominant. For 413 K (fig. 7.3c), the end-effects become even weaker in addition to the overall speedup.

In figure 7.4 the reorientation behavior of these vectors (413 K) is compared to the bead-spring model. There is no adjustable factor involved, as the time mapping originates from the mapping fixed by the diffusion speed. Clearly, the correlation function of the simple chain with $x = 1.5$ continues very well both curves of the atomistic simulations. Therefore, a mapping of a detailed atomistically simulated chain onto a much simpler description can be achieved by including only an angular potential.

However, as shown above, a Rouse description cannot really be applied to polyisoprene. It cannot be decided whether this depends on the short chain length or if there is a more fundamental discrepancy. As the displacements of the central monomers could not be brought to coincidence, either, the latter is more probable. This result is in agreement with the findings of Paul *et al.* for

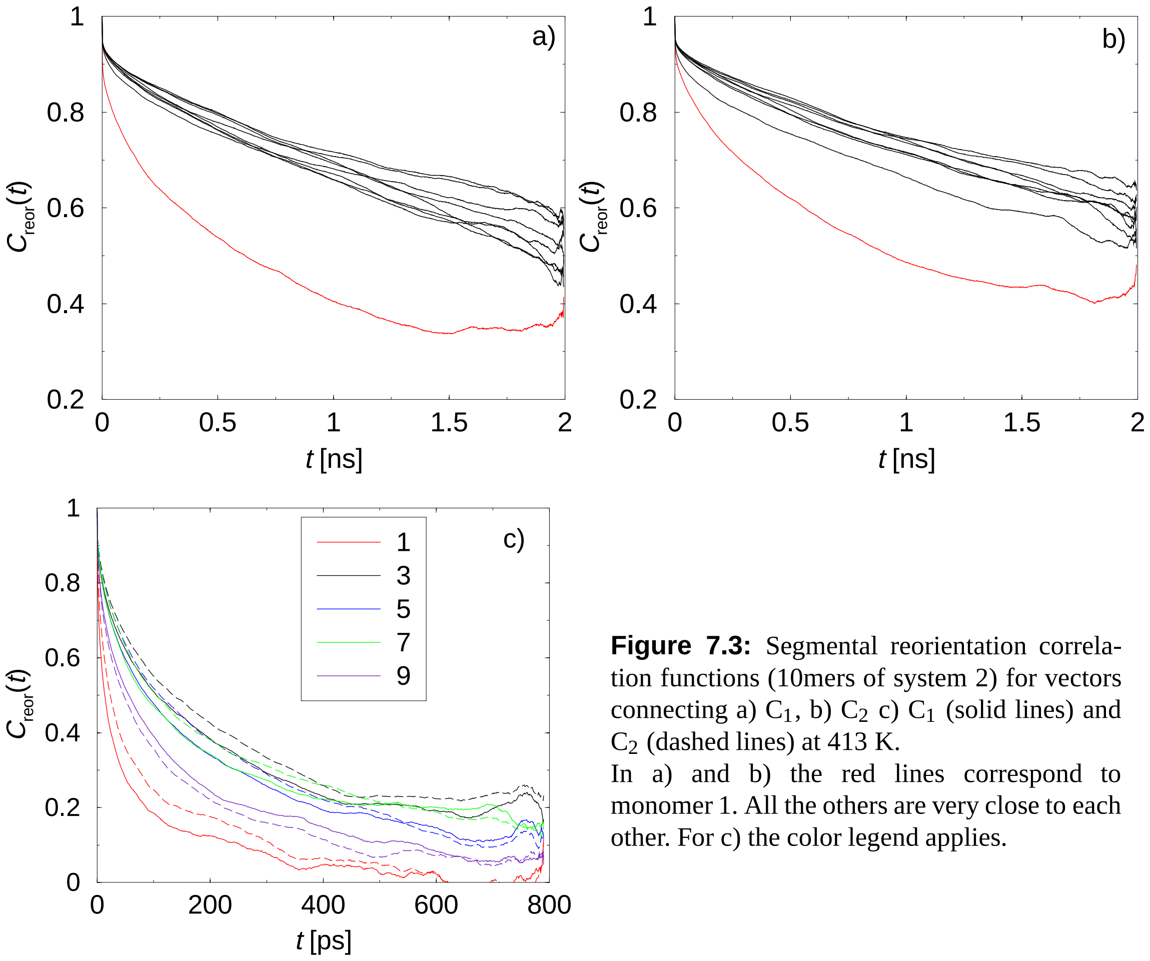

Figure 7.3: Segmental reorientation correlation functions (10mers of system 2) for vectors connecting a) C_1, b) C_2 c) C_1 (solid lines) and C_2 (dashed lines) at 413 K.
In a) and b) the red lines correspond to monomer 1. All the others are very close to each other. For c) the color legend applies.

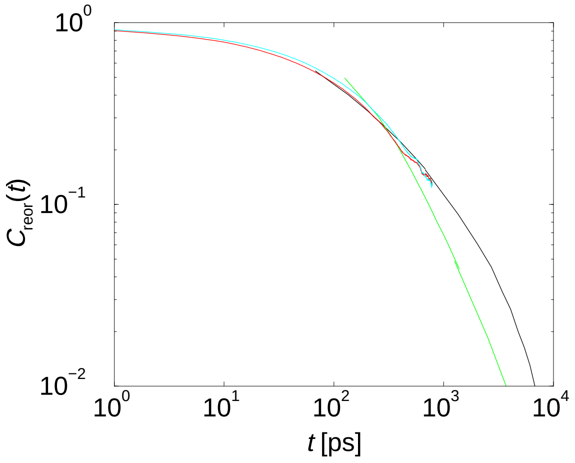

Figure 7.4: Comparison of the reorientation behavior of vectors connecting neighboring monomers. The data for the the bead-spring model (green: fully flexible, black: $x = 1.5$) are rescaled according to the times from g_3, the atomistic data at 413 K are averaged over all but the first monomer (red: C_1, light blue: C_2).

polyethylene [PSY97]. They have shown that for the large-scale properties the Rouse model is a reasonable description whereas for the internal modes there are systematic deviations.

7.2 A view back on the atomistic scale

One now sees that the atomistic scale experiences influences from two sides. On the one hand, the local interactions between the atoms are the dominant contribution; even quantum chemical influences have to be taken into account. However, the freedom of the atoms is constrained by the connection to the rest of the chain. Therefore, the whole problem is to be solved in a self-consistent manner. No scale can be interpreted alone. The long-time tails in the atomistic reorientation functions reflect exactly these influences. They merge with the generic functions, i.e. on this time scale there is even for the very local processes no other way than to behave according to generic constraints of the connectivity.

Although there are links between the different length scales, it is still useful to draw conclusions from atomistic simulations alone. The very local static properties arise from the packing of carbons and hydrogens together with the double bond. Other local architectures would lead to different local structures and short-time dynamics. From the polymer physics point of view, this atomistic scale is not polymeric, as the typical ingredients to a polymer, the connectivity and with it the constraining of the motion and global packing are only corrections to the behavior of monomers seen as small molecules. Different “small molecules”, however, have different influences on the bigger scales, the most important being the persistence length leading to different dynamic behaviors on *global* scales.

7.3 The global scale - Stiffness versus entanglements

It has become clear in chapter 5 that the dynamics of entangled semiflexible polymer systems is not easily mapped to a simple bead-spring chain, as the length scales originating from the different interactions are linked to each other. With a view to the atomistic results one has to conclude that the only way of understanding polymer systems from a molecular level up to rheologic properties is to start at the very bottom, i.e. with all atoms involved. With such a detailed treatment one has to calculate the ingredients to the next scale model, e.g. the persistence length. However, only if the coarser analysis of the detailed system and the system to which it is mapped can be brought to coincidence, as is the case for the reorientation dynamics presented here, one can assign a meaning to the data obtained on the coarse grained level. Otherwise a refining of the mesoscale model is necessary if the connection to the “real” world should not be lost.

On the bead-spring level, several results emerge which cannot be obtained in the detailed atomistic picture. A coarse-graining of the local-scale properties into an effective monomer or Kuhn segment is possible from a static point of view. There is only one dominant length scale: the persistence length (chapter 4). This suggests that on large length scales, i.e. longer than any local scale in a polymer, the random walk picture arises irrespective of local packing. For such purposes the link to the detailed model is not necessary as the mesoscopic scaling regime is generic for almost all polymers due to the dominance of entropy, whereas the local scales are governed by energetic contributions. The atomistic simulations support this picture. There are considerable local differences between the distinct correlation functions of different carbon atoms. However, the overall structure is only weakly affected. For the bead-spring case this holds as long as the nematic ordering transition is not approached; then also the mesoscopic entropic effects change completely, entropy can drive a liquid crystalline ordering.

The mapping to Kuhn segments fails for dynamics, as the length and time scales interdepend substantially. Dynamically, one encounters *two* important length scales: first, again the persistence length already present in the statics and, second, the entanglement length describing the constraints imposed by non-crossability of the chains due to excluded volume. The latter length decreases systematically with stiffness, so that the two dominant lengths are not at all independent. The tube diameter in the reptation picture is related to the entanglement length and decreases with stiffness as well. It describes the anisotropy of motion of a chain in the matrix imposed by the other chains in the system. The relation between tube diameter and entanglement length is changed by rigidity as well. The tube becomes more elongated.

In particular, when the persistence length and the entanglement length are of the same order of magnitude, new behaviors emerge, which cannot be deduced by mapping to Rouse chains or other simple models. The chains are more tightly constrained by their neighbors (small tube diameter). The reptation picture gives a useful illustration of this, as the snake-like motion is the dominant contribution to the dynamics. However, the standard reptation picture established by de Gennes, Doi, and Edwards for flexible melts has to be modified. The underlying dynamics no longer obeys the Rouse picture. Therefore, one may be misled by investigations of key observables, such as the mean-squared displacements of central monomers, which partially looks as if there was an unconstrained motion. Thus, the dynamical exponents are no longer the same, i.e. the dynamics changes *qualitatively*. This has to be kept in mind if the term *reptation* is still used. Reptation can mean a reptile-like motion in a tube, which is still found; however, the other motion types in the standard tube model, like the free wiggling inside the tube, are no longer present if the stiffness becomes too strong. Comparing to results of NMR experiments and theoretical predictions of reorientation in a tube, the simulations can only be explained if stronger entangling for stiffer chains is assumed consistent with the dynamical structure factors. The most direct evidence for motion in the tight tube, however, is the visualization of the chains. The title picture of this thesis illustrates exactly this behavior.

Reptation is in the literature also discussed for the almost rigid rod case [DE86]. The dynamics of truly rigid chains is drastically different from the flexible case as well as from the systems presented here. A rigid chain leaving the very straight tube can only slightly reorient, i.e. by an angle of the order of tube diameter divided by chain length. The motion is stronger biased along the chain contour leading to reorientation on time scales longer than tube disengagement. So depending on chain stiffness there are at least two qualitative transitions in the local dynamics of the chain.

Direct comparison to experiments even on the coarse-grained level can be regarded a success. One understands that for the reproduction of the experimental dynamical behavior a reptating chain is necessary but not sufficient. Stiffness is needed in order not to loose the correlation completely on the local first stage of reorientation. In addition, it brings the entanglement length to so small values that chains of length 200 are already highly entangled. Moreover, *local* stiffness enhances the *global* reptation, as other relaxation modes are effectively suppressed.

7.4 Stiffness on different scales

This thesis shows that stiffness is an important ingredient on a wide variety of scales in polymers. On the atomistic end, it enters mainly via torsional potentials. The torsion distribution and dynamics dominates together with excluded volume the local scales. For obtaining reliable potentials for atomistic simulations of e.g. polyisoprene, the electronic degrees of freedom cannot be neglected, so that even quantum chemical methods have to be applied. The treatment of the quantum influences by potentials is sufficient; quantum degrees of freedom need not to be taken into account for the dynamics as the comparison to experiment succeeds with classical simulations.

On the other end of the scales, one just has a simple chain of beads, but again with stiffness. Stiffness qualitatively changes the mesoscale dynamics of chains in the melt. To look for the influences and consequences of rigidity, one has to understand the different nature of stiffness on various time and length scales. Thus, all the methods from quantum chemistry up to simulations of largely coarse-grained model chains were to be taken into account to reveal more of the nature of this important characteristics and to shine a light on the same problem from various viewpoints.

The mapping procedure between the models shows that the degree of stiffness is one important link between the scales. The best match of the dynamics of polyisoprene decamers to model decamers was obtained for similar persistence length. The mapping, however, also shows that the explicit local dynamics can be different for the same stiffness. This is not too surprising as there are of course different polymers with similar persistence lengths. But, the dynamics can almost not be compared between a fully flexible and a completely rod-like polymer. It can be concluded that coarse-graining is a promising way of attack as long as precautions are taken not to loose the complete chemical identity of the chains.

7.5 Final conclusions

Finally, one can conclude three major results from this work:

- There is a new, more pronounced, type of reptation in melts of locally stiff chains. This one may call *strong* reptation.
- The reorientation dynamics, observed by double-quantum NMR in polybutadiene, can be explained by a simple model including stiffness.
- An atomistically detailed model for polyisoprene can be successfully mapped to a simple model if scales of more than a monomer size are considered.

Clearly, the investigations opened more new questions than they could answer, or to say it with Bertolt Brecht:

Der Vorhang zu und alle Fragen offen.

A Relationship between double-quantum correlation function and reorientation correlation function

In section 5.1 the identity

$$C_{\mathrm{DQ}}(t) = \frac{1}{5} C_{\mathrm{reor}}(t) \tag{A.1}$$

was used under the assumption of an isotropic distribution which was confirmed also by simulations. This is now proved.

The double quantum correlation function is defined as

$$\begin{aligned} C_{\mathrm{DQ}}(t) &= \left\langle P_2\left[\hat{u}(t)\hat{B}\right] P_2\left[\hat{u}(0)\hat{B}\right]\right\rangle \\ &= \left\langle \frac{1}{2}\left(3[\hat{u}(t)\hat{B}]^2 - 1\right)\frac{1}{2}\left(3[\hat{u}(0)\hat{B}]^2 - 1\right)\right\rangle . \end{aligned} \tag{A.2}$$

Without loss of generality $\hat{B} = \hat{e}_z$ can be chosen. So eq. (A.2) reduces to

$$\begin{aligned} C_{\mathrm{DQ}}(t) &= \frac{1}{4}\left\langle\left[3u_z(t)^2 - 1\right]\left[3u_z(0)^2 - 1\right]\right\rangle \\ &= \frac{1}{4}\left\langle 9u_z(t)^2 u_z(0)^2 - 3\left[u_z(t)^2 + u_z(0)^2\right] + 1\right\rangle . \end{aligned} \tag{A.3}$$

On the assumption of isotropic distribution of the unit vectors at all times, which is justified by the symmetry of the system, one arrives at

$$\left\langle u_z(t)^2 + u_z(0)^2\right\rangle = 2\left\langle u_z^2\right\rangle = \frac{2}{3}\left\langle \vec{u}^2\right\rangle = \frac{2}{3} . \tag{A.4}$$

Using this result equation (A.3) reduces to

$$C_{\mathrm{DQ}}(t) = \frac{1}{4}\left\langle 9u_z(t)^2 u_z(0)^2 - 1\right\rangle . \tag{A.5}$$

In the limit $t = 0$, which means $\vec{u}(t) = \vec{u}(0)$, one finds

$$\begin{aligned} C_{\mathrm{DQ}}(0) &= \frac{1}{4}\left\langle 9u_z^4 - 1\right\rangle \\ &= \frac{1}{4}\left(\frac{1}{2}\int_0^{\pi} \mathrm{d}\theta \sin\theta (9\cos^4\theta - 1)\right) \\ &= \frac{1}{8}\int_{-1}^{1}\left(9x^4 - 1\right)\mathrm{d}x = \frac{1}{4}\left|\frac{9x^5}{5} - x\right|_0^1 = \frac{1}{5} . \end{aligned} \tag{A.6}$$

As the normal reorientation correlation function reads

$$C_{\mathrm{reor}}(t) = \Big\langle P_2[\vec{u}(t)\vec{u}(0)]\Big\rangle \tag{A.7}$$

it transforms to

$$\begin{aligned} C_{\mathrm{reor}}(t) &= \left\langle \frac{1}{2}\left(3\left[\vec{u}(t)\vec{u}(0)\right]^2 - 1\right)\right\rangle \\ &= \left\langle \frac{1}{2}\left(3[\cos\theta\cos\theta' + \sin\theta\sin\theta']^2 - 1\right)\right\rangle \\ &= \left\langle \frac{1}{2}\left(3[(\cos\theta\cos\theta')^2 + 2\cos\theta\cos\theta'\sin\theta\sin\theta' + (\sin\theta\sin\theta')^2] - 1\right)\right\rangle . \end{aligned} \tag{A.8}$$

by applying the definitions $\cos\theta = u_z(t)$ and $\cos\theta' = u_z(0)$. The term

$$\Big\langle 2\cos\theta\cos\theta'\sin\theta\sin\theta'\Big\rangle = 0 \tag{A.9}$$

vanishes for an isotropic distribution by either averaging over θ or θ'. This illustrates that for any value of u_z there are as many positive and negative values of u_x and u_y. Thus, both C_{reor} and C_{DQ} depend linearly on $\kappa = \langle u_z(t)^2 u_z(0)^2\rangle$:

$$\begin{aligned} C_{\mathrm{DQ}} &= a\kappa + b \ , \\ C_{\mathrm{reor}} &= c\kappa + d \ , \end{aligned} \tag{A.10}$$

so that one arrives at

$$C_{\mathrm{DQ}}(t) = \alpha C_{\mathrm{reor}}(t) + \beta \ . \tag{A.11}$$

On the condition that in the limit $t \to \infty$

$$C_{\mathrm{DQ}}(t \to \infty) = C_{\mathrm{reor}}(t \to \infty) = 0 \tag{A.12}$$

one can conclude

$$\beta = 0 \ . \tag{A.13}$$

Now α just reduces to the fraction at $t = 0$

$$\alpha = \frac{C_{\mathrm{DQ}}(0)}{C_{\mathrm{reor}}(0)} = \frac{1}{5} \ . \tag{A.14}$$

B List of Symbols

Following are the symbols used throughout the work. Only short time used abbreviations are skipped.

Symbol	Description
a	parameter to separate two stage reorientation
$\vec{B}$	magnetic field
β	amplitude of correlation reorientation functions
C_{DQ}	double quantum correlation function
C_{reor}	reorientation correlation function
C_N	characteristic ratio (for N monomers)
C_∞	characteristic ratio (limit for long chains)
D	diffusion constant
d	segment length
d_{T}	tube diameter
Δt	timestep
ΔE	energy difference
ϵ	nonbonded interaction parameter
f	penalty function
$\vec{F}$	force
$\vec{f}$	stochastic force
$g^{\pm}$	*gauche* ± state
G	oscillatory shear modulus
G'	storage modulus
G''	loss modulus
G_N	plateau modulus
g_1	mean-squared displacement of inner monomers
g_3	mean-squared displacement of center of mass
γ	strain, gyromagnetic ratio
H	Hamiltonian
H_{vap}	enthalpy of vaporization
J	spectral density
$\mathcal{K}$	population flow
κ_T	isothermal compressibility
k_B	Boltzmann’s constant
L	contour length
λ	deflection length
l	box length
l_{b}	bond length

Symbol	Description
l_e	entanglement length
l_K	Kuhn segment length
l_p	persistence length
M_c	critical molecular weight
M_e	entanglement molecular weight
M_n	number averaged molecular weight
M_w	weight averaged molecular weight
m	particle mass
N	monomer number
N_C	number of chains
N_e	entanglement monomer number
ν	scaling exponent
OCF	static orientation correlation function
ω	frequency
p	packing length, Rouse Mode index, pressure
P_1	first Legendre polynomial
P_2	second Legendre polynomial
Π	direction correlation functions of displacements
r	distance
RDF	radial distribution function
$\vec{R}$	position vector of a monomer
$\vec{R}_\mathrm{cm}$	position of the center of mass
r_cutoff	interaction cutoff
$\vec{R}_\mathrm{e\text{-}e}$	end-to-end vector
r_exclude	exclusion radius for non-reversal random walk
R_gyr	radius of gyration
ρ	density
s	contour coordinate
S	dynamical order parameter
S_SC	single chain structure factor
σ	stress, nonbonded interaction radius
T	temperature
t	time, *trans* state
t^*	Lennard-Jones reduced time
T_1	spin-lattice relaxation time
τ_d	disengagement time
τ_e	entanglement time
τ_p	decay times of eigenmodes
τ_p	pressure coupling time
τ_R	Rouse time
τ_reor	reorientation time
t_sim	simulation time
$\vec{u}$	unit vector along the chain
U_bend	bending energy
V	potential

Symbol	Description
V_{FENE}	FENE potential
V_{LJ}	Lennard-Jones potential
V_{WCA}	WCA potential
w	weighting factor
x	potential strength for stiffening potential,local molar fraction
$\vec{X}$	Rouse mode
ξ	friction coefficient

Table B.1: List of the symbols used in this thesis

Bibliography

[Ale69] L. E. Alexander. *X-Ray Diffraction Methods in Polymer Science*. John Wiley & Sons, 1969.

[AST98] Stelios J. Antoniadis, Christina T. Samara, and Doros N. Theodorou. Molecular dynamics of atactic polypropylene melts. *Macromolecules*, 31(22):7944–7952, 1998.

[AT87] M. P. Allen and D. J. Tildesley. *Computer Simulation of Liquids*. Clarendon Press, Oxford, 1987.

[Bar00] Sandra Barsky. Molecular dynamics study of diffusion in bidesperse polymer melts. *J. Chem. Phys.*, 112(7):3450–3456, 2000.

[BBD$^+$00] J. Baschnagel, K. Binder, P. Doruker, A. A. Gusev, O. Hahn, K. Kremer, W. L. Mattice, F. Müller-Plathe, M. Murat, Wolfgang Paul, S. Santos, U. W. Suter, and V. Tries. Bridging the gap between atomistic and coarse-grained models of polymers: Status and perspectives. *Adv. Polymer Sci.*, 152:41–156, 2000.

[BC96] K. Binder and G. Ciccotti, editors. *Monte Carlo and Molecular Dynamics of Condensed Matter Systems*, Como Conference Proceedings, Bologna, 1996. Italian Phys. Soc., Società Italiana di Fisica.

[BCS97] R. C. Ball, P. T. Callaghan, and E. T. Samulski. A simplified approach to the interpretation of nuclear spin correlations in entangled polymeric liquids. *J. Chem. Phys.*, 106(17):7352–7361, 1997.

[Bec93] A. D. Becke. Density functional thermochemistry. 3. The role of exact exchange. *J. Chem. Phys.*, 98(7):5648–5652, 1993.

[BF68] G. C. Berry and T. G. Fox. The viscosity of polymers and their concentrated solutions. *Adv. Polymer Sci*, 5:261–357, 1968.

[BI75] J. Brandrup and E. H. Immergut, editors. *Polymer Handbook*. Wiley, New York, 1975.

[Bin95] K. Binder, editor. *Monte Carlo and Molecular Dynamics Simulation in Polymer Science*, volume 49. Oxford University Press, Oxford, 1995.

[BPvG$^+$84] H. J. C. Berendsen, J. P. M. Postma, W. F. van Gunsteren, A. DiNola, and J. R. Haak. Molecular dynamics with coupling to an external heat bath. *J. Chem. Phys.*, 81(8):3684–3690, 1984.

[BvGMP98] C. D. Berweger, W. F. van Gunsteren, and F. Müller-Plathe. Molecular dynamics simulation with an *ab initio* potential energy function and finite element interpolation: The photoisomerisation of cis-stilbene in solution. *J. Chem. Phys.*, 108(21):8773–8781, 1998.

[CA74] J. P. Cohen-Addad. Effect of the anisotropic chain motion in molten polymers: The solidlike contribution of the nonzero average dipolar coupling to NMR signals. Theoretical description. *J. Chem. Phys.*, 60(6):2440–2453, 1974.

[CK88] I. Carmesin and K. Kremer. The bond fluctuation method - A new effective algorithm for the dynamics of polymers in all spatial dimensions. *Macromolecules*, 21(9):2819–2823, 1988.

[CP85] R. Car and M. Parinello. Unified approach for molecular dynamics and density-functional theory. *Phys. Rev. Letters*, 55(22):2471–2474, 1985.

[CS98] P. T. Callaghan and E. T. Samulski. The molecular weight dependence of nuclear spin correlations in entangled polymeric liquids. *Macromolecules*, 31(11):3693–3705, 1998.

[DBT93] L. R. Dodd, T. D. Boone, and D. N. Theodorou. A concerted rotation algorithm for atomistic Monte-Carlo simulation of polymer melts and glasses. *Mol. Phys.*, 78(4):961–996, 1993.

[de 71] P.-G. de Gennes. Reptation of a polymer chain in the presence of fixed obstacles. *J. Chem. Phys.*, 55(2):572–579, 1971.

[de 79] P. G. de Gennes. *Scaling Concepts in Polymer Physics*. Cornell Univ. Press, New York, 1979.

[de 81] P. G. de Gennes. Coherent scattering by one reptating chain. *J. de Physique*, 42(5):735–740, 1981.

[DE86] M. Doi and S. F. Edwards. *The Theory of Polymer Dynamics*, volume 73 of *International Series of Monographs on Physics*. Clarendon Press, Oxford, 1986.

[DFA98] G. Dlubek, Helen M. Fretwell, and A. Alam. Positron lifetime studies of local free volume in elastomer modified thermoplastics. *Phys. Stat. Sol. A*, 167(2):R13–R14, 1998.

[DG99] Raffaele Guido Della Valle and Domenico Gazzillo. Towards an effective potential for the monomer, dimer, hexamer, solid and liquid forms of hydrogen fluoride. *Phys. Rev. B*, 59(21):13699–13706, 1999.

[DGK98] Burkhard Dünweg, Gary S. Grest, and Kurt Kremer. Molecular dynamics simulations of polymer systems. In S. G. Whittington, editor, *Numerical Methods for Polymeric Systems*, volume 102 of *IMA Volumes in Mathematics and its Applications*, pages 159–196. Springer, 1998.

[DHP71] R. Ditchfield, W. J. Hehre, and J. A. Pople. Self-consistent molecular-orbital methods. IX. An extended gaussian-type basis for molecular orbital studies on organic molecules. *J. Chem. Phys.*, 54(2):724–728, 1971.

[DLM89] R. Dejean de la Batie, F. Lauprêtre, and L. Monnerie. Carbon-13 NMR investigation of local dynamics at temperatures well above the glass-transition temperature. 3. *cis*-1,4-polybutadiene and *cis*-1,4-polyisoprene. *Macromolecules*, 22(1):122–129, 1989.

[dLS92] J. J. de Pablo, M. Laso, and U. W. Suter. Simulation of polyethylene above and below the melting-point. *J. Chem. Phys.*, 96(3):2395–2403, 1992.

[Doi85] Masao Doi. Effect of chain flexibility on the dynamics of rodlike polymers in the entangled state. *J. of Polymer Science: Polymer Symposium*, 73:93–103, 1985.

[Dox] Manolis Doxastakis. personal communication.

[DP89] J. Denault and J. Prud'homme. Carbon-13 nuclear overhauser effect and molecular motion in bulk elastomers. *Macromolecules*, 22(3):1307–1316, 1989.

[DT77] Michael J. S. Dewar and Walter Thiel. Ground states of molecules. 38. The MNDO method. approximations and parameters. *J. Am. Chem. Soc.*, 99(15):4899–4907, 1977.

[ER97] B. Ewen and D. Richter. Neutron spin echo investigations on the segmental dynamics of polymers in melts, networks and solutions. *Adv. Polymer Sci.*, 134:1–129, 1997.

[Fer80] John D. Ferry. *Viscoelastic Properties of Polymers*. John Wiley & Sons, New York, 3 edition, 1980.

[FKMP99] Roland Faller, Alexander Kolb, and Florian Müller-Plathe. Local chain ordering in amorphous polymer melts: Influence of chain stiffness. *Phys. Chem. Chem. Phys.*, 1(9):2071–2076, 1999.

[FLG99] Lewis J. Fetters, David J. Lohse, and William W. Graessley. Chain dimensions and entanglement spacings in dense macromolecular systems. *J. of Polymer Science Part B: Polymer Physics*, 37(10):1023–1033, 1999.

[FLMG99] Lewis J. Fetters, David J. Lohse, Scott T. Milner, and William W. Graessley. Packing length influence in linear polymer melts on the entanglement, critical and reptation molecular weights. *Macromolecules*, 32(20):6847–6851, 1999.

[FLR$^+$94] L. J. Fetters, D. J. Lohse, D. Richter, T. A. Witten, and A. Zirkel. Connection between polymer molecular weight, density, chain dimensions and melt viscoelastic properties. *Macromolecules*, 27(17):4639–4646, 1994.

[FMPH00] Roland Faller, Florian Müller-Plathe, and Andreas Heuer. Local reorientation dynamics of semiflexible polymers in the melt. *Macromolecules* in press, 2000.

[FPMP99] Roland Faller, Mathias Pütz, and Florian Müller-Plathe. Orientation correlations in simplified models of polymer melts. *Int J. Mod. Phys. C*, 10(2 & 3):355–360, 1999.

[FS96] D. Frenkel and B. Smit. *Understanding Molecular Simulation: From Basic Algorithms to Applications*. Academic Press, San Diego, CA, 1996.

[FSBMP99] Roland Faller, Heiko Schmitz, Oliver Biermann, and Florian Müller-Plathe. Automatic parameterization of forcefields for liquids by simplex optimization. *J. Comput. Chem.*, 20(10):1009–1017, 1999.

[FTS+95] M. J. Frisch, G. W. Trucks, H. B. Schlegel, P. M. W. Gill, B. G. Johnson, M. A. Robb, J. R. Cheeseman, T. A. Keith, G. A. Petersson, J. A. Montgomery, K. Raghavachari, M. A. Al-Laham, V. G. Zakrzewski, J. V. Ortiz, J. B. Foresman, J. Cioslowski, B. B. Stefanov, A. Nanayakkara, M. Challacombe, C. Y. Peng, P. Y. Ayala, W. Chen, M. W. Wong, J. L. Andres, E. S. Replogle, R. Gomperts, R. L. Martin, D. J. Fox, J. S. Binkley, D. J. Defrees, J. Baker, J. P. Stewart, M. Head-Gordon, C. Gonzalez, and J. A. Pople. *Gaussian 94 Revision C.3*. Gaussian, Inc., Pittsburg PA, 1995.

[FTS+98] M. J. Frisch, G. W. Trucks, H. B. Schlegel, G. E. Scuseria, M. A. Robb, J. R. Cheeseman, V. G. Zakrzewski, J. A. Montgomery, R. E. Stratmann, J. C. Burant, S. Dapprich, J. M. Millam, A. D. Daniels, K. N. Nudin, M. C. Strain, O. Farkas, J. Tomasi, V. Barone, M. Cossi, R. Cammi, B. Menucci, C. Pomelli, C. Adamo, S. Clifford, J. Ochterski, G. A. Petersson, P. Y. Ayala, Q. Cui, K. Morokuma, D. K. Malick, A. D. Rabuck, K. Raghavachari, J. B. Foresman, J. Cioslowski, J. V. Ortiz, B. B. Stefanov, G. Liu, A. Liashenko, P. Piskorz, I. Komaromi, R. Gomperts, R. L. Martin, D. J. Fox, T. Keith, M. A. Al-Laham, C. Y. Peng, A. Nanayakkara, C. Gonzalez, M. Challacombe, P. M. W. Gill, B. G. Johnson, W. Chen, M. W. Wong, J. L. Andres, M. Head-Gordon, E. S. Replogle, and J. A. Pople. *Gaussian 98 Revision A.5*. Gaussian, Inc., Pittsburg PA, 1998.

[GHS98] R. Graf, A. Heuer, and H.W. Spiess. Chain-order effects in polymer melts probed by ^{1}H double-quantum NMR spectroscopy. *Phys. Rev. Letters*, 80(26):5738–5741, 1998.

[GK86] Gary S. Grest and Kurt Kremer. Molecular dynamics simulation for polymers in the presence of a heat bath. *Phys. Rev. A*, 33(5):R3628–R3631, 1986.

[Gra98] Robert Graf. *Hochauflösende Doppelquanten-NMR-Spektroskopie an amorphen Polymeren*. PhD thesis, MPI für Polymerforschung and Universität Mainz, Shaker Verlag, Aachen, 1998.

[GW97] Robert D. Groot and Patrick B. Warren. Dissipative particle dynamics: Bridging the gap between atomistic and mesoscopic simulation. *J. Chem. Phys.*, 107(11):4423–4435, 1997.

[Hai92] J. M. Haile. *Molecular Dynamics Simulation: Elementary methods*. John Wiley & Sons, New York, 1992.

[HDS96] W. Humphrey, A. Dalke, and K. Schulten. VMD - Visual Molecular Dynamics. *J. Molec. Graphics*, 14(1):33–38, 1996.

[HH99] J. Hunger and G. Huttner. Optimization and analysis of force field parameters by combination of genetic algorithms and neural networks. *J. Comput. Chem.*, 20(4):455–471, 1999.

[HMT98] Vagelis A. Harmandaris, Vlasis G. Mavrantzas, and Doros N. Theodorou. Atomistic molecular dynamics simulation of polydisperse polyethylene melts. *Macromolecules*, 31(22):7934–7943, 1998.

[Hoc70] R. W. Hockney. The potential calculation and some applications. In B. Alder, S. Fernbach, and M. Rotenberg, editors, *Methods in computational physics. IX. Plasma physics.*, pages 135–211, London, 1970. NASA, Academic Press.

[HvdE99] H. E. A. Huitema and J. P. van der Eerden. Can Monte Carlo simulation describe dynamics? A test on Lennard-Jones systems. *J. Chem. Phys.*, 110(7):3267–3274, 1999.

[HWR97] Ludger Harnau, Roland G. Winkler, and Peter Reineker. Influence of stiffness on the dynamics of macromolecules in the melt. *J. Chem. Phys.*, 106(6):2469–2476, 1997.

[HZF82] Nikos Hadjichristidis, Xu Zhongde, and L. J. Fetters. The characteristic ratios of stereoirregular polybutadiene and polyisoprene. *J. of Polymer Science: Polymer Physics Ed.*, 20(4):743–750, 1982.

[Jon24] J. E. Jones. On the determination of molecular fields. II. From the equations of state of a gas. *Proc. R. Soc. London A*, 106:463–477, 1924.

[KB84] K. Kremer and K. Binder. Dynamics of polymer chains confined into tubes: Scaling theory and Monte Carlo simulations. *J. Chem. Phys.*, 81(12):6381–6394, 1984.

[KBB84] Hans-Otto Kalinowski, Stefan Berger, and Siegmar Braun. *^{13}C-NMR-Spektrokospie*. Thieme, Stuttgart, 1984.

[KG90] Kurt Kremer and Gary S. Grest. Dynamics of entangled linear polymer melts: A molecular-dynamics simulation. *J. Chem. Phys.*, 92(8):5057–5086, 1990.

[KGC88] Kurt Kremer, Gary S. Grest, and I. Carmesin. Crossover from Rouse to reptation dynamics: A molecular-dynamics simulation. *Phys. Rev. Letters*, 61(5):566–569, 1988.

[Kol99] Alexander Kolb. *Molekular-Dynamik-Untersuchungen zum Wechselspiel zwischen flüssigkristalliner Ordnung und den Konformationen von Polymerketten*. PhD thesis, MPI für Polymerforschung and Universität Mainz, 1999.

[KP49] O. Kratky and G. Porod. Röntgenuntersuchung gelöster Fadenmoleküle. *Recl. Trav. Chim. Pays-Bas*, 68:1106–1122, 1949.

[KSY86] A. Kolinski, J. Skolnick, and R. Yaris. Monte Carlo study of local orientational order in a semiflexible polymer melt model. *Macromolecules*, 19(10):2550–2560, 1986.

[KT95] P. V. Krishna Pant and Doros N. Theodorou. Variable connectivity method for the atomistic Monte Carlo simulation of polydisperse polymer melts. *Macromolecules*, 28(21):7224–7234, 1995.

[Kuh34] Werner Kuhn. Über die Gestalt fadenförmiger Moleküle in Lösungen. *Kolloid Z.*, 68(1):2–15, 1934.

[LBM93] Françoise Lauprêtre, Liliane Bokobza, and Lucien Monnerie. Comparison of the local chain dynamics in a series of bulk polymers well above glass transition temperature. *Polymer*, 34(3):468–475, 1993.

[Lid95] David R. Lide, editor. *CRC handbook of chemistry and physics*. CRC Press, Boca Raton, 76 edition, 1995.

[LS82a] Giovanni Lipari and Attila Szabo. Model-free approach to the interpretation of nuclear magnetic resonance relaxation in macromolecules. 1. Theory and range of validity. *J. Am. Chem. Soc.*, 104(17):4546–4559, 1982.

[LS82b] Giovanni Lipari and Attila Szabo. Model-free approach to the interpretation of nuclear magnetic resonance relaxation in macromolecules. 2. Analysis of experimental results. *J. Am. Chem. Soc.*, 104(17):4559–4570, 1982.

[MBF$^+$00] Hendrik Meyer, Oliver Biermann, Roland Faller, Dirk Reith, and Florian Müller-Plathe. Coarse graining of nonbonded interparticle potentials using automatic simplex optimization to fit structural properties. *J. Chem Phys.* in press, 2000.

[MBZT99] Vlasis G. Mavrantzas, Travis D. Boone, Evangelia Zervopoulou, and Doros N. Theodorou. End-bridging Monte Carlo: A fast algorithm for atomistic simulation of condensed phases of long polymer chains. *Macromolecules*, 32(15):5072–5096, 1999.

[MC80] A. D. McLean and G. S. Chandler. Contracted gaussian basis set for molecular calculations. I. Second row atoms Z=11-18. *J. Chem. Phys.*, 72(10):5639–5648, 1980.

[ME96] Neil E. Moe and M. D. Ediger. Molecular dynamics computer simulation of local dynamics in polyisoprene melts. *Polymer*, 37(10):1787–1795, 1996.

[ME99] Neil E. Moe and M. D. Ediger. Calculation of the coherent dynamic structure factor of polyisoprene from molecular dynamics simulations. *Phys. Rev. E*, 59(1):623–630, 1999.

[MK98] Michael Murat and Kurt Kremer. From many monomers to many polymers: Soft ellipsoid model for polymer melts and mixtures. *J. Chem. Phys.*, 108(10):4340–4348, 1998.

[MM98] S. T. Milner and T. C. B. McLeish. Reptation and contour-length fluctuations in melts of linear polymers. *Phys. Rev. Letters*, 81(3):725–728, 1998.

[Mor98a] David C. Morse. Viscoelasticity of tightly entangled solutions of semiflexible polymers. *Phys. Rev. E*, 58(2):R1237–R1240, 1998.

[Mor98b] David C. Morse. Viscoelaticity of concentrated isotropic solutions of semiflexible polymers. 1. Model and stress tensor. *Macromolecules*, 31(20):7030–7043, 1998.

[Mor98c] David C. Morse. Viscoelaticity of concentrated isotropic solutions of semiflexible polymers. 2. Linear response. *Macromolecules*, 31(20):7044–7067, 1998.

[MP] Florian Müller-Plathe. personal communication.

[MP93] Florian Müller-Plathe. YASP: A molecular simulation package. *Comput. Phys. Commun.*, 78(1-2):77–94, 1993.

[MP97] Florian Müller-Plathe. Molecular simulation - A primer. In S. Wilson and G. H. F. Diercksen, editors, *Problem Solving in Computational Molecular Science: Molecules in Different Environments*, volume 500 of *NATO ASI Series C*, pages 389–412, Dordrecht, 1997. NATO, Kluwer Academic Publishers.

[MPB91] F. Müller-Plathe and D. Brown. Multi-colour algorithms in molecular simulation: Vectorisation and parallelisation of internal forces and constraints. *Comput. Phys. Commun.*, 64(1):7–14, 1991.

[MPSF00] Florian Müller-Plathe, Heiko Schmitz, and Roland Faller. Molecular simulation in polymer science: Understanding experiments better. *Prog. Theor. Phys. (Kyoto) Supplements*, 138:311–319, 2000.

[MRR$^+$53] Nicholas Metropolis, Arianna W. Rosenbluth, Marshall N. Rosenbluth, Augusta H. Teller, and Edward Teller. Equation of state calculations by fast computing machines. *J. Chem. Phys.*, 21(6):1087–1092, 1953.

[MWC00] M. Müller, J. P. Wittmer, and M. E. Cates. Topological effects in ring polymers (II): Influence of persistence length. *Phys. Rev. E*, 61(4):4078–4089, 2000.

[NvGMP95] S. L. Njo, W. F. van Gunsteren, and F. Müller-Plathe. Determination of force field parameters for molecular simulation by molecular simulation: An application of the weak-coupling method. *J. Chem. Phys.*, 102(15):6199–6207, 1995.

[Odi83] Theo Odijk. On the statics and dynamics of confined or entangled stiff polymers. *Macromolecules*, 16(8):1340–1344, 1983.

[OKST95] Atsuyuki Oshima, Hiroyuki Kudo, Takahiro Sato, and Akio Teramoto. Entanglement effects in semiflexible polymer solutions. 1. Zero-shear viscosity of poly(*n*-hexyl isocyanate) solutions. *Macromolecules*, 28(18):6095–6099, 1995.

[OMK70] Shigeharu Onogi, Toshiro Masuda, and Keishi Kitagawa. Rheological properties of anionic polystyrenes. I. Dynamic viscoelasticity of narrow-distribution polystyrenes. *Macromolecules*, 3(2):109–125, 1970.

[PK98] M. Pütz and A. Kolb. Optimization techniques for parallel molecular dynamics using domain decomposition. *Comput. Phys. Commun.*, 113(2-3):145–167, 1998.

[PKG00] M. Pütz, K. Kremer, and G. S. Grest. What is the entanglement length in a polymer melt ? *Europhysics letters*, 49(6):735–741, 2000.

[PM96] Emanuele Paci and Massimo Marchi. Constant-pressure molecular dynamics techniques applied to complex molecular systems and solvated proteins. *J. Phys. Chem.*, 100(10):4314–4322, 1996.

[PSC94] T. Perkins, D. E. Smith, and S. Chu. Direct observation of tube-like motion of a single polymer-chain. *Science*, 264(5160):819–822, 1994.

[PSD95] D. Parrat, F. Sommer J. M. Solleti, and T. M. Due. Imaging modes in atomic-force microscopy. *Journal of Trace and Microprobe Techniques*, 13(3):343–352, 1995.

[PSY97] W. Paul, Grant D. Smith, and Do Y. Yoon. Static and dynamic properties of a n-$C_{100}H_{202}$ melt from molecular dynamics simulations. *Macromolecules*, 30(25):7772–7780, 1997.

[PTVF92] William H. Press, Saul A. Teukolsky, William T. Vetterling, and Brian P. Flannery. *Numerical Recipes in C: The Art of Scientific Computing*. Cambridge University Press, New York, 2 edition, 1992.

[Püt99] Mathias Pütz. *Dynamik von Polymerschmelzen und Quellverhalten ungeordneter Netzwerke*. PhD thesis, Universität Mainz, 1999.

[RCB77] J.-P. Ryckaert, G. Cicotti, and H. J. C. Berendsen. Numerical integration of the cartesian equations of motion of a system with constraints: Molecular dynamics of n-alkanes. *J. Comput. Phys.*, 23(3):327–341, 1977.

[Rei65] Frederick Reif. *Fundamentals of Statistical and Thermal Physics*. Mc Graw Hill, New York, 1965.

[Rou53] P. E. Rouse. A theory of linear viscoelastic properties of dilute solutions of coiling polymers. *J. Chem. Phys.*, 21(7):1272–1280, 1953.

[RP99] Richard L. Rowley and Tapani Pakkanen. Determination of a methane intermolecular potential for use in molecular simulations from *ab initio* calculations. *J. Chem. Phys.*, 110(7):3368–3377, 1999.

[RR88] David Rigby and Ryong-Joon Roe. Molecular dynamics simulation of polymer liquid and glass. II. Short range order and orientation correlation. *J. Chem. Phys.*, 89(8):5280–5290, 1988.

[SBE$^+$99] T. Z. Sen, I. Bahar, B. Erman, F. Laupretre, and L. Monnerie. Local dynamics of *cis*-1,4,-polybutadiene and *cis*-1,4,-polyisoprene. A comparative study based on cooperative kinematics theory and NMR experiments. *Macromolecules*, 32(9):3017–3024, 1999.

[Sch73] Jacob Schaefer. Distributions of correlation times and the carbon-13 nuclear magnetic resonance spectra of polymers. *Macromolecules*, 6(6):882–888, 1973.

[SFL$^+$98] P. Schleger, B. Farago, C. Lartigue, A. Kollmar, and D. Richter. Clear evidence of reptation in polyethylene from neutron spin-echo spectroscopy. *Phys. Rev. Letters*, 81(1):124–127, 1998.

[SFMP99] Heiko Schmitz, Roland Faller, and Florian Müller-Plathe. Molecular mobility in cyclic hydrocarbons: A simulation study. *J. Phys. Chem. B*, 103(44):9731–9737, 1999.

[Sli90] C. P. Slichter. *Principles of Magnetic Resonance*. Number 1 in Springer Series in Solid-State Sciences. Springer, Berlin, 2 edition, 1990.

[SMPF00] Heiko Schmitz, Florian Müller-Plathe, and Roland Faller. Hole size distributions and positronium lifetimes in different polymers examined by computer simulation for different polymers. in preparation, 2000.

[SRS94] Klaus Schmidt-Rohr and Hans Wolfgang Spiess. *Multidimensional solid state NMR and polymers*. Academic Press, New York, 1994.

[ST91] Takahiro Sato and Akio Teramoto. Dynamics of stiff-chain polymers in isotropic solution: Zero-shear viscosity of rodlike polymers. *Macromolecules*, 24(1):193–196, 1991.

[Str97] Gert Strobl. *The Physics of Polymers*. Springer Verlag, Berlin, 2 edition, 1997.

[TR91] Hisao Takeuchi and Ryong-Joon Roe. Molecular dynamics simulation of local chain motion in bulk amorphous polymers. I. Dynamics above the glass transition. *J. Chem. Phys.*, 94(11):7446–7457, 1991.

[TST91] Yasushi Takada, Takahiro Sato, and Akio Teramoto. Dynamics of stiff-chain polymers in isotropic solution. 2. Viscosity of aqueous solutions of xanthan, a rigid double-helical polysaccharide. *Macromolecules*, 24(23):6215–6219, 1991.

[Tur97] Paul Turner. Xmgr 4.1.2. Technical report, Weizmann Institute, Rehovot, Israel, 1997.

[Ver67] L. Verlet. Computer ‘experiments’ on classical fluids. I. Thermodynamical properties of Lennard-Jones molecules. *Phys. Rev.*, 159:98–103, 1967.

[vGB90] Wilfred F. van Gunsteren and Herman J. C. Berendsen. Computer simulation of molecular dynamics: Methodology, applications, and perspectives in chemistry. *Angew. Chem. Int. Ed. Engl.*, 29(9):992–1023, 1990.

[WCA71] J. D. Weeks, D. Chandler, and H.C. Andersen. Role of repulsive forces in determining the equilibrium structure of simple liquids. *J. Chem. Phys.*, 54(12):5237–5247, 1971.

[WH79] Thomas A. Weber and Eugene Helfand. Molecular dynamics simulation of polymers. I. Structure. *J. Chem. Phys.*, 71(11):4760–4762, 1979.

[WPB92] J. Wittmer, W. Paul, and K. Binder. Rouse and reptation dynamics at finite temperatures: A Monte Carlo simulation. *Macromolecules*, 25(26):7211–7219, 1992.

[WSDMP00] Richard Witt, Laszlo Sturz, Andreas Dölle, and Florian Müller-Plathe. Molecular dynamics of benzene in neat liquid and a solution containing polystyrene. ^{13}C nuclear magnetic relaxation and molecular dynamics simulation results. *J. Phys. Chem. A* in press, 2000.

[Wu89] Souheng Wu. Chain structure and entanglement. *J. of Polymer Sci.: Part B Polymer Physics*, 27(4):723–741, 1989.

[ZAC+95] R. Zorn, A. Arbe, J. Colmenero, B. Frick, D. Richter, and U. Buchenau. Neutron scattering study of the picosecond dynamics of polybutadiene and polyisoprene. *Phys. Rev. E*, 52(1):781–795, 1995.

[Zim56] Bruno H. Zimm. Dynamics of polymer molecules in dilute solution: Viscoelasticity, flow birefringence and dielectric loss. *J. Chem. Phys.*, 24(2):269–278, 1956.

[ZRF+92] R. Zorn, D. Richter, B. Farago, B. Frick, F. Kremer, U. Kirst, and L. J. Fetters. Comparative-study of the segmental relaxation in polyisoprene by quasi-elastic neutron-scattering and dielectric-spectroscopy. *Physica B*, 180 & 181(Part A):534–536, 1992.

List of Figures

1.1 Different topologies of polymers 14

2.1 Explanation of the structure factor 19
2.2 Illustration of the Rouse model 21
2.3 Scaling of MSD for Rouse and reptation 23
2.4 Plateau in storage modulus 24
2.5 Transformation of the curvilinear motion to Cartesian space 25
2.6 Destruction and rebuilding of the tube 25
2.7 Hooked polymer chains 26
2.8 Fuzzy cylinder model 27
2.9 Deflection Length of Odijk 28
2.10 Loosely and highly entangled polymers 29
2.11 The chain in the tube and its primitive path. 31
2.12 Different diffusion scenarios for flexible and stiff chains 32
2.13 Illustration of double quantum filtering 34
2.14 Course of time of double quantum NMR experiments 35
2.15 Extreme narrowing limit 36
2.16 Illustration of entanglements for NMR and reptation 37
2.17 Scaling for reorientation correlation function 38

3.1 Scheme of the different methods 40
3.2 Scheme of end-bridging move 44
3.3 The hypothetical chain for end-bridging 45
3.4 Comparison of potential strengths 46
3.5 Illustration of applying the stiffening potential to every or only every second angle. 46
3.6 Exclusion radius for setup 47
3.7 Relaxation of end-to-end distance 48

4.1 Bond correlation functions 51
4.2 Definition of angle and distance for static correlations 52
4.3 Illustration of the meaning of positive and negative values of the orientation correlation function (second Legendre polynomial). The values correspond to the dimers indicated by blue arrows. 53
4.4 Inter-chain orientation correlation functions 53
4.5 Definition of fcc lattice 54
4.6 *OCF* of flexible chains versus lattice 55
4.7 Definition of segment unit vectors 55
4.8 *OCF* of medium size segments 55

4.9 Inter-chain RDF 56
4.10 Single chain structure factor in the generic model 57

5.1 Short time reorientation in bead-spring system 62
5.2 Long time reorientation in bead-spring systems 63
5.3 Reorientation time versus stiffness 64
5.4 Reorientation depending on segment length 65
5.5 Double-quantum correlation functions 66
5.6 Reorientation versus translation 68
5.7 Sketch of reptation in a moving tube 69
5.8 Collapse of Rouse modes 71
5.9 Rouse modes for stiff chains 73
5.10 Rouse modes for entangled chains 74
5.11 Rouse scaling for different chain lengths 74
5.12 Chain diffusion constant versus chain length 76
5.13 MSD of inner monomers and center of mass 78
5.14 Visualization of the reptation tube 80
5.15 Anisotropic displacement 81
5.16 Dynamical structure functions 83
5.17 Fits of dynamic structure functions 84
5.18 Master-plot of dynamic structure factor 85

6.1 Sketch of *trans*-1,4-polyisoprene 90
6.2 Energy barrier for torsion 1. 94
6.3 Comparison of calculated and fitted torsion potential 96
6.4 The simplex moves 98
6.5 Molecular weight distributions 101
6.6 Example conformations of atomistic chains 102
6.7 Bond correlation functions for atomistic polyisoprene 103
6.8 Atomistic Torsion distributions 104
6.9 Atomistic radial distribution functions 105
6.10 Atomistic center of mass RDF 105
6.11 Partial RDFs in the atomistic simulations 106
6.12 Atomistic orientation correlations 108
6.13 Atomistic melt structure factor 110
6.14 Reorientation of atomistic end-to-end vector 111
6.15 Atomistic Reorientation of double bonds 112
6.16 Reorientation of C−H vectors 114
6.17 Two stage process in methyl group reorientation 116
6.18 Comparison segmental reorientation to C=C reorientation 118

7.1 Comparison MSD atomistic and bead-spring 122
7.2 Comparative Rouse mode analysis of atomistic/bead-spring simulations 123
7.3 Segmental reorientation in polyisoprene 124
7.4 Comparative reorientation of bead-spring and atomistic 124

List of Tables

2.1 Theoretical predictions of entanglement lengths 30

4.1 Radius of gyration, persistence length, end-to-end distance 50

5.1 Overview over bead-spring systems 60
5.2 Exponential fits against segment length for reorientation 65
5.3 Algebraic fits of double quantum functions 67
5.4 Rouse times for different systems 72
5.5 Rouse friction coefficients 75
5.6 Entanglement length versus persistence length 77
5.7 Entanglement lengths according to the packing concept 81
5.8 Overview of the dynamics of the bead-spring models 86
5.9 The different dynamic classes 87

6.1 Characteristics of atomistic simulations 90
6.2 Relevant conformations of single bonds in di-isoprene 92
6.3 Torsion conformations after to DFT calculation 92
6.4 QC calculated energy barriers for torsion 1 93
6.5 Relative Torsion energies for torsions 2 and 3 95
6.6 Fitted force-field parameter for Torsions 95
6.7 Geometry parameters for atomistic simulations 97
6.8 Non-bonded interaction parameters 99
6.9 Non-bonded parameters for end-bridging MC equilibration 100
6.10 Acceptance rates in EBMC 100
6.11 Local molar fractions in the neighborhood of atomistic carbons 107
6.12 Experiment and simulation, the two-stage process 115
6.13 Different reorientation times 117
6.14 Torsion classes 118
6.15 Torsion transitions 119

B.1 List of Symbols 133

Acknowledgments

Of course, not one single person contributes to a thesis like the present one. A lot of discussions, comments and helpful idea contribute from various sides.

I would like to thank Prof. Kurt Kremer for the opportunity to work in his group at the MPIP and for the continuing interest at all stages of the work.

Dr. Florian Müller-Plathe, as my direct project leader and supervisor, was all the time involved in all stages of the work. Without the numerous ideas, concepts and hints from his side this thesis definitely would not have been written in this time. He always had time for discussions in and outside of science.

The whole YASP-group Oliver Biermann, Dr. Hendrik Meyer, Dirk Reith, and my room-mate Dr. Heiko Schmitz were involved in many discussions and comments. It was really working in a team.

Dr. Markus Deserno and Dr. Ralf Everaers gave very useful comments and offered fruitful discussions.

Dr. Robert Graf and Prof. Andreas Heuer explained to me lots of the details and interesting phenomena of the NMR experiments.

The data for the long flexible simulations I got from Dr. Mathias Pütz as well as some helpful analysis tools for the calculation of e.g. structure factors.

The whole AK Kremer group in the institute offered an inspiring atmosphere. Our secretary Doris Kirsch gave always a friendly word and a helpful hand.

The language competence of Dr. Alex Bunker, and Sabine Sauer was very helpful in the final stages of writing the thesis.

Out of work, the cooking sessions with Markus and Oliver were an opportunity to switch off the brain and relax. Patrick Ahlrichs and Dirk shared my interest in shouting at German soccer teams on TV. Also the board game sessions including Heiko, who had to stand me two years in one office, and Thomas Soddemann contributed to the nice time here in Mainz.

A warm thanks goes to the university of Patras, Greece, to Prof. Doros Theodorou, Manolis Doxastakis, Vagelis Harmandaris, and the rest of the group in the department of chemical engineering for the friendly integration into their group during my stay in Patras.

Last, but not at all least, it was very important that I could rely on my family all the time.

Curriculum Vitae

Roland Faller
Am sonnigen Hang 2
55127 Mainz

Date and place of birth	20 April 1972, Freiburg/Brsg
Nationality	German
1978-1982	primary school, Elzach
1982-1991	Geschwister-Scholl Gymnasium (grammar school), Waldkirch
1991	Abitur (General entrance qualification)
1991/1992	Civil service in lieu of military service
1992-1997	study of physics, university of Bayreuth
1994	Pre-diploma
1997	Diploma, Thesis: *Untersuchungen an der komplexen Ginzburg-Landau Gleichung für anisotrope Systeme*
1997-2000	PhD student at Max-Planck institute for polymer research and university of Mainz, Thesis: *Influence of Chain Stiffness on Structure and Dynamics of Polymers in the Melt*